TECHNISCHE UNIVERSITÄT WIEN
Vienna | Austria

DIPLOMARBEIT

Perovskite-based mixed conducting thin film anodes for proton conducting solid oxide fuel cells

Ausgeführt am Institut für

Chemische Technologien und Analytik der Technischen Universität Wien

unter der Anleitung von

Univ.Ass. Dipl-Ing. Dr.techn. Alexander Karl Opitz
Senior Scientist Dipl.-Ing. Dr.techn. Stefanie Taibl
Univ.-Prof. Dipl.-Phys. Dr. Jürgen Fleig

durch

Harald Summerer
Alfred-Adler-Straße 11/5/15
1100 Wien

Wien, im April 2019

Harald Summerer

Abstract

Fuel cells based on ceramic proton conducting electrolytes (so called protonic ceramic fuel cells, PCFC) have received growing interest in recent years as an alternative to conventional oxide ion conducting solid oxide fuel cells (SOFC) due to lower operating temperature requirements. State of the art composite anodes for PCFC suffer from several drawbacks such as microstructural or chemical stability. Mixed ionic-electronic conductors (MIEC) are considered as alternatives due to their electrochemically highly active surfaces.

In this study, the electrochemical polarisation resistance of various perovskite-type mixed conducting thin film electrodes such as $(La_{0.6}Sr_{0.4})FeO_{3-\delta}$ (LSF), grown by pulsed laser deposition (PLD) on $BaZr_{0.8}Ce_{0.1}Y_{0.1}O_3$ (BZCY), was studied by electrochemical impedance spectroscopy (EIS). These measurements were carried out on symmetrical cells in humid reducing atmosphere (2.5 % H_2/2.5 % H_2O in Ar) at temperatures between 300 to 700 °C. For comparison with the oxide ion conducting system the same electrode materials were also studied on yttria stabilised zirconia (YSZ) electrolyte. Moreover, the effect of oxide ion basicity on the electrode performance was investigated by either substituting Sr^{2+} with Ba^{2+} (LSBF) or creating a material with substantially higher oxide ion basicity like $(Ba_{0.9}La_{0.1})FeO_{3-\delta}$ (BLF). Interestingly, only minor dependencies of the surface exchange rates on the electrolyte and the electrode composition could be determined. In addition to impedance measurements, electrochemical DC experiments were performed. Current-voltage curves (recorded at 600 °C) further confirmed the polarisation resistance from the impedance measurements to be related to the electrode surface.

Moreover, ionic transference numbers of BZCY and YSZ were measured by electrochemical pumping experiments. Therefore, a novel measuring setup was built containing two separate gas compartments. Symmetrical cells were exposed to one oxidising (1 % O_2/2.5 % H_2O in N_2) and one reducing (2.5 % H_2/2.5 % H_2O in Ar) atmosphere. Drawing an electrochemical current together with mass spectrometric (MS) analysis of the gas composition in both compartments

allowed determination of the reaction products H_2, H_2O and O_2. Resulting transference numbers for each ionic charge carrier prove predominant proton conduction for systems with a BZCY electrolyte.

Combining the results of AC, DC and MS experiments, the same elementary process is suggested to be rate limiting in case of a proton as well as an oxide ion based reaction mechanism. Considering also previous work on the studied MIEC electrodes, H_2 dissociation or oxidative dissociation of H_2 are identified as the most likely candidates for the rate determining step of hydrogen oxidation.

Kurzfassung

In den letzten Jahren erhielten Brennstoffzellen basierend auf protonenleitenden, keramischen Elektrolyten (engl. *protonic ceramic fuel cells*, PCFC) aufgrund niedriger Arbeitstemperaturen vemehrt Aufmerksamkeit als Alternative zu konventionellen oxidionenleitenden Festoxidbrennstoffzellen (engl. *solid oxide fuel cells*). Derzeitige PCFC-Anoden besitzen mehrere Nachteile wie etwa mikrostrukturelle oder chemische Instabilitäten. So genannte elektronisch-ionische Mischleiter (engl. *mixed ionic-electronic conductors*, MIEC) gelten als vielversprechende Alternative aufgrund ihrer elektrochemisch hoch aktiven Oberflächen.

In dieser Studie wurde der elektrochemische Polarisationswiderstand von unterschiedlichen mischleitenden Dünnfilmelektroden vom Perowskit-Typ untersucht. Via Laserdeposition (engl. *pulsed laser deposition*, PLD) konnten Filme aus beispielsweise $(La_{0.6}Sr_{0.4})FeO_{3-\delta}$ (LSF) auf dem Elektrolytmaterial $BaZr_{0.8}Ce_{0.1}Y_{0.1}O_3$ (BZCY) mit elektrochemischer Impedanzspektroskopie (EIS) untersucht werden. Diese Messungen symmetrischer Zellen wurden in befeuchteter, reduzierender Atmosphäre (2.5 % H_2/2.5 % H_2O in Ar) bei Temperaturen zwischen 300 und 700 °C durchgeführt. Zum Vergleich mit dem bekannteren Oxidionen leitenden System wurden diese Elektrodenmaterialien auch auf yttrium-stabilisiertem Zirkoniumdioxid (YSZ) durchgeführt. Ferner sollte noch der Effekt der Oxidionenbasizität auf die Elektrodenperformance, entweder durch Ersetzen von Sr^{2+} mit Ba^{2+} (LSBF) oder durch Synthese eines Materials mit signifikant höherer Oxidionenbasizität $(Ba_{0.9}La_{0.1})FeO_{3-\delta}$ (BLF), untersucht werden. Hier zeigte sich jedoch nur ein kleiner Einfluss auf die Oberflächenaustauschrate unabhängig vom Elektrolyt und von der Elektrodenzusammensetzung. Zusätzlich wurden im Zuge von Gleichstromexperimenten noch Strom-Spannungs-Kurven (bei 600 °C) aufgenommen, die ebenfalls auf einen oberflächenbezogenen Polarisationswiderstand hinwiesen.

Weiters konnten in einem elektrochemischen Pumpexperiment die ionischen Überführungszahlen von BZCY und YSZ mithilfe eines neuen Messapparats, der zwei getrennte Gaskompartimente aufwies, bestimmt werden. Symmetrische Zellen konnten somit gleichzeitig einer oxidierenden (1 % O_2/2.5 % H_2O in N_2) und einer reduzierenden (2.5 % H_2/2.5 % H_2O in Ar) Atmosphäre ausgesetzt werden. Massenspektrometrische Analyse (MS) der Gaszusammensetzung

unter elektrochemischen Stromfluss ermöglichte so die Bestimmung der Reaktionsprodukte H_2, H_2O und O_2. Die erhaltenen Überführungszahlen der ionischen Ladungsträger zeigte eine überwiegende Protonenleitfähigkeit für das System mit einem BZCY-Elektrolyten.

Die Ergebnisse der oben genannten Experimente weisen darauf hin, dass derselbe Elementarprozess sowohl für Protonen- als auch Oxidionen-basierte Reaktionsmechanismus ratenlimitierend ist. Bei Berücksichtigung früherer Arbeiten an diesen MIEC-Elektroden kann der ratenlimitierende Schritt entweder auf die Dissoziation von H_2 oder die oxidative Dissoziation von H_2 eingeschränkt werden.

Acknowledgements

Lange hat es gedauert. Nun ist es aber doch soweit. Während ich diese letzten Worte meiner Diplomarbeit verfasse, schweifen meine Gedanken natürlich auch zu den Leuten, die mich auf dem Weg hierher unterstützt haben. Daher seien die folgenden Worte ausschließlich ihnen gewidmet.

Zuerst möchte ich hiermit bei Prof. Jürgen Fleig bedanken, der mir eine Diplomarbeit in seiner Arbeitsgruppe ermöglicht hat. Außerdem seien hier meine Betreuer Alexander Opitz und Stefanie Taibl genannt, die meine mitunter nervigen Fragen stets ausführlich beantwortet haben.

Ferner möchte ich mich noch bei den Mitgliedern der Arbeitsgruppe Elektrochemie bedanken. Das ausgezeichnete Arbeitsklima sorgte insbesondere in schwierigen Zeiten dafür, dass weder der Mut noch der Spaß vollständig verloren gegangen sind. An dieser Stelle möchte ich mich noch im Speziellen bei Alexander Viernstein bedanken, der insbesondere am Anfang meine Aufnahme in die Arbeitsgruppe durch seine extrovertierte Art erleichtert hat. Ferner möchte ich mich bei Max Morgenbesser und Stefan Smetaczek bedanken, die beide nicht nur meine Raunzereien meisterhaft über sich ergehen haben lassen, sondern auch stets für spaßigen Klatsch und Tratsch am Freitag Nachmittag zur Verfügung gestanden sind. Hierbei sei ferner Alexander Schmid genannt, mit dem ich den perfekten Kompagnon für allerlei nerdiges Zeug gefunden habe. Seine Unterstützung bei verschiedenen Basteleien oder Fragen zu fachlichen Dingen bzw. Programmieren hat mich vor den einen oder anderen grauen Haaren bewahrt.

Abschließend möchte ich natürlich noch bei meinen Freunden und meiner Familie bedanken. Dies betrifft speziell meine Eltern, die mir dieses Studium überhaupt ermögicht haben und mich auch trotz meiner mitunter schwierigen Eigenheiten stets unterstützt haben. Andererseits sei hier mein kleiner Bruder genantn, auf dessen Rückhalt ich stets bauen kann. Es ist angenehm jemanden an seiner Seite zu haben, der für einen durchs Feuer geht!

Contents

1. Introduction 1

2. Theoretical Background 6
   - 2.1. Charge Transport in Ionic Solids . . . 6
     - 2.1.1. Point Defects . . . 7
     - 2.1.2. Mass and Charge Transport . . . 11
   - 2.2. Perovskite: Structure and Defects . . . 13
   - 2.3. PCFC vs. SOFC . . . 14
   - 2.4. Measurement Techniques . . . 19
     - 2.4.1. Electrochemical Impedance Spectroscopy (EIS) . . . 19
     - 2.4.2. Mass Spectrometry (MS) . . . 22

3. Experimental 27
   - 3.1. Target Preparation and Characterisation . . . 27
   - 3.2. Sample Preparation . . . 28
     - 3.2.1. Samples for Electrolyte Characterisation . . . 28
     - 3.2.2. Macroscopic Electrodes for Symmetric Samples . . . 29
     - 3.2.3. Microelectrode Preparation . . . 32
     - 3.2.4. Samples for Electrochemical Pumping Experiments . . . 34
   - 3.3. Electrochemical Experiments . . . 35
     - 3.3.1. Electrolyte Characterisation . . . 35
     - 3.3.2. AC Experiments . . . 36
     - 3.3.3. DC Experiments . . . 37
     - 3.3.4. Electrochemical Pumping Experiments . . . 38

4. Results and Discussion 42
   - 4.1. Target and Sample Characterisation . . . 42
     - 4.1.1. X-ray Diffraction (XRD) . . . 42
     - 4.1.2. Scanning Electron Microscopy (SEM) . . . 43

4.2. Characterisation of Electrolyte Conductivity 46
4.3. Electrochemical Characterisation of Proton Conducting MIEC Electrodes . . . 52
4.4. I-V Curves 58
4.5. Electrochemical Pumping Experiments 62
4.5.1. Expected Reactions 62
4.5.2. Proton Conductor 66
4.5.3. Oxygen Ion Conductor 70
4.5.4. Transference Numbers 73

5. Mechanistic Conclusion **80**

6. Summary and Outlook **83**

A. Electrolyte Characterisation **85**

B. 2-Gas Measurements **87**

Bibliography **96**

1. Introduction

According to the International Energy Agency (IEA) the energy policy driver of any country in the world consists of three E's: **E**nergy security, **E**conomic growth and **E**nvironmental protection. One of its main objectives remains the reduction of greenhouse-gas emissions, which contribute to climate change [1]. This is made more difficult due to the rising global demand in energy services which is closely linked to the rapidly increasing world population. The number of countries with a high level of industrialisation is rising and state-of-the-art technologies based on fossil fuel combustion won't be sufficient to ensure the energy supply of the whole world. All this shows the critical role of energy in discussions regarding sustainable development. Consequently, several solutions to the necessity of a cleaner energy technology have evolved [2, 3]:

- Increased use of renewable sources (water, sun, wind, ...)
- Energy conservation through improved energy efficiency
- Reduction of fossil fuels

Over 70 % of net additions to global power generating capacity in 2017 consisted of renewable power which makes this its largest annual increase ever [4]. Another important aspect is the push towards improved efficiencies, in other words the careful use of the available resources. The level of efficiency in current automobiles lies between 20 - 30 %. Thus, a significant portion of the expended energy is wasted.

Fuel cells are electrochemical devices that allow the direct conversion of chemical into electrical energy. The electricity and heat are generated by an electrochemical reaction of gaseous fuel (hydrogen) and an oxidant gas (oxygen from the air). The half-reactions oxidation of the fuel and reduction of the oxidant take place in two compartments separated by an ion conducting electrolyte. As a product water is formed at the exhaust. Both electrodes (anode and

cathode) are electronically connected via an external circuit. In recent years the interest in fuel cells among the various alternative energy technologies has grown significantly due to multiple advantages [5]:

- High efficiency, independent from cell size
- Flexibility of operation for a wide range of applications (stationary or portable)
- Continuous energy production
- Low pollutant emission

Due to the direct conversion of chemical energy, a fuel cell can extract more electricity from the same amount of fuel than any conventional thermo-mechanical system. Based on the type of the cell (see below) different operation modes and a wide variety of applications are possible. Unlike a battery, energy production occurs as long as fuel is supplied. Since they operate without combustion, pollutant emissions are negligible or even zero if hydrogen from renewable sources is used.

Up to now, various types of fuel cells have been developed, usually classified after the electrolyte material used. Examples include proton exchange membranes (PEMFC), phosphoric acid (PAFC), molten carbonate (MCFC) or solid oxide (SOFC) among others. An overview is presented in Fig. 1.1 which also shows fuel types, oxidising agents and mobile ions. Operational temperatures of these materials vary greatly due to their nature. Hence, numerous application possibilities exist. Of all fuel cell systems mentioned PEMFCs and SOFCs are the ones furthest in development and considered for commercialisation. Both have advantages and disadvantages in terms of operating temperature, costs, materials used and applications.

In PEMFCs, perfluorosulfonic acid polymers like Nafion are the most common electrolytes, which require liquid water to maintain proton conductivity. The necessity of keeping the polymer hydrated and its acid groups stable, limits the operating temperature to around 100 °C. Platinum and platinum alloys are typical catalyst materials in conventional PEMFCs. Their current popularity lies in short start-up time, broad range of application (especially in the mobile sector) and their design and package flexibility. Disadvantages of PEMPFCs are severe poisoning of the Pt electrode by CO present in the fuel and thus requiring expensive H_2-fuel of highest purity, poor kinetics of the oxygen reduction reaction on the cathode and large overpotential losses [6].

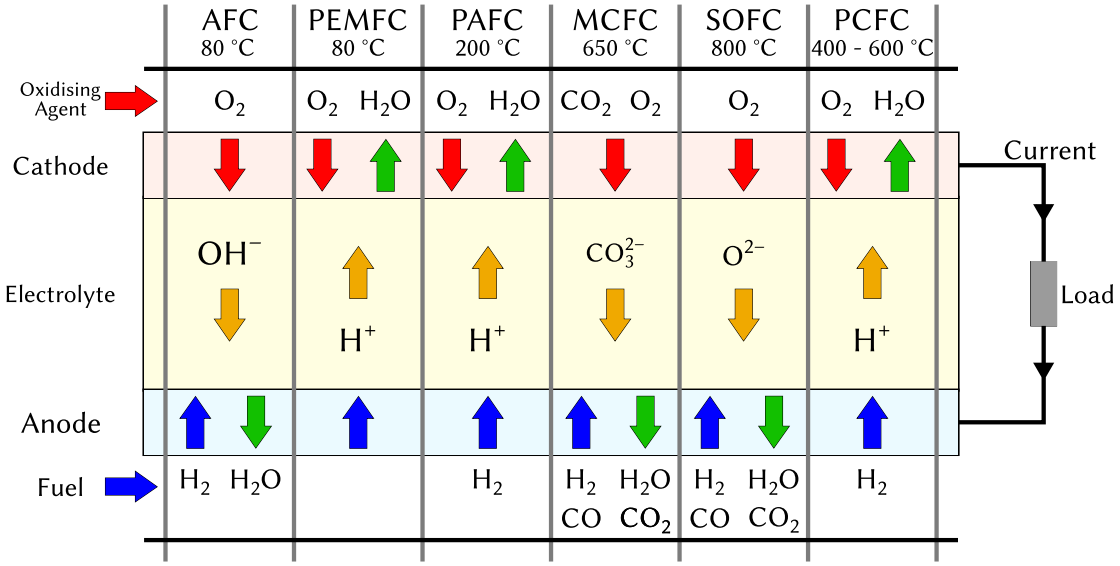

FIGURE 1.1.: Overview: Fuel cell types including operating temperatures, gas atmosphere (cathode - red, anode - blue), mobile ions (orange) and products (green).

SOFCs generally use dense, oxygen ion conducting ceramic electrolytes. High operating temperatures in the range of 600 - 900 °C are needed to achieve sufficient ionic conductivities. Those high temperatures and porous ceramic electrodes allow for fast electrochemical reactions without the use of noble metals. They also enable direct reforming of hydrocarbon fuels and the presence of CO does not impede the cell performance. Rather, CO can be used as a fuel. High overall fuel to electricity and heat efficiencies up to 75 % are achievable in cogeneration systems. The main drawbacks are related to the high operating temperatures (e.g. material degradation, long heat-up process) [7]. For building SOFC-stacks expensive heat-tolerant ceramics like $LaCrO_3$ or chromium based alloys are needed as interconnector materials, since the elevated operating temperature prevent the use of cost-effective ferritic steel [8].

As discussed above, the operating temperature of a fuel cell has a large impact on fuel cell performance, materials and fuel used, efficiency and the range of possible applications. Running PEMFCs at higher temperatures would result in better kinetics at the cathode, a higher tolerance for CO poisoning and a possible replacement of the expensive Pt catalysts. Lower operating temperatures in SOFC would result in longer life-spans due to slower material degradation, short heat-up times and the use of cheaper metals instead of expensive ceramics for certain components.

Development of such an intermediate temperature (400 - 600 °C) fuel cell could possibly fill this gap between PEMFCs and SOFCs. This kind of fuel cell would require new materials. Research in recent years has become more intense in order to find electrode and electrolyte materials with sufficient electronic and ionic conductivity in this temperature range. Among the most promising materials are proton-conducting ceramics [9–15].

The replacement of the typical oxide ion conductor with a proton conductor forms a so called proton ceramic fuel cell (PCFC). Proton conduction requires less thermal energy in comparison to their oxide ion counterparts. Thus, proton transport at lower temperatures (<600 °C) is still sufficiently fast. This change in charge carrier may also lead to a change in reaction mechanism, thus also requiring intensive research for possible electrode materials, which can utilise proton conduction. In this thesis, the focus lies on the anode site of such PCFCs. An in-depth summary of current state-of-the-art electrolyte and electrode materials of both, SOFC and PCFC, is provided in Sec. 2.3 for better understanding.

In conventional SOFCs, Ni/electrolyte composite materials are typically used as fuel gas electrodes. Naturally, similar materials of their PCFC counterparts are investigated, mainly barium and strontium zirconates and cerates in a composite with Ni [16–19]. However, studies on anode materials are scarce compared to electrolyte and cathode materials. Furthermore, research has mostly been done on porous electrodes, which may offer easier comparisons with real world application on the one hand. On the other hand, their complex morphology and ill-defined geometry impede mechanistic conclusions or straightforward material comparisons. In this thesis, dense, thin-film model cells are used to study the anode oxidation reaction in PCFCs. As an electrolyte proton conducting, yttrium- and cerium-doped barium zirconate, $BaZr_{0.8}Ce_{0.1}Y_{0.1}O_3$ (BZCY), was used. Another aspect to consider is the necessity of using a mixed ionic-electronic conductor (MIEC) in order to make the whole electrode surface area catalytically active.

The main goal of this thesis is to get mechanistic insight into the whole H_2 oxidation process on proton conducting MIECs. Various, similar perovskite-type materials based on the SOFC electrode material $La_{0.6}Sr_{0.4}FeO_3$ (LSF) [20] were synthesised. Model-type thin film electrodes were prepared from these by PLD and impedance spectra as well as current-voltage characteristics were recorded at various temperatures. To gain information on the rate determining step (*rds*) and to assess the rate of the ionic charge carrier for the H_2 oxidation, all electrochemical experiments were conducted on electrodes grown on proton conducting BZCY as well as oxide ion conducting YSZ electrolytes. Moreover, the basicity of oxide ions in the electrode materials was modified by different doping strategies (e.g. substitution of Sr^{2+} by Ba^{2+}) thus leading to

different proton concentrations in the materials. Since proton conducting materials also exhibit oxide ion and hole conduction in specific atmospheres [21] additional DC experiments were conducted in order to determine the transference number of each charge carrier. To draw comparisons between the electrode kinetics on proton conductors all experiments were also carried out on an oxide ion conductor.

2. Theoretical Background

2.1. Charge Transport in Ionic Solids

In general, crystalline materials are characterised by their repeating structures. Bravais showed that there area fourteen symmetrical ways of arranging points in a three dimensional Euclidian geometry as early as 1848. Nowadays, these are known as Bravais lattices [22]. They can be summarised in seven crystal systems, which only differ in the length of its base vectors and the interaxial angles. All possible crystal structures can be derived from these lattices, which define long-range symmetry.

Each lattice point accommodates an identical series of atoms known as the basis. In contrast to the aforementioned crystal systems the symmetry associated with the basis includes short-range elements such as reflections and rotations. It is commonly referred to point group symmetry. The addition of translational symmetry then builds up 230 distinct space groups. All crystals can be described by one of these space groups.

These descriptions are only perfectly correct for an ideal lattice. However, in this thesis we depart from these ideal crystals and will instead focus on defective crystalline solids.

Imperfect crystals originate from the fact that up to a certain concentration the presence of defects leads to a reduction of Gibb's free energy ΔG (see Eq. (2.1)). In order to create a defect a certain amount of energy ΔH is required. On the other hand a considerable increase in entropy ΔS can be expected, because of the large number of positions, which this defect can occupy. This means that up to a certain concentration the formation of defects is energetically favoured.

$$\Delta G = \Delta H - T\Delta S \tag{2.1}$$

Defects are often classified based on their size:

- **Point defects**: Involve only one atom or site (for example vacancies or interstitials)
- **Line defects**: Dislocations
- **Plane defects**: Defects, which span over a whole layer (e.g. grain boundaries)
- **Volume defects**: Point defect clusters

In ionic solids it is the point defects, which are primarily responsible for the transport of ions. Therefore, they hold a special position, which will be briefly introduced in the following subsection.

2.1.1. Point Defects

Point defects are subdivided in intrinsic and extrinsic defects. The former are an inherent property of a pure crystal. In contrast, the latter are caused by dopants or impurities. Either way most of the time one type of defect dominates, which then can have a major impact on physical or chemical properties of the material.

Defects and defect reactions are seldom depicted using standard chemical nomenclature. Kröger and Vink developed a notation, which is very useful for discussing point defects, the involved sites and the effective charges (see Eq. (2.2)) [23].

$$M_S^C \tag{2.2}$$

In this example of the Kröger-Vink-notation M describes the species, which can be an atom or an ion, an electron (e) or a hole (h) or an unoccupied lattice site (v), also called vacancy. The subscript S denotes the location of the species M. It shows the chemical symbols of the normal occupant of the site or an i if its an interstitial. Lastly the superscript C is the charge relative to the charge the same site would have had in an ideal structure. Therefore it can be either negative ($'$), neutral ($^{\times}$) or positive ($^{\bullet}$).

a) Intrinsic Defects

The aforementioned configurational entropy is the reason for the formation of intrinsic disorders. The most common types of intrinsic defects in ionic crystals are Schottky and Fenkel disorders - a sketch of both is shown in Fig. 2.1.

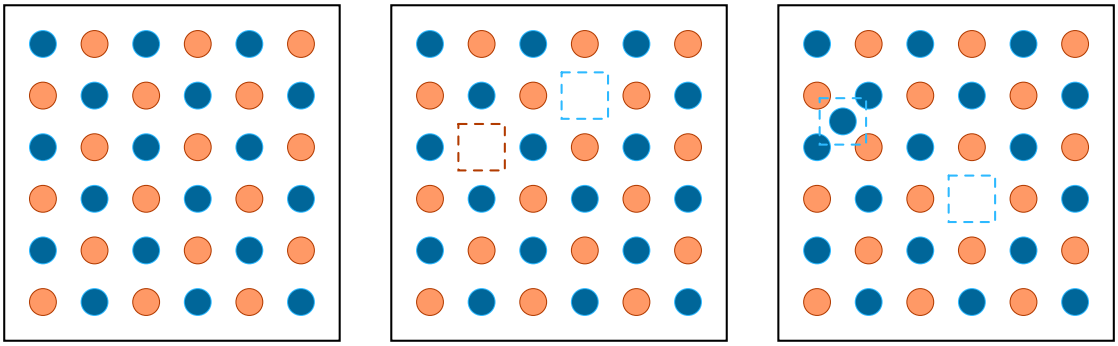

Figure 2.1.: Schematic showing (a) an ideal crystal (b) Schottky disorders and (c) Frenkel disorders

In case of the Schottky disorders both an cation and anion lattice site is unoccupied to preserve local electroneutrality. These defects are the predominant point defects in alkali halides. For intrinsic NaCl at room temperature, typically one in 10^{15} of the sites is vacant.

Compared to Schottky disorders Frenkel disorders also involve interstitials in the crystal structure. An atom of one sublattice creates a vacancy and is place in an interstitial site in the crystal. Like before, electroneutrality is preserved. For example AgCl has predominantly Frenkel disorders with vacant interstitial Ag sites (v'_{Ag} and $Ag_i^{\bullet}$, respectively). So called Anti-Frenkel disorders can occur if anion instead of cations occupy the interstitial sites (e.g. CaF_2 with $v_F^{\bullet}$ and F_i').

b) Extrinsic Defects

As mentioned before extrinsic defects are either impurities or dopants. The former are undesired, who can complicate the interpretation of experimental data. The latter are desired and added with a purpose in mind. In most cases the goal is to either introduce a new property or further enhance an already existing kind. In doped ceramics the intrinsic defects can often be neglected due to their small concentrations compared to their extrinsic counterparts.

In general there are two kind of dopants:

- **Donor dopants**, which are cations in higher valence compared to the host-lattice cations and therefore relatively positive charged. Charge neutrality can be preserved via generation of electrons, cation vacancies or anion interstitials.
- **Acceptor dopants** have a lower valence than the lattice cations they replace, which results in a negative relative charge. They are balanced with electron holes, cation interstitials or anion vacancies.

In electrochemistry ceramics are often doped in order to enhance electronic or ionic conductivity. For example, the most commonly used electrolyte material in SOFCs is yttria-stabilised zirconia, which is ZrO_2 doped with Y_2O_3 as shown in Eq. (2.3).

$$Y_2O_3 \xrightarrow{ZrO_2} 2\,Y'_{Zr} + v_O^{\bullet\bullet} + 3\,O_O^{\times} \tag{2.3}$$

By replacing Zr^{4+} cations in the ZrO_2 lattice by Y^{3+} cations, oxygen vacancies are formed to maintain charge neutrality. Because of these vacancies oxide ions are mobile at high temperatures, which allow them to move through the lattice. Furthermore, the addition of yttria stabilises the cubic modification of ZrO_2.

c) Non-Stoichiometry

Other than extrinsic and intrinsic defects there is another important factor when considering point defects: non-stoichiometry. An oxide, for example, equilibrates with the surrounding atmosphere at sufficiently high temperatures. For high oxygen partial pressure, oxygen can be incorporated into the lattice by consuming vacancies and electrons according to Eq. (2.4).

$$\frac{1}{2}\,O_2 + v_O^{\bullet\bullet} + 2\,e' \longrightarrow O_O^{\times} \tag{2.4}$$

At low oxygen partial pressure, oxygen is released from the lattice forming a vacancy and leaving two electrons behind (see Eq. (2.5)).

$$O_O^{\times} \longrightarrow \frac{1}{2} O_2 + v_O^{\bullet\bullet} + 2\,e' \tag{2.5}$$

All aforementioned charge carrier concentrations can be summarised in a so called Brouwer diagram. There, defect concentrations are shown as a function of oxygen partial pressure for a given temperature. Fig. 2.2 depicts this diagram[1] at 600 °C for LSF based on the thermodynamic data of *Kuhn et al* [24].

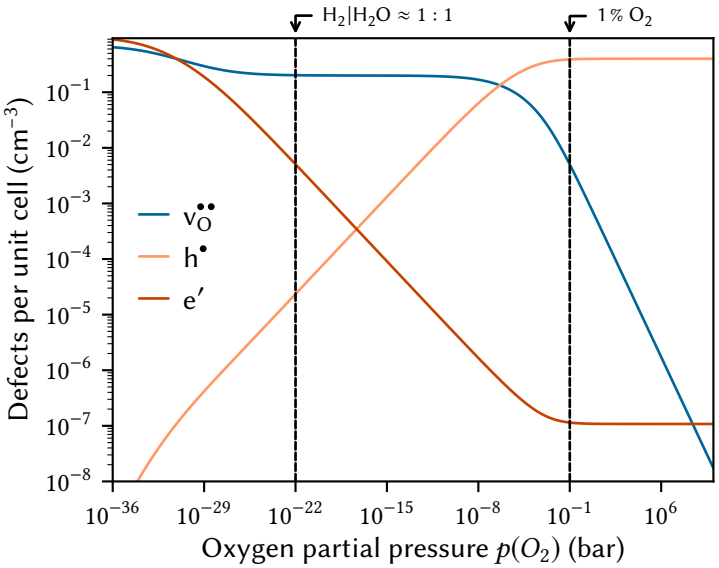

Figure 2.2.: Brouwer diagram of LSF

Ionic defects can have a substantial impact on the volume of the crystal. Vacancies as well as polarons (electronic defects localised on an ion) can increase the lattice constant due to their repulsion of ions with equal charges on neighbouring sites. Furthermore, temperature and the surrounding atmosphere also have a large effect on the formation of such defects. Electrons and holes are needed in order to preserve charge neutrality. Thus, oxides with cations of multiple stable valence states have a higher probability to show non-stoichiometry.

[1] calculated by Alexander Schmid

2.1.2. Mass and Charge Transport

The electrochemical potential $\tilde{\mu}_i$ of a particle i is composed of the chemical potential μ_i of this particle and the electrical potential φ including the charge number z_i and the elementary charge e as shown in Eq. (2.6). As long as the thermodynamic equilibrium is maintained the electrochemical potential remains constant.

$$\tilde{\mu}_i = \mu_i + z_i e\varphi \tag{2.6}$$

Disruptions of this equilibrium lead to a particle flux J_i, which is opposed to the resulting gradient in $\tilde{\mu}_i$. This fundamental transport equation is shown in Eq. (2.7) [25, 26].

$$J_i = -\frac{\sigma_i}{z_i^2 e^2}\nabla\tilde{\mu}_i \tag{2.7}$$

The electrical conductivity σ_i in Eq. (2.7) is proportional to the concentration c_i and the mobility u_i of the charge carrier (Eq. (4.2)).

$$\sigma_i = |z_i| e c_i u_i \tag{2.8}$$

Eq. (2.7) and Eq. (2.8) are both valid for both electronic defects (electrons and holes) and ionic defects (vacancies and interstitials). The resulting total conductivity σ_{tot} is then given as the sum of all contributions (see Eq. (2.9)).

$$\sigma_{tot} = \sum_k \sigma_k = \sigma_{cation} + \sigma_{anion} + \sigma_{electrons} + \sigma_{holes} \tag{2.9}$$

In general, the movement of ionic defects is a thermally activated hopping process [27, 28]. The aforementioned mobility of a particle is thus strongly dependent on the temperature. Assuming a constant charge carrier concentration (which is the case for extrinsic defects), the same is true for the conductivity, which is then given by Eq. (2.10):

$$\sigma = \sigma_0 \exp\left(-\frac{E_a}{k_B T}\right) \tag{2.10}$$

The pre-exponential factor σ_0 therein denotes the conductivity if every jump were to be successful and the exponential part assumes the role of the success probability. It includes the activation energy E_a of the process, the Boltzmann constant k_B and the temperature T. The former represents the energy barrier, which has to be overcome for a successful jump from one lattice site to a neighbouring one. The logarithmic form of Eq. (2.10) allows the determination of E_a (see Eq. (2.11)), which is - due to its temperature dependence - a key parameter of a material.

$$\ln(\sigma) = \ln(\sigma_0) - \frac{E_a}{k_B}\frac{1}{T} \tag{2.11}$$

In so called Arrhenius-Plots the logarithm of the conductivity is plotted versus the inverse temperature. The activation energy is then calculated from the slope of the resulting line of Fig. 2.3 for an arbitrary example.

The activation energy E_a fulfils an important role as a measure of temperature dependence of the ionic conductivity. Resistances due to electrode processes (e.g. incorporation of oxygen into a crystal lattice) are also thermally activated. Activation energies in these cases can be used as a measure of the temperature dependence and therefore play a key role in the characterisation of the kinetic parameters.

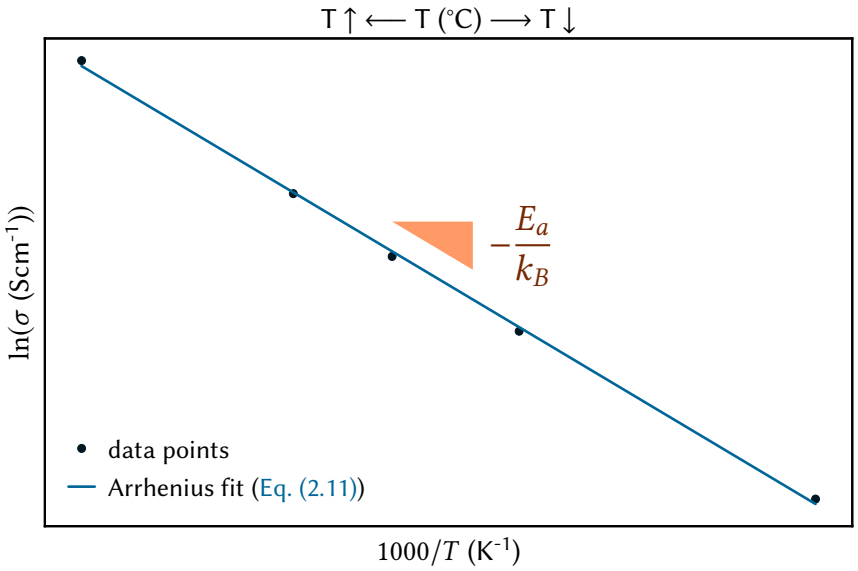

Figure 2.3.: Example of an Arrhenius plot.

2.2. Perovskite: Structure and Defects

All electrode materials used in this thesis crystallise in the perovskite structure. The general formula is ABX_3, where A is a large cation, B a smaller cation and X oxygen or a halogen. The charges of the cations ranges from +1 to +5. Fig. 2.4 illustrates both a B- and A-centred view of the crystal structure. The former can be described as A and X ions forming a cubic closed packed lattice with B ions occupying the octahedral holes created by the oxygen. The structure also has a three dimensional network of corner sharing $[BX_6]$ octahedra with A ions in the twelve fold cavities in between the polyhedra. Temperature or other external parameters can easily break the idealised cubic symmetry, which leads to distorted octahedra and tetragonal or orthorhombic symmetry.

In addition, a wide variety of cations in a multitude of combinations can occur. In the case of doped perovskites different cations occupy the same site. The properties of a perovskite are strongly influenced by the types of cations and their ratios as well as oxygen partial pressure and temperature. This opens up the possibility for a wide variety of applications. Some exhibit ferro- or piezoelectricity and are thus of big interest for optoelectronic devices. In fuel cell research the significance of being able to conduct ions and/or electrons allows for usage as potential electrolyte and electrode materials.

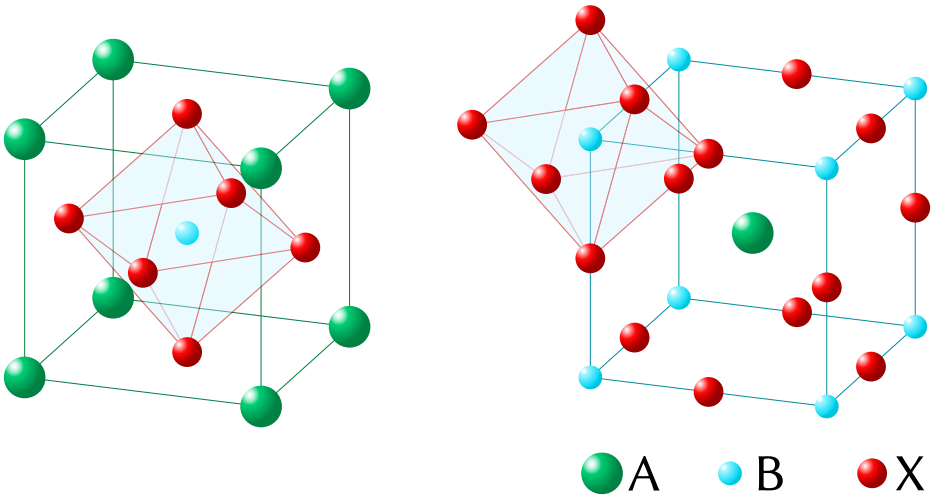

Figure 2.4.: Two representations of a cubic perovskite showing either the B- (left) or A-centred unit cell.

2.3. PCFC vs. SOFC

The basic operating principle of fuel cells has already been explained in Ch. 1. In this section the focus lies on the main differences between SOFCs and PCFCs including state of the art materials. While the net reaction for both fuel cell types remains the same, the underlying elementary processes such as the mobile ions responsible for charge carrier transport in the electrolyte differ. In general, fuel in the form of H_2 is oxidised and oxygen is reduced yielding water vapour as the product (see Eq. (2.12)).

$$H_2 + \frac{1}{2} O_2 \rightleftharpoons H_2O \tag{2.12}$$

The general working principle of a SOFC is shown in Fig. 2.5. Fuel enters the cell through the inlet manifold at the anode. In the same way air is introduced at the cathode.

The latter is also called air electrode. Oxygen O_2 from the atmosphere dissociates and reacts with electrons e' and vacancies $v_O^{\bullet\bullet}$ forming oxygen ions $O_O^{\times}$ (see Eq. (2.13)). They then move to and through the electrolyte.

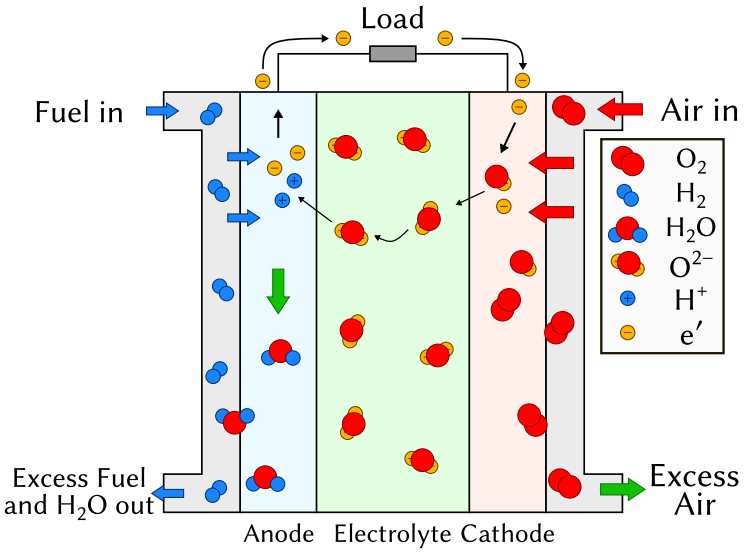

Figure 2.5.: Working principle of a SOFC.

$$\frac{1}{2}\,O_2 + v_O^{\bullet\bullet} + 2\,e' \longleftrightarrow O_O^{\times} \tag{2.13}$$

Criteria such as low polarisation resistance, high electronic conductivity and mechanical strength or compatibility are important for cathode materials. $La_{1-x}Sr_xMnO_3$ (LSM) is the most commonly used material due to matching thermal expansion coefficients with the electrolyte and relatively high electronic conductivity after doping [29, 30]. A popular alternative is the mixed conductor $La_{1-x}Sr_xCo_yFe_{1-y}$ (LSCF), which offers low polarisation losses but suffers from degradation issues [31, 32].

The transport of oxygen through an oxide is a well-studied process. Due to the size of the ions it is impossible to move via interstitial sites. Instead, the oxygen ions hop through vacant oxygen sites. In general, one has to consider not only the opportunity to move (e.g. a vacancy in the vicinity) but also having enough energy to successfully complete the movement. This existing energy barrier also gives vacancy diffusion its exponential temperature dependence (see also Eq. (2.11) and the related text). The most common electrolyte used in SOFCs is yttria-stabilised zirconia (YSZ), which [33]. Due to the aforementioned temperature dependence operating temperatures of around 600 to 900 °C or higher are necessary (depending on the thickness of the electrolyte).

At the anode the incoming fuel H_2 and surface oxide ions $O_O^\times$ form water vapour H_2O, leaving a vacancy $v_O^{\bullet\bullet}$ and two electrons e' (see Eq. (2.14)). Both move back to the cathode, the vacancies via the electrolyte and the electrons via the external circuit.

$$H_2 + O_O^\times \longleftrightarrow H_2O + v_O^{\bullet\bullet} + 2\,e' \tag{2.14}$$

The most common state-of-the-art SOFC anode material is porous Ni/YSZ due to its low cost and high chemical stability at operation temperatures. While Ni acts as a catalyst for the H_2 oxidation and provides the electronic conductivity, YSZ offers the ionic contribution to the conductivity as well as prevents the coarsening of the Ni particles [34]. However, Ni/YSZ anodes also have significant drawbacks such as vulnerability for carbon deposition (coking), low resilience against H_2S containing fuels (sulphur poisoning), and a limited redox-cycling stability [35]. Thus, alternatives like ceramic anodes are investigated. $La_{1-x}Sr_xFeO_3$ (LSF) is a suitable model-type MIEC-anode, provided a metal current collector is placed beneath the oxide [20]. LSF is sufficiently stable under humid reducing atmospheres, its defect chemistry is known and well behaved [24, 36].

Just like in a SOFC, in PCFCs the fuel is added at the anode, while the oxidant enters at the cathode. The electrolyte represents the main difference compared to a SOFC, since protons are the main mobile ionic species. The working principle is shown in Fig. 2.6. While the interest in PCFC has increased in recent years, research regarding materials is still in its infancy and often purely empirical.

At the anode mobile protons can be incorporated from molecular hydrogen H_2 according to Eq. (2.15). The protons bond with two lattice oxygen ions $O_O^\times$ forming hydroxide defects $(OH)_O^\bullet$ and releasing electrons e'.

$$H_2 + 2\,O_O^\times \longleftrightarrow 2\,(OH)_O^\bullet + 2\,e' \tag{2.15}$$

However, the dissociation of water is considered the most important reaction leading to high concentrations of protonic defects: H_2O from the gas phase dissociates into a hydroxide ion and a proton [37]. The former fills an oxygen vacancy $v_O^{\bullet\bullet}$ and the latter bonds to a lattice oxygen (see Eq. (2.16)).

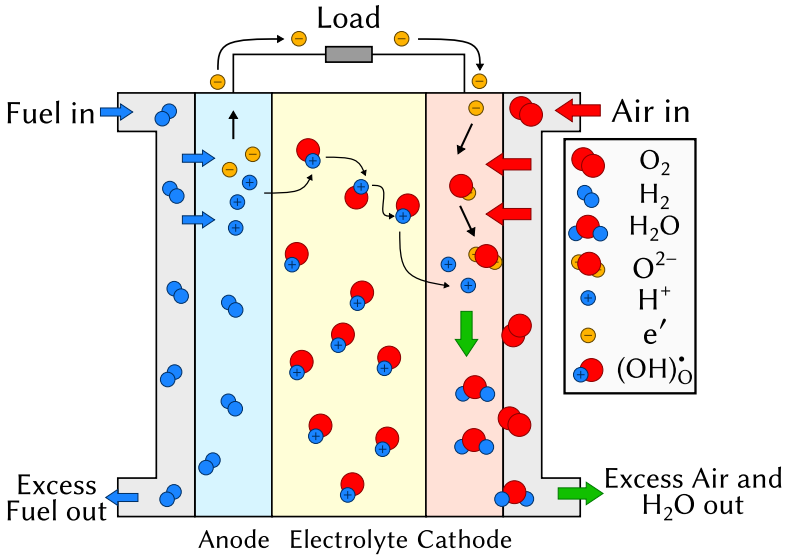

Figure 2.6.: Working principle of a PCFC.

$$H_2O + O_O^{\times} + v_O^{\bullet\bullet} \longleftrightarrow 2\,(OH)_O^{\bullet} \tag{2.16}$$

Similar to conventional SOFCs most PCFCs utilise composite anodes as fuel electrodes. In general they consist of Ni and the HTPC of the electrolyte. Research in this field has received little attention so far. While Ni offers the same advantages as in SOFC, there are still problems such as agglomeration, coking, sulphur poisoning, and limited redox-cycling stability, which all would deteriorate the anode performance with time [38].

The generally accepted mechanism for proton diffusion in perovskite oxides differs greatly from the oxygen vacancy mechanism in YSZ. In fact, it resembles the behaviour in solutions and therefore follows a hopping mechanism [39, 40]. The transfer of a proton is between two lattice oxygen ions, where the proton is passed from one site to the other. The steps are as follows:

1. Rotational motion around the oxygen
2. Bending of the Zr-O bond
3. Hopping of the proton to the neighbouring oxygen

The most common electrolyte materials are based on barium cerates or zirconates. The former shows the best performance in terms of proton conductivity. However, they easily react with acidic gases like CO_2 and H_2O forming carbonates and hydroxides [16]. The latter is a serious drawback since steam is inevitably generated at the cathode in a PCFC [5]. Zirconates on the other hand offer high chemical stability but lower proton conductivity than the cerate-based materials. Furthermore, it has been reported that the basicity is a key parameter with regards of the proton uptake [41]. Also, in high oxygen partial pressures p-type conductivity $h^\bullet$ has to be expected (see Eq. (2.17)):

$$\frac{1}{2}\,O_2 + v_O^{\bullet\bullet} \longleftrightarrow O_O^\times + 2\,h^\bullet \tag{2.17}$$

At the cathode the protonic defects $(OH)_O^\bullet$ and oxygen from the atmosphere O_2 form water vapour H_2O. Two electrons e' from the external circuit take part in the reduction, while two lattice oxide ions $O_O^\times$ are restored. This shows one of the main differences between SOFC and PCFC. Now, steam is produced at the cathode, which prevents fuel dilution.

$$2\,(OH)_O^\bullet + \frac{1}{2}\,O_2 + 2\,e' \longleftrightarrow H_2O + 2\,O_O^\times \tag{2.18}$$

In general, the most desirable cathode material should be a mixed proton/electronic conductor. So far, no material has been found, which satisfies this prerequisite [42]. Instead, researchers are looking at composites made of a proton and an oxygen/electron conductor. First tests have been reported using the already mentioned LSCF in conjunction with a HTPC material [43]. $Ba_{0.5}Sr_{0.5}Fe_{0.8}Zn_{0.2}O_{3-\delta}$ (BFSZ) is another MIEC, which is considered as a possible cathode material [44].

2.4. Measurement Techniques

2.4.1. Electrochemical Impedance Spectroscopy (EIS)

Electrochemical Impedance Spectroscopy is a powerful technique, which can be used in a wide range of applications. Today it is the most practical tool of electrochemists for investigating mechanisms of electrochemical reactions or measuring dielectric and transport properties of materials [45]. Other advantages besides its broad field of use include a relatively simple experimental setup and the fact of it being a non-destructive method. While the recording of spectra is straightforward the difficult interpretation afterwards is actually the major disadvantage.

As the name implies, EIS is the measurement of the frequency dependent AC resistance, the impedance Z, in an electrical system. As general principle a small AC potential $u(t)$ is applied to an electrochemical cell. Subsequently, the current response $i(t)$ of the system to this perturbation is measured. The impedance can be expressed in terms of a magnitude Z_0 and a phase shift ω (Eq. (2.19)), where ω is the angular frequency and $\hat{U}$ and $\hat{I}$ the amplitude of potential and the resulting current, respectively.

$$Z = \frac{u(t)}{i(t)} = \frac{\hat{U}\sin(\omega t)}{\hat{I}\sin(\omega t + \varphi)} = Z_0 \frac{\sin(\omega t)}{\sin(\omega t + \varphi)} \tag{2.19}$$

Using Euler's relationship (Eq. (2.20)) where $j = \sqrt{-1}$ the impedance Z can be expressed as a complex number as shown in Eq. (2.21). Therefore, the Z is composed of a real and imaginary part, which will be important later on.

$$e^{i\varphi} = \cos(\varphi) + j\sin(\varphi) \tag{2.20}$$

$$Z = \frac{\hat{U}e^{j\omega t}}{\hat{I}e^{j\omega t+\varphi}} = Z_0 e^{-j\varphi} = Z_0(\cos(\varphi) + j\sin(\varphi)) \tag{2.21}$$

In the case of a resistor there is no phase shift between potential and current. Thus, the impedance Z_R has no imaginary part and equals the frequency-independent resistance R (see Eq. (2.22)). In electrochemistry the charge transport through a material (ionic or electronic) or the charge transfer across an interface can be described by a resistance.

$$Z_R(\omega) = R \tag{2.22}$$

For a capacitor only a frequency-dependent imaginary part but no real part can be found. Therefore, the impedance of a capacitor Z_C is given by Eq. (2.23), where C is the capacitance.

$$Z_C(\omega) = \frac{1}{j\omega C} \tag{2.23}$$

In reality most system do not behave like ideal elements. To take this into account constant phase elements (*CPE*) are used instead of a traditional capacitor. Their impedance Z_{CPE} is given by Eq. (2.24). The factor n is frequency-independent and can have values between 0 and 1. In the latter case the parameter Q equals C of an ideal capacitor.

$$Z_{CPE} = \frac{1}{(j\omega)^n Q} \tag{2.24}$$

Eq. (2.25) shows the relation between Q and C [46], which is then used to estimate a typical capacitance from the CPE.

$$C = \left(R^{(1-n)}Q\right)^{\frac{1}{n}} \tag{2.25}$$

Just like in DC measurements Kirchhoff's laws apply to characterise networks of multiple elements. One of the most common networks in EIS is the parallel circuit of a resistor and a capacitor called RC element. Its impedance Z_{RC} can be expressed as:

$$Z_{RC}(\omega) = \left(\frac{1}{Z_R} + \frac{1}{Z_C}\right)^{-1} = \frac{R}{1 + j\omega RC} \tag{2.26}$$

After the recording of impedance spectra they can be visualised in various ways. In this thesis the so called Nyquist plots are used, where the imaginary part of the impedance Z_{IM} is plotted versus the real part Z_{RE}. In Fig. 2.7 an example of such a diagram can be seen.

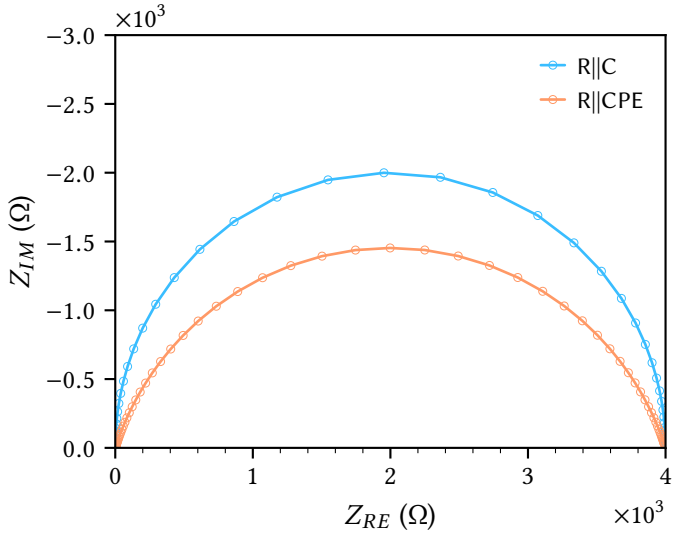

Figure 2.7.: Example of a simulated R||C element (blue) and an R||CPE (orange, with $n = 0.8$) in a Nyquist plot.

For interpretation of impedance spectra so called equivalent circuits (EC) are modelled. By a complex non-linear least-squares (CNLS) fit, parameters such as resistance R or capacitance C can be extracted. The equivalent circuits for both curves in Fig. 2.7 are shown in Fig. 2.8. They consist of a resistor in conjunction with either a R||C element or a R||CPE element. Simulated spectra corresponding to both circuits are given in Fig. 2.7 by the blue and orange curve, respectively.

(a) EC of a R||C **(b)** EC of a R||CPE

Figure 2.8.: Equivalent Circuit of an ideal R||C element an a R||CPE element

2.4.2. Mass Spectrometry (MS)

Mass spectrometry is a powerful analytical technique used to identify unknown compounds within a sample, quantify known materials or elucidate the structure and chemical properties of different molecules. The usefulness of MS has risen even further with the introduction of hyphenated techniques such as LC-MS (liquid chromatography-mass spectrometry).

The main components of a MS are shown in Fig. 2.9. The sample is introduced via the inlet. The following ion source ionises the analytes and partly fragments larger molecules into smaller pieces, which are then accelerated into an analyser. There they are separated according to the mass to charge ratio (m/z). Afterwards the ion current of the desired m/z are detected. An extensive vacuum system for sample inlet, ion source, analyser and detector is needed. Otherwise, collision of gas particles and fragment ions would occur. In the following a brief overview over all components will be given. The explanation will be focused on the components of the employed mass spectrometer.

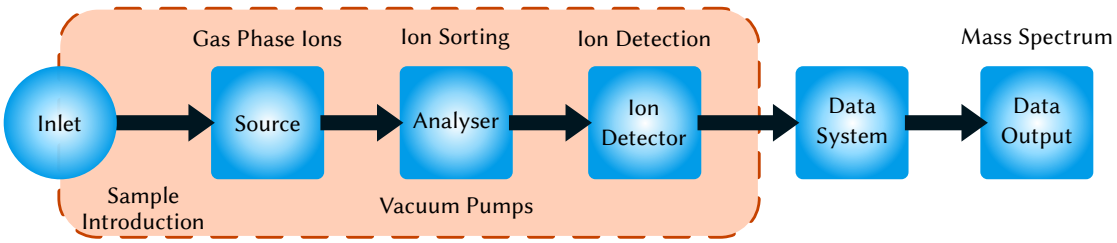

Figure 2.9.: Components of a Mass Spectrometer

In most cases the sample inlet system is coupled to the ion source. There, the samples are evaporated and subsequently ionised. In general there are various types of ionisation sources, which can be roughly classified in 'hard' and 'soft' ion sources. The former uses high energy and also yields fragment ions whereas the latter leaves the sample mostly intact. Examples

for soft ion sources are: chemical ionisation (CI), field ionisation (FI) or electrospray ionisation (ESI). In this work the hard ion sources electron ionisation (EI) is used, where high energy electrons collide with the sample M and expel an electron to form a positive ion:

$$M + e^- \longrightarrow M^{+\bullet} + 2\,e^- \tag{2.27}$$

Electrons are produced by thermionic emission of a heating filament (cathode), which has an electric current running through it. The sample is introduced in a perpendicular orientation to the electron beam. The kinetic energy of the electrons has to be higher than the ionisation energy of the molecule. In commercial systems electrons are accelerated to the anode with up to 70 eV. Based on the amount of excess energy after the collision the sample can fragment into various 'daughter ions'. After ionisation the ions are accelerated and focused by a set of lenses, which lead to the mass analyser. Fig. 2.10 shows a schematic of an EI source.

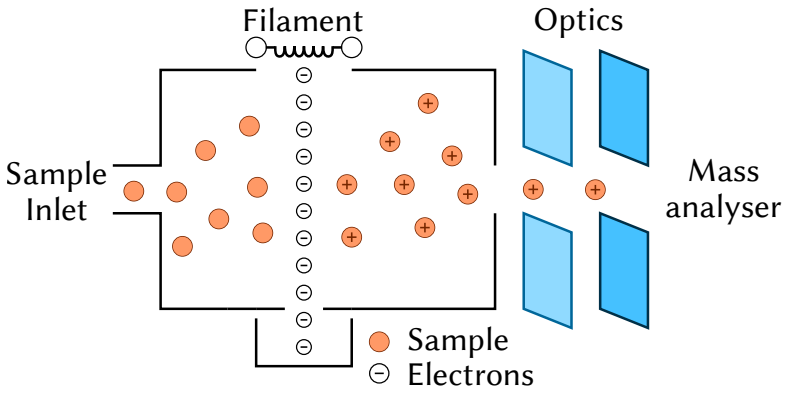

Figure 2.10.: Working principle of an Electron Ionisation (EI) source

Mass analysers separate the ions based on their mass to charge ratio (m/z). There are multiple ways to achieve this. One of the most important parameters of a mass analyser is its resolution R. It is defined as the ratio of the mass number m and the difference Δm to a second ion of the mass number $m + \Delta m$ (see Eq. (2.28)). In general, two signals are considered to be separated if the valley beneath two overlapping peaks is smaller than 10 % of the peak height of the weaker signal.

$$R = \frac{m}{\Delta m} \tag{2.28}$$

Tab. 2.1 lists the most common types of analysers and their principle of separation. It also shows the typical achievable resolution.

Table 2.1.: Types of mass analysers and their principle of separation

Analyser	Principle of separation	Resolution
Quadrupole	Trajectory stability	< 5000
Magnetic Sector	Magnetic field	$5 \cdot 10^4$
Electrostatic Sector	Kinetic Energy	1000
Ion trap	Resonance frequency	10^4
Time-of-flight	Flight time	$2 \cdot 10^4$
Ion Cyclotron Resonance (ICR)	Resonance Frequency	10^6

The most common mass analyser, which is also used in this work, is the quadrupole mass filter (Q). It consists of four parallel metal rods arranged in a square (see Fig. 2.11). Two opposite rods have a DC component U superimposed with a AC voltage $V_O \cos(\omega t)$. A negative DC potential $-U$ and AC potential $-V_O \cos(\omega t)$ is applied to the other rods. The trajectory of ions coming from the ion source is affected by the applied potential as they travel along the rods. For given DC and AC voltages, only ions of a certain mass to charge ratio can pass through the quadrupole and reach the detector. The unstable trajectory of the other ions ensure that they collide with one of the rods and get filtered out.

The popularity of quadrupoles stem from their compact format and ease of use. Resolution-wise they are adequate for lots of application, but not on the level of other analysers. They also exclusively operate in sequential mode, which is balanced by short scan times (<100 ms per m/z value).

The separated ions are registered as an ion current at the detector, for which multiple options are available. In secondary electron multipliers (SEM) the incident ion beam generates secondary electrons when impacting on shaped pieces of sheet metal. The resulting electrons then are guided to another in series connected stages. Eventually, an avalanche of electrons coming from a single ion get detected. They are especially useful in measuring extremely small currents due to the inherent amplification.

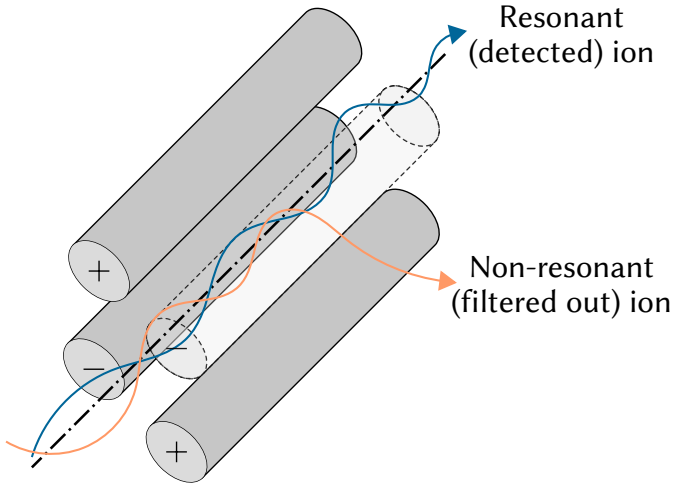

Figure 2.11.: Working principle of a quadrupole mass analyser

The detector used in this work has an even simpler design, which is shown in Fig. 2.12. This Faraday cup is in the most simple cases an electrically conductive material in the shape of a cup. It is placed in the path of the charged particle beam whose current is to be measured. In the best case all particles in the beam are absorbed by the Faraday cup. They induce a charge on the cup that leads to a current to ground, which can be measured by means of appropriate electronics. Excluding any kind of losses the current passing through the Faraday cup is a direct continuation of the charged particle beam. The cup basically acts as an resistor, therefore, the current read out from the Faraday cup is equal to the beam current.

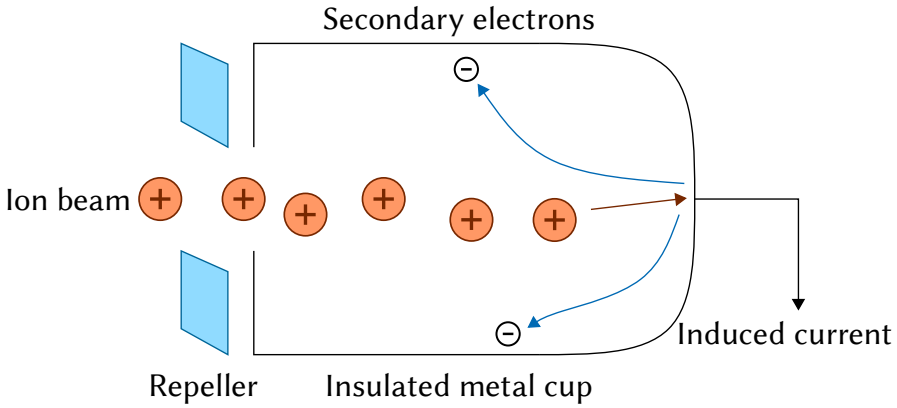

Figure 2.12.: Working principle of a Faraday cup

The goal of a Faraday cup is to completely absorb all of the charged particles in the incident beam and to fully encapsulate the electromagnetic cascade. The absorbed charge should accurately correspond directly to the charge in the incident beam. In most cases the energy of the incident ions is much higher than the work function of the metal. Thus, secondary electrons are generated. To prevent these electrons from leaving the cage and distort the measured current a repeller plate on a negative potential is placed at the entry hole. The biggest advantage of a Faraday cup lies in its simplicity and robustness. Compared to SEMs, however, the sensitivity is much lower.

3. Experimental

3.1. Target Preparation and Characterisation

In order to deposit thin film electrodes on a suitable electrolyte material via pulsed laser deposition (PLD) different targets were prepared. The desired composition and their abbreviation used throughout this thesis are shown in Tab. 3.1. The powders were either directly purchased (LSF) or synthesised.

Table 3.1.: Abbreviations and stoichiometric compositions of all electrode materials

Abbreviation	Stoichiometric Composition	Source
LSF	$La_{0.6}Sr_{0.4}FeO_3$	Sigma Aldrich
LSBF	$La_{0.6}Sr_{0.3}Ba_{0.1}FeO_3$	synthesised in-house
BLF	$Ba_{0.9}La_{0.1}FeO_3$	synthesised in-house

In the case of LSBF, Fe_2O_3 (99.998 %, Alfa Aesar), La_2O_3 (99.999 %, Sigma Aldrich), BaO (99.99 %, Sigma Aldrich), and SrO (99.9 %, Sigma Aldrich) were used as starting materials. The reactants were weighted in their desired amounts and thoroughly grounded for 1 h. The powder was then calcinated for 3 h at 900 °C and again grounded for 30 min. Afterwards, it was isostatically pressed and sintered at 1200 °C for 12 h yielding a target suitable for PLD.

For BLF, the powder was prepared via the Pechini method [47]. After weighing, the starting materials were dissolved in HNO_3 (65 %, Merck). Cation complexes were formed by adding of citric acid in a ratio of 1:1.1. After evaporation of H_2O the resulting gel was heated until self-ignition took place. The resulting powder was then objected to the same heat treatment as described in the case of LSBF. Phase purity of the targets was verified via X-ray diffraction (XRD) using a X'Pert PRO Diffractometer (PANalytical, Almelo/NL) (see Subsec. Subsec. 4.1.1).

3.2. Sample Preparation

3.2.1. Samples for Electrolyte Characterisation

Disc shaped $BaZr_{0.8}Ce_{0.1}Y_{0.1}O_3$ (BZCY) electrolytes were purchased at NORECS (Norway) having a diameter of around 17 mm and thickness of 1 mm and a relative density of around 99 %. The general workflow of the sample preparation procedure for electrolyte characterisation is shown in Fig. 3.1.

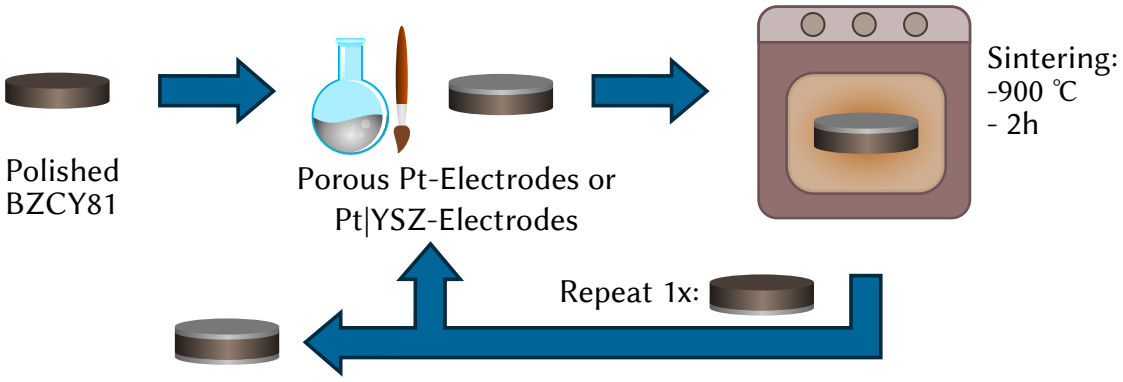

Figure 3.1.: Workflow of the sample preparation for the electrolyte characterisation: Deposition of porous Pt-electrodes on both sides and sintering at 900 °C for 2 h.

The obtained BZCY samples were ground and polished by hand using a SiC grinding paper of rising granulation (starting with 500 and ending with 4000 mesh). Afterwards platinum paste was applied on both parallel surfaces. Then, the sample was sintered for 2 h at 900 °C to ensure good adhesion of the Pt on the electrolyte surface. The whole procedure was repeated on the back of the sample. Due to poor attachment of the paste to the pellet surface the whole procedure was repeated with a Pt|YSZ cermet paste.

3.2.2. Macroscopic Electrodes for Symmetric Samples

The general workflow of the sample preparation for the AC experiments with macroscopic cells on symmetric electrodes is shown in Fig. 3.2.

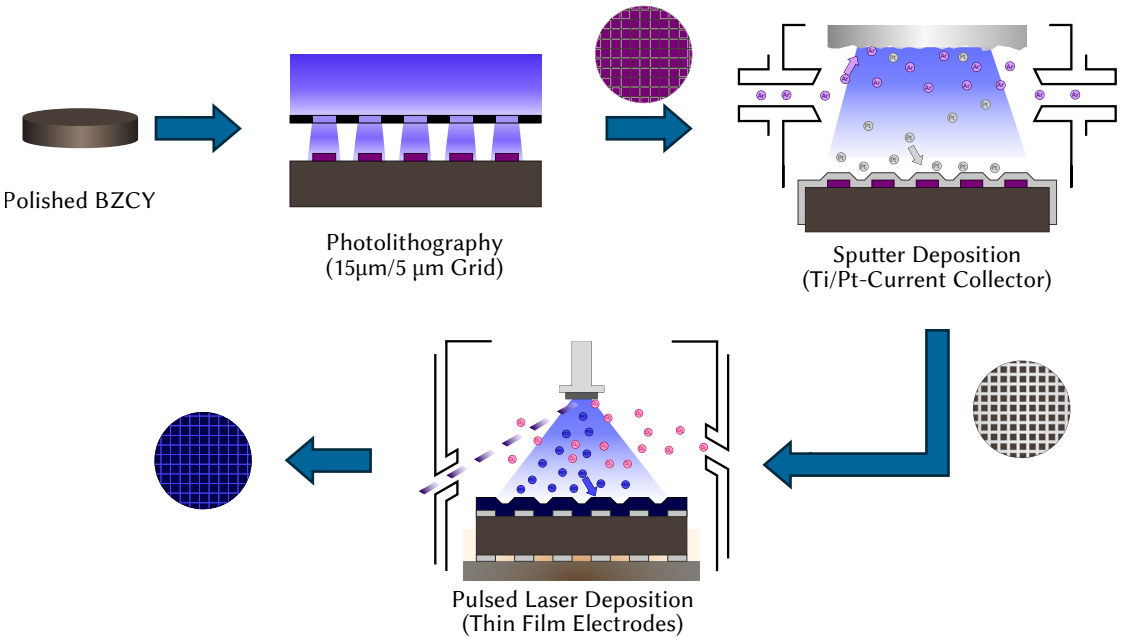

Figure 3.2.: Workflow of the sample preparation for the symmetric cells with macroscopic electrodes: Ti/Pt current collector grid is deposited on the polished sample via photolithography and magnetron sputtering. Symmetric cells with thin film electrodes are obtained via pulsed film deposition.

Prior to electrode thin film deposition the BZCY samples were ground and polished by the same procedure as mentioned in Subsec. 3.2.1. To allow comparisons with kinetics of an oxygen ion conducting electrolyte the following steps were also carried out on a (100)-oriented, polished double side, 10 mm × 10 mm × 0.5 mm YSZ single crystal, obtained from Crystec (Germany).

To ensure homogeneous polarisation of the MIEC-electrode surface, platinum grids were used as current collector (5 µm strips, 15 µm spacing). They were produced via lift-off photolithography and magnetron sputtering. A thin 5 nm titantium layer between the substrate and the platinum was deposited in order to improve adhesion.

For photolithography, the sample was coated with a photoresist (N-1430 MicroResist Technology, Germany) by a spin-coater (SCC-200 KLM, Germany). After pre-baking and applying the desired mask to shade areas, where Pt has to be deposited, the resist was polymerised by UV exposure (350 W, USHIO 350DP, Hg, Ushio, Japan). Removing of uncured structures was done by immersing the sample in a developer solution (MicroResist Technology, Germany). The parameters of the whole process are shown in Tab. 3.2.

Table 3.2.: Photolithography parameters used for the fabrication of the current collector grids

Parameters: Photolithography	
Photoresist volume	150 µl
Spincoater (speed/duration)	75 s^{-1}/45 s
Prebaking	10 min at 100 °C
UV Exposure time	60 s
Developing time	40 to 60 s

The Ti/Pt thin films were then deposited via a MED 020 Coating System machine (BAL-TEC Germany). The specific parameters of the depositions can be found in Tab. 3.3. Afterwards, the whole procedure was repeated on the other side of the substrate to get symmetric cells.

Table 3.3.: Sputtering parameters used for the fabrication of the current collector grids

Parameters: Sputtering		
Target	Titanium	Platinum
Target distance (cm)	6	6
Sputter current (mA)	100	100
Argon pressure (mbar)	0.0073	0.02
Sputter time (s)	57	150
Thickness (nm)	5	100

The mixed-conducting thin film electrodes of approximately 200 nm were deposited via pulsed laser deposition. A Kr/F exicmer laser (COMPex Pro 201F) was used for ablation of the target. All relevant parameters of the process are shown in Tab. 3.4. Just like before, thin films were deposited on both sides of the electrolyte substrate.

Table 3.4.: PLD parameters used for the deposition of the electrode films

Parameters: PLD	
Laser wavelength (nm)	248
Laser energy/pulse (mJ)	400
Pulse frequency (Hz)	5
Deposition time (min)	30
Deposition temperature (°C)	600
O_2 partial pressure (mbar)	0.04
Target distance (cm)	6

Optical micrographs of thin films on both substrates are shown in Fig. 3.3. The current collector strips are 5 µm wide and the mesh width accounts to 15 µm. The polycrystalline BZCY (Fig. 3.3a) also exhibits a certain roughness compared to the YSZ single crystal (Fig. 3.3b). A more detailed overview is shown in Subsec. 4.1.2.

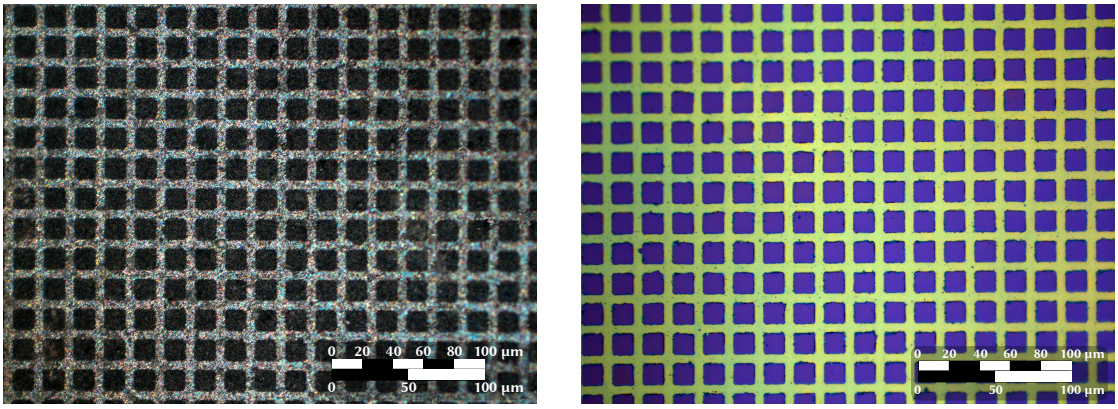

(a) BZCY **(b)** YSZ

Figure 3.3.: Top-views of 200 nm PLD-grown oxide thin films with buried 5/100 nm Ti/Pt (5/15 µm) current collector on both substrates.

3.2.3. Microelectrode Preparation

The general workflow for the microelectrode preparation is shown in Fig. 3.4.

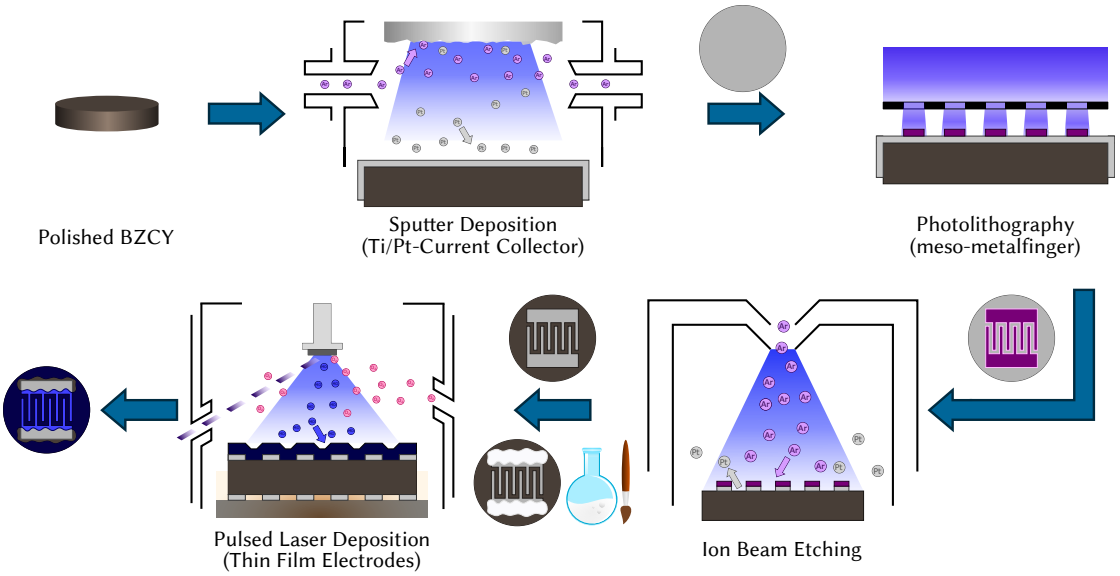

Figure 3.4.: Workflow of the sample preparation for microelectrodes: A dense Ti/Pt-layer is deposited via magnetron sputtering and then microstructured using photolithography. The remaining Ti/Pt-layer was removed using IBE resulting in a interdigitating finger geometry. Thin films are deposited via PLD, after covering the Pt-pads with ZrO_2.

In the first step, a dense Ti/Pt- layer was deposited by means of magnetron sputtering using the parameters shown in Tab. 3.3. Then, an interdigitating finger structure is developed via negative photolithography (see Fig. 3.4). In the next step the remaining Ti/Pt-layer had to be removed. This was achieved via ion beam etching (IBE) using an unfocussed Ar plasma cone. The parameters for this etching step can be found in Tab. 3.5.

In the next step, the desired MIEC thin film was deposited via PLD using the before mentioned parameters (Tab. 3.4). In this case the active electrode area was limited by the geometrically well-defined current collector and the limited electronic conductivity of the used oxides. A micro-structuring of the MIEC film could be omitted owing to the fact that the electrochemically active region is restricted to whole surface area above the current collector plus a narrow zone of several µm around the metallic current collector. In order to be able to directly contact an electrode, the Ti/Pt-pads had to be completely free of electrode material. To achieve this, a slurry of ZrO_2 and terpineol was prepared. The pads were then carefully covered by this

Table 3.5.: IBE parameters used for the removal of the Ti/Pt layer

Parameters: Ion Beam Etching	
Magnetron current (mA)	25
Beam voltage (kV)	2.5
Extractor voltage (kV)	0
Ar pressure (mbar)	7 to 9 × 10^{-5}
Plasma current (mA)	1.2 to 1.4
Etching time (min)	120

paste prior to the PLD process using a brush. After the MIEC deposition the protecting ZrO_2 was removed using compressed air. The back of the sample was prepared using the workflow described in Subsec. 3.2.2.

Optical microscope images of the resulting interdigitating finger geometry are shown in Fig. 3.5. Each of the eight fingers of structure no. 2 has a length of 980 µm and a width of 15 µm. Furthermore, the distance between two fingers amounts to 15 µm. Including the meander length of 7100 µm this results in an electrochemically active area of 0.0022 cm^2. The images also show the uncovered Pt-pads which were used to contact the samples.

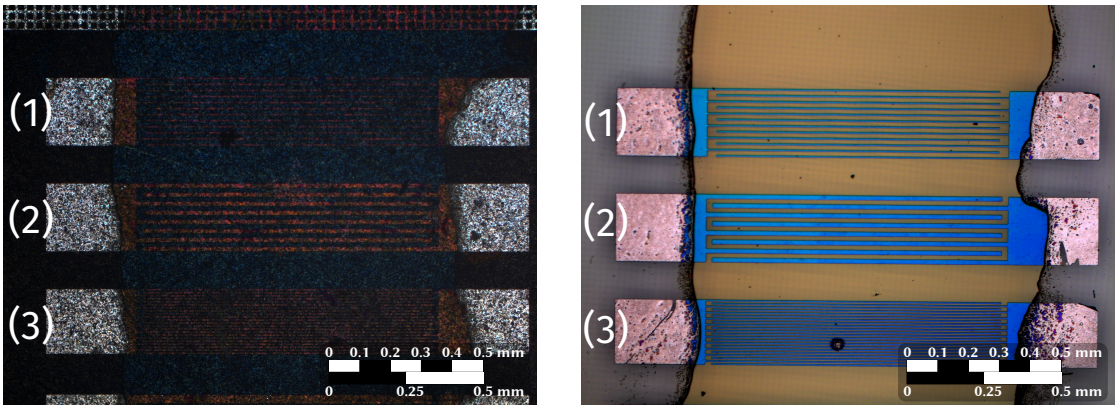

(a) BZCY **(b)** YSZ

Figure 3.5.: Top-views of 200 nm PLD-grown thin films with buried 5/100 nm Ti/Pt (8 interdigitating fingers of 15 µm width, 980 µm length, 15 µm finger distance and 7100 µm meander length).

3.2.4. Samples for Electrochemical Pumping Experiments

In order to analyse the proportion of the current of each conducting species (i.e. its transference number) a setup with two separate gas compartments was used. Due to technical limitation of this setup, the process of the sample preparation had to be further adapted and optimised. The resulting workflow is shown in Fig. 3.6.

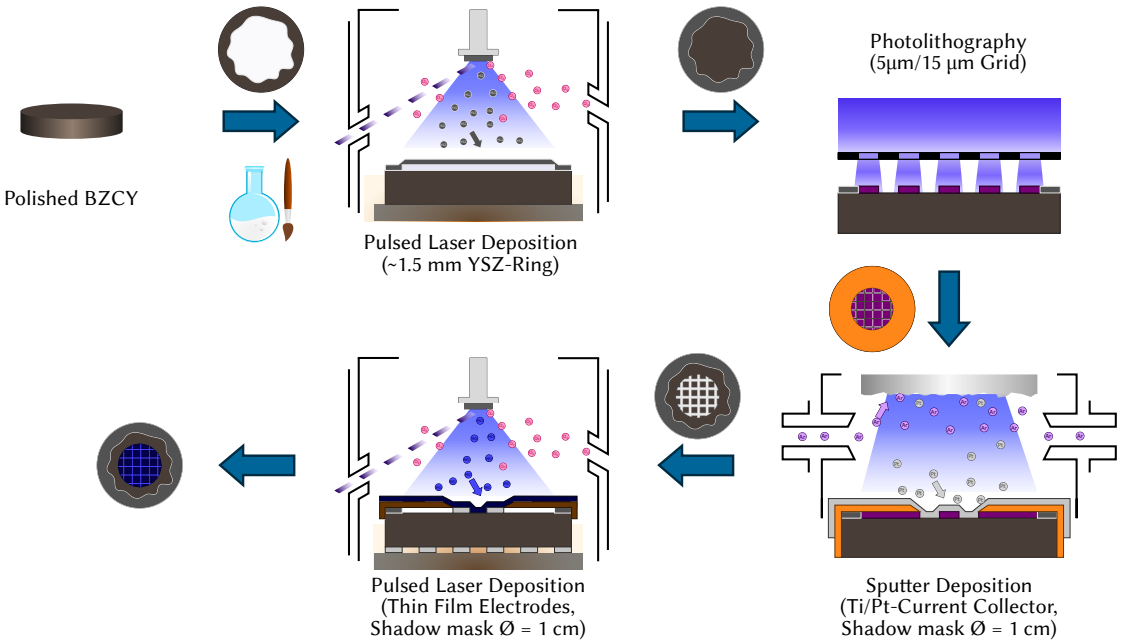

Figure 3.6.: Workflow of the sample preparation for the electrochemical pumping experiments: A YSZ-ring is deposited via PLD. Then a 5/15 µm Pt-grid in a 1 cm circle is deposited via photolithography and magnetron sputtering (using a shadow mask). Similarly, a shadow mask is used during the thin PLD process to prevent the YSZ ring from MIEC film deposition.

In the 2-gas setup a glass seal (glass transition temperature T_{glas} = 525 °C) was used to prevent gas flow of one compartment into the other. However, first tests showed that the BZCY surface is virtually not wetted by the glass. To circumvent this, an outer ring of YSZ was deposited on BZCY via pulsed laser deposition. The standard parameters (see Tab. 3.4) were used with the exception of temperature (450 °C), pulse frequency (10 Hz) and duration (1 h). To prevent coverage of the whole surface area the already mentioned ZrO_2-slurry was used in order to protect the central part of the BZCY disk. Then, the current collector was deposited in the center of the sample using familiar parameters (Tab. 3.2 and Tab. 3.3). To restrict the active surface area to a small circle in the middle of the sample a shadow mask made of acrylonitrile

butadiene styrole (ABS) was put on top of the sample during Ti/Pt deposition. In a similar vein a shadow mask made of corundum was used during the MIEC thin film deposition by PLD using standard parameters (see Tab. 3.4).

3.3. Electrochemical Experiments

3.3.1. Electrolyte Characterisation

The setup for the impedance measurements consists of two parts: an apparatus in which the sample can be mounted, and a tube furnace (Gero, SR 40-200/12). A sketch of the former can be found in Fig. 3.7.

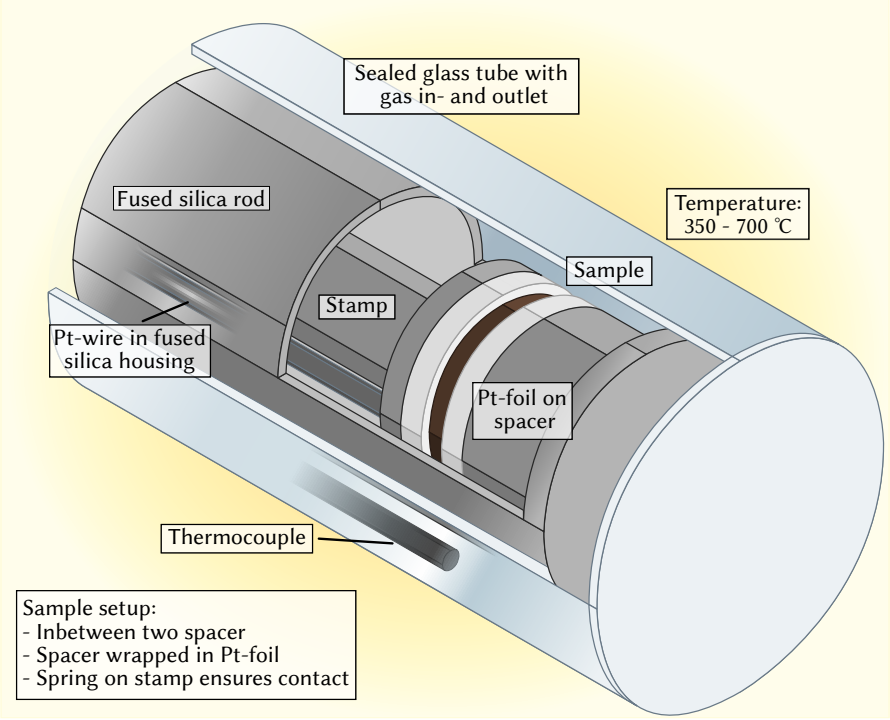

Figure 3.7.: Measurement setup for electrolyte characterisation: Base system consists of a hollow fused silica rod in which the sample is placed between two spacers and held in place via a spring mechanism. Pt-foils on both spacer contact the respective sample electrodes and the thermocouple ensures accurate temperature measurements.

The apparatus includes a hollow rod of fused silica. The sample was generally placed in between two current collectors, which are made of Pt-foil wrapped on a fused silica spacer. A smaller rod with a spring mechanism at one end acted as a stamp and ensured optimal contacting of the sample. A type-S thermocouple in fused silica housing enabled accurate measurement of the current temperature. Pt-wires, connecting the Pt-sheets to electrical feedthroughs, were put in similar housing. This base system of Fig. 3.7 is mounted onto a stainless steel flange (not shown), which also includes gas in- and outlets. Gas tight housing by a quartz glass tub enables control of the desired gas atmosphere. This whole system was then put in a tube furnace to allow uniform heating of the sample.

The Pt-foils on both sides of the samples acted as contacts for the working and counter electrodes. The behaviour of the sample in both, strongly reducing as well as oxidising, regimes was of interest. Therefore, measurements were carried out in pure oxygen and hydrogen (2.5 % H_2/balance Ar, Air liquide) atmospheres. Before entering the apparatus, the gases slowly bubbled through a stainless steel bubbler filled with distilled water at room temperature (22 °C) in order to achieve humidification. Under the assumption of the gas being saturated with water vapour at room temperature, the resulting water partial pressure equals 25 mbar.

In the beginning the measuring apparatus was purged with the desired gas and heated to a temperature of around 700 °C. After achieving equilibrium, impedance spectra were recorded in a frequency range of 900 000 to 0.1 Hz with an AC voltage of 20 mV root-mean-square (*RMS*), using a Alpha-A High Performance Frequency Analyser (Novocontrol). Subsequently, the temperature was lowered by 50 °C and the EIS process repeated until 200 °C was reached. To ensure reproducibility three spectra were recorded at each temperature. Furthermore, a second cycle back to original starting temperature was carried out.

3.3.2. AC Experiments

The symmetrical cell (see Subsec. 3.3.2) was placed in the measurement apparatus shown in Fig. 3.7. The measurements were carried out using the same parameters as described in Subsec. 3.3.1 with the exception of the gas atmosphere and a slightly smaller temperature range of 700 to 300 °C. All further experiments were exclusively performed under a humidified 2.5 % H_2/balance Ar atmosphere.

3.3.3. DC Experiments

The measuring apparatus used in this experiment differs greatly from the one described above. Now, a the microelectrode sample (see Subsec. 3.2.3) was placed on Pt-foil (wrapped around a long fused silica blank as shown in Fig. 3.8), which contacts the counterelectrode. The figure also shows three arms consisting of Pt-wire in a fused silica housing and a sharp needle at the end. Two of those were carefully placed onto the uncovered Pt-pads of the desired microelectrode (working electrode). The third one contacted the Pt-foil and thus the back of the sample (counterelectrode).

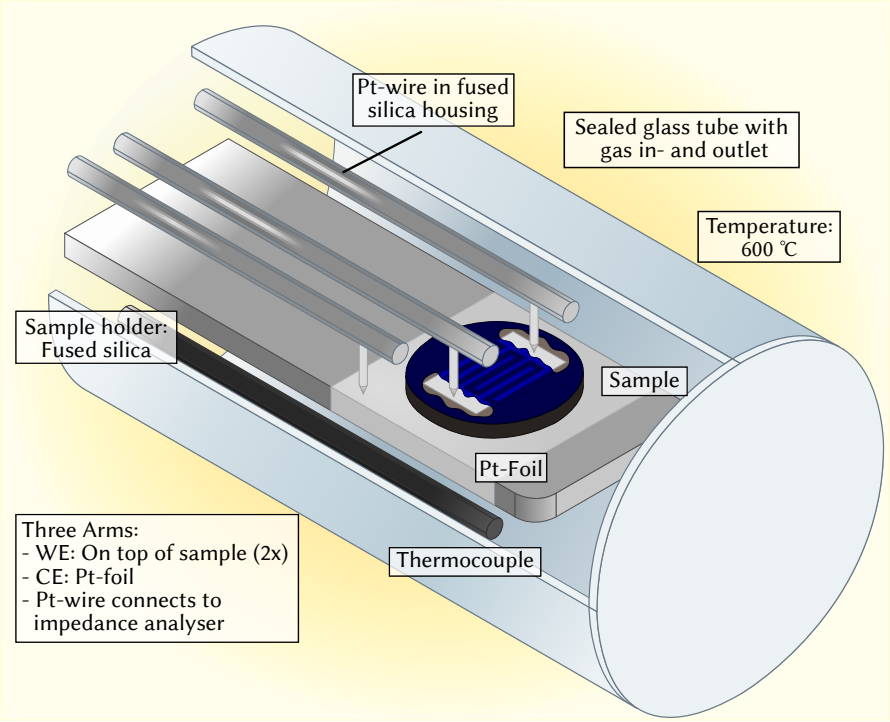

Figure 3.8.: Measurement setup for IV-curve recordings: The sample is placed on a Pt-foil wrapped around a fused silica blank. Two arms with Pt-needles contact the microelectrode and the third one the counterelectrode at the back. The apparatus is kept airtight sealed using the outer glass tube.

Like before, the whole measuring system is mounted onto a stainless steel flange, which also carries the gas in- and outlets as well as the electrical feedthroughs. A thermocouple is placed just beneath the fused silica blank. After contacting and purging with humidified 2.5 % H_2/balance Ar a tube furnace is slowly moved over the apparatus. Then the sample is heated to 600 °C.

After achieving equilibrium, impedance spectra are recorded in the frequency range of 900 000 to 0.1 Hz with an AC voltage of 20 mV *RMS*, just like in the other experiments. The only difference is the applied bias in the range of −100 to 500 mV using 25 mV steps.

3.3.4. Electrochemical Pumping Experiments

The top part of the actual measuring apparatus is shown in Fig. 3.9. It consisted of two hollow corundum pipes. The inner pipe had a diameter of 1 cm and was put on a spring. Pt-wire was wrapped around it in order to contact the electrode of the sample. Its top was put slightly higher than that of the outer pipe including the glass seal. The outer pipe had a diameter of 2 cm. Due to the smaller size of the sample a thick-walled glass seal ring had to be used. The sample was then put on top of the inner pipe. A Pt-contact was placed on top of the sample. Then, the heavy corundum hat was put on the whole structure to fix the sample on the glass sealing and prevent possible shifting of the current collectors.

Both gas compartments had inlets, which were connected to a mass flow controller (MFC) and an exhaust leading to the laboratory hood. Furthermore, the inner compartment exhaust had a split leading to a Pfeiffer OmniStar Gas Analysis System GSD320 containing a QMG220 PrismaPlus Compact Mass Spectrometer (with quartz sample inlet capillary). In addition, both gas flows were humidified. Since the apparatus was built standing upright, the tube furnace had to be rotated 90° and mounted on a custom-made furnace elevator. The temperature was measured using a type-S thermocouple, which was put at sample height.

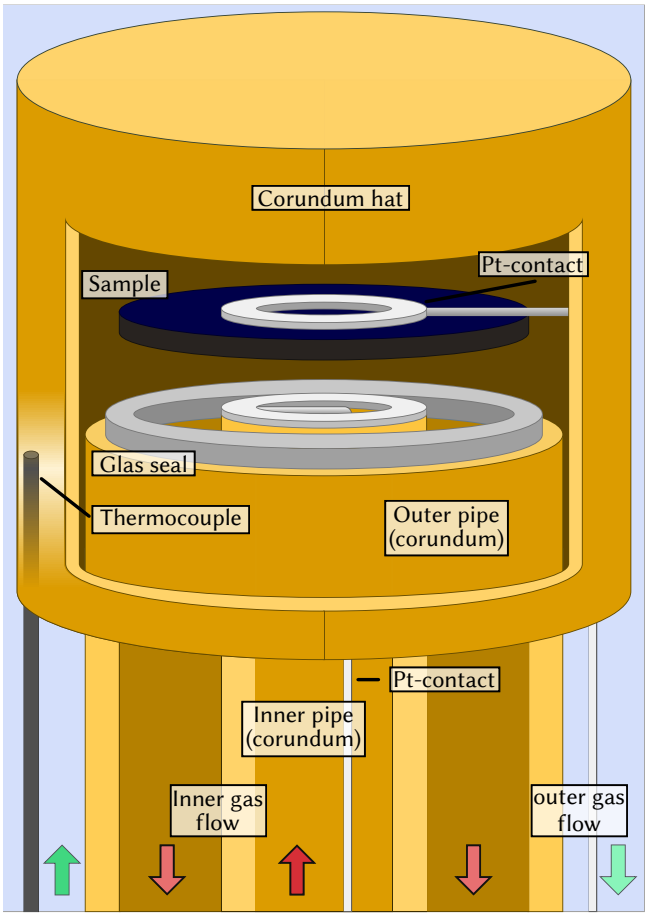

Figure 3.9.: Measurement setup for the 2-gas measurements: The sample is placed on a glass seal on top of the outer pipe. The inner pipe is pressed firmly against the sample with a spring mechanism. Pt-wire is put on the inner pipe and on the outer side to ensure contact with both electrodes. The heavy hat prevents shifting of all components. The inner gas flow takes place in the inner and outer pipe and is also connected to the MS, while the outer gas flow occurs around the hat.

In contrast to the previous experiments, knowledge of the exact gas flow was necessary in order to quantify the measurement results. Thus, the MFCs had to be calibrated. This was achieved by water displacement using the standard N_2-gas. In this setup the amount of time the calibration gas needs to push water through a given volume is measured. Then, the resulting flow rate is calculated. In addition to N_2, Ar was used as a carrier gas. Due to its monoatomic nature, relatively high mass and therefore large difference in heat capacity, a separate calibration had to be carried out. The resulting calibration curves are shown in Fig. 3.10.

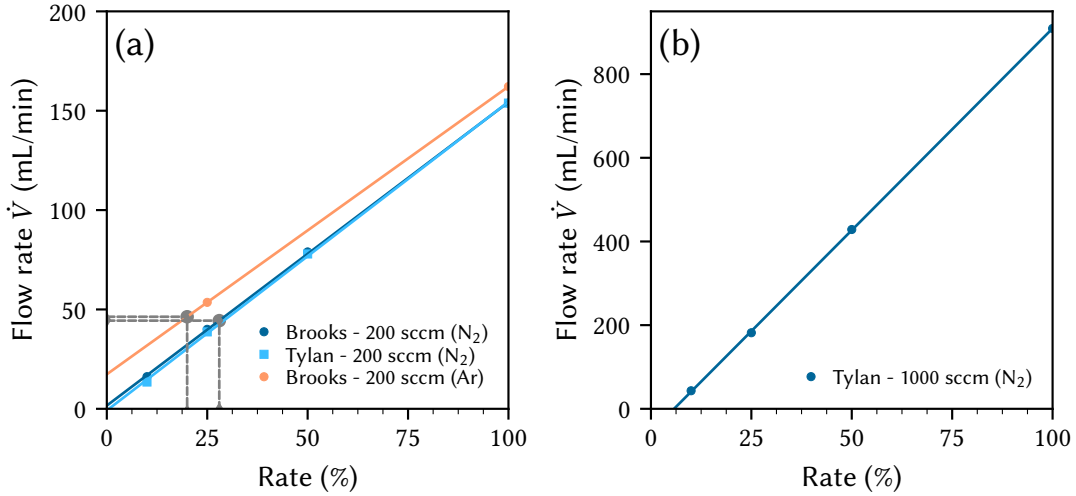

Figure 3.10.: Resulting Calibration curves for (a) Brooks - 200 sccm (N_2, Ar) as well as Tylan - 200 sccm (N_2) and (b) Tylan - 1000 sccm (N_2)

Fig. 3.10a depicts the flow rate $\dot{V}$ in mL min^{-1} by a given rate of 10, 25, 50 and 100 % for both 200 sccm mass flow controller. In Fig. 3.10b the same can be seen for the larger 1000 sccm MFC. In order to achieve a total flow of around 45 mL min^{-1} the needed rate had to be adjusted according to the heat capacity of the gas, as explained above. Rates of 20 % for Ar and 28 % for N_2 result in 46.33 mL min^{-1} and 44.38 mL min^{-1}, respectively.

Partial flows $\dot{V}_{p,i}$ can then be calculated based on the partial pressures of the gases i present in the mixtures according to Eq. (3.1).

$$\dot{V}_{p,i} = \dot{V}_i p_i \tag{3.1}$$

For humidified 2.5 % H_2/balance Ar this results in partial flows of 1.158 and 1.158 mL min^{-1} for H_2 and H_2O, respectively. In the case of 1 % O_2 in N_2 partial flows of 0.144 mL min^{-1} for H_2O and 0.444 mL min^{-1} for O_2.

After purging both compartments with the desired gas the sample was heated to 800 °C. The tightness of the apparatus was determined by observing the MS signal of the interesting mass to charge ratios: 2 (H_2^+), 14 (N_2^{++}, N^+), 18 (H_2O^+) and 32 (O_2^+). Also, the open circuit voltage (*OCV*) was measured at each desired operating temperature. Due to constant fluctuation of

the these values averages of 700 mV, 800 mV and 900 mV at 800 °C, 700 °C and 600 °C were obtained. For positive *OCV*s the negative pole has to be put to the gas compartment with the reducing atmosphere and vice versa for the positive pole.

For drawing electrochemical currents, DC bias was applied using bias steps ranging from 0 to 1400 mV. After each step, the bias was set back to the *OC*V to account for signal fluctuations in the MS. Furthermore, the voltage loss at the electrolyte had to be considered. Thus, impedance spectra at each bias step were recorded in a frequency range of 900 000 to 10 Hz and a AC voltage of 20 mV *RMS*.

4. Results and Discussion

4.1. Target and Sample Characterisation

4.1.1. X-ray Diffraction (XRD)

In order to ensure phase purity diffraction patterns of all prepared targets were recorded. The pellets were objected to X-ray diffraction both before and after sintering to check for significant differences. The resulting patterns for LSBF are shown in Fig. 4.1. It can be seen that the target had various phases before sintering due to the amount of reflexes. Afterwards, only signals of the perovskite-typ lattice can be observed. Any reflexes of the starting materials are either undistinguishable from the noise or not present at all.

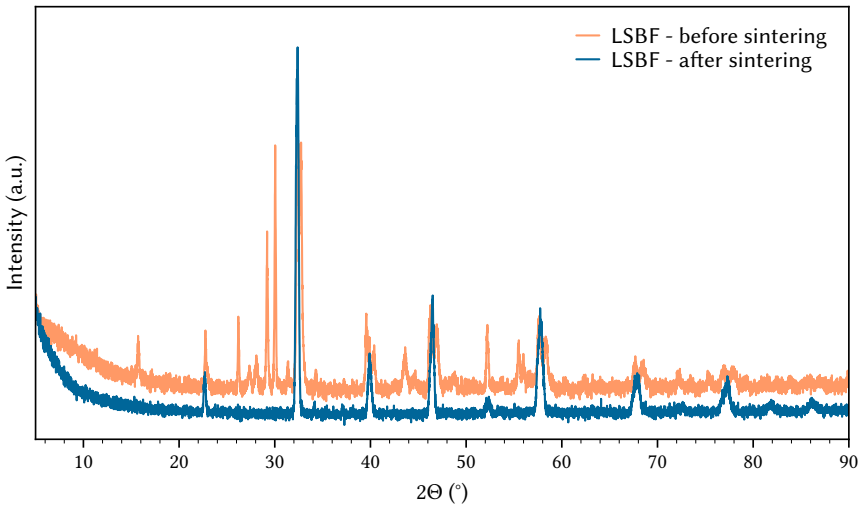

Figure 4.1.: X-ray diffractogram of the LSBF target before and after sintering to verify phase purity

In a similar vein the XRD pattern of BLF is shown in Fig. 4.2. This target was prepared via the Pecchini method. Just like before the necessity of the sintering process can be seen in the stark contrast of the patterns. Compared to the LSBF pattern these one has less noise and seemingly no residual phases left.

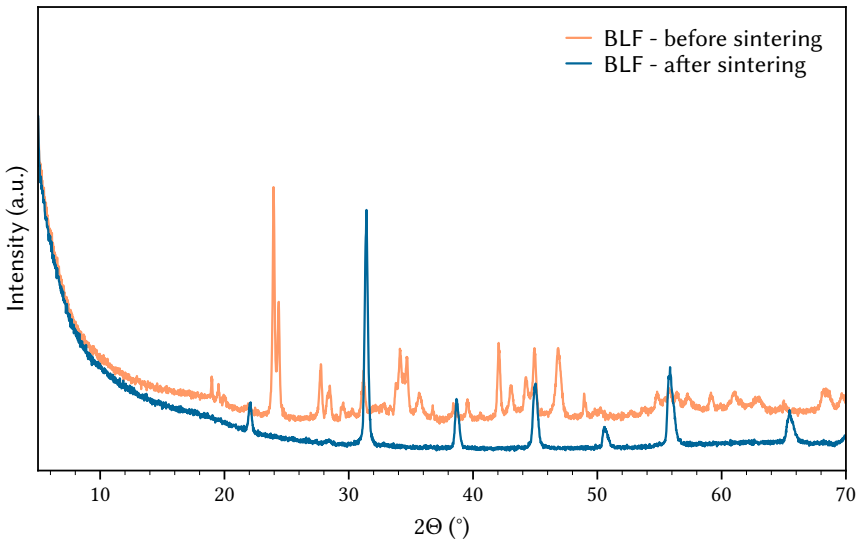

Figure 4.2.: X-ray diffractogram of the BLF target before and after sintering to verify phase purity

4.1.2. Scanning Electron Microscopy (SEM)

Scanning electron microscope images of PLD grown MIEC films were recorded on a FEI TECNAI F20 microscope in order to examine the surface of the thin film samples. Fig. 4.3 shows an overview of a thin film system containing a buried Ti/Pt square grid current collector and a LSBF film on a polycrystalline BZCY substrate after measurement. Even though the substrate was ground and polished before the film depositions a certain roughness can still be observed. Also, in rare cases the prepared current collector via lift-off photolithography shows structural imperfections.

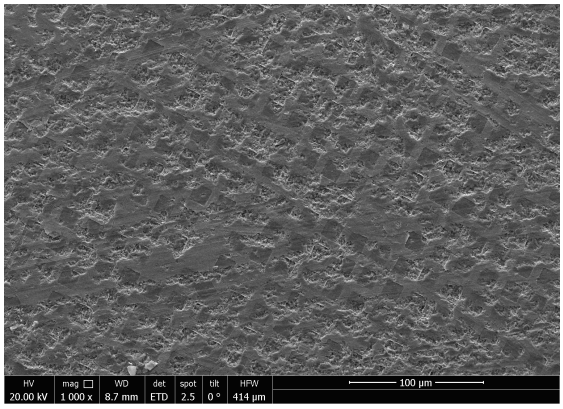

Figure 4.3.: SEM top-views of 200 nm PLD-grown LSBF film with 5/100 nm Ti/Pt (5/15 µm square grid) beneath on a BZCY substrate after heating to 700 °C at 1000 magnification.

Furthermore, there are significant differences in the surface structure of the electrode part deposited on the current collector and the part directly grown on the substrate (see Fig. 4.4). In the first case (Fig. 4.4a) a much more even surface structure can be observed. A film deposited directly on the substrate shows small pores and a larger amount of buckles (Fig. 4.4b).

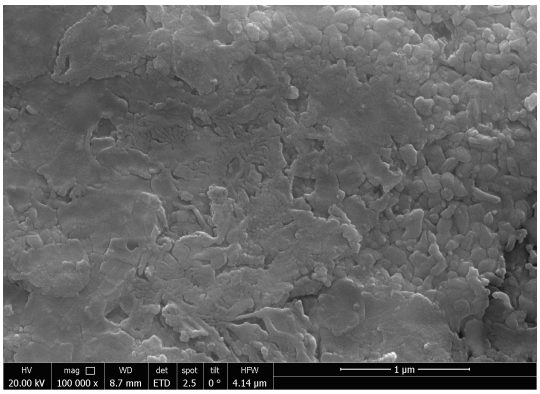

(a) Thin film on current collector

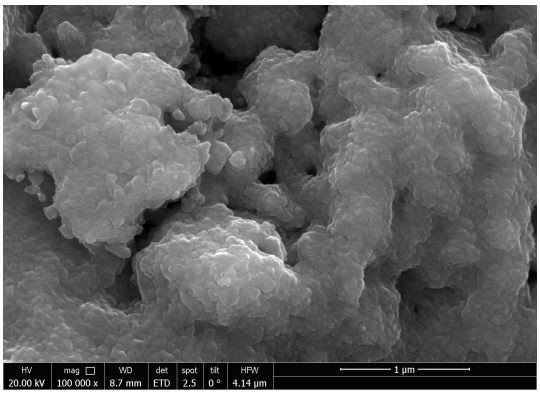

(b) Thin film on substrate

Figure 4.4.: SEM top-views of 200 nm PLD-grown LSBF film with 5/100 nm Ti/Pt (5/15 µm square grid) current collector beneath on BZCY substrate at 10^5 magnification

In Fig. 4.5 the focus is on one specific square of the current collector before and after the measurement. In the first case (Fig. 4.5a) the surface appears to be mostly even. After measurement (Fig. 4.5b) a much higher roughness can be observed, especially on sites with no current collector.

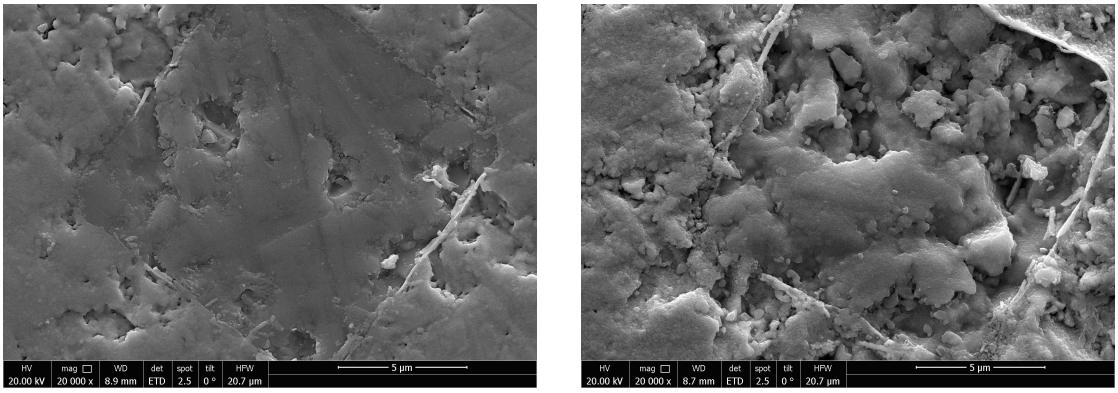

(a) Freshly prepared sample **(b)** Sample after measurement

Figure 4.5.: SEM top-views of a 200 nm PLD-grown LSBF film on a square of a 5/100 nm Ti/Pt current collector BZCY substrate at 20 000 magnification

However, this roughening appears to be not always the case as can bee seen in Fig. 4.6. There, microelectrodes of LSF thin films with the already mentioned current collector on BZCY are shown before and after measurement. Now, the changes of the microelectrode surface structure appear to negliglible before (Fig. 4.6a) and after (Fig. 4.6b) measurement.

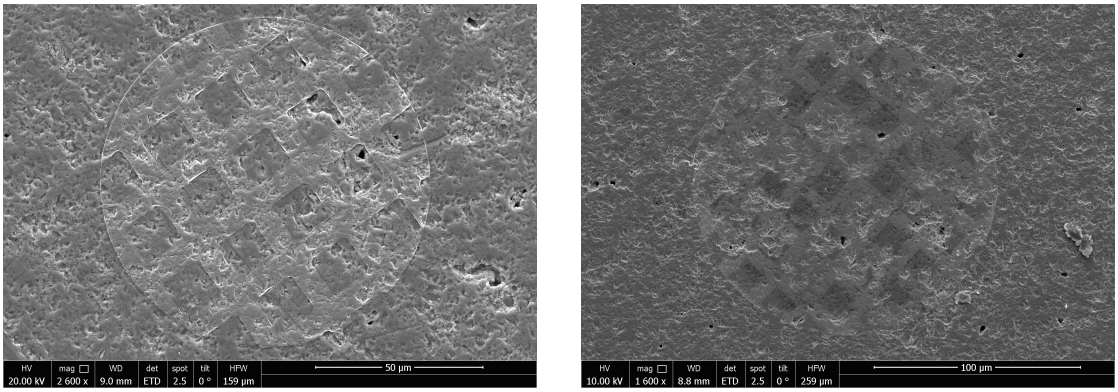

(a) LSF - before measurement **(b)** LSF - after measurement

Figure 4.6.: SEM top-views of a circular 200 nm PLD-grown LSF microelectrode with a 5/100 nm Ti/Pt (5/15 µm square grid) current collector beneath on a BZCY substrate at 1600 and 2600 magnification, respectively.

4.2. Characterisation of Electrolyte Conductivity

Accompanied information of the bought electrolyte pellets only provided insight about the manufacturing process, but no conductivity information was available. Therefore, an electrochemical characterisation was necessary. Experimental data was acquired by impedance spectroscopy measurements in reducing and oxidising atmosphere BZCY samples carrying on porous platinum and Pt|YSZ cermet electrodes at various temperatures.

As described in Subsec. 3.3.1 the complex impedance of the prepared sample was measured as a function of the frequency. Now, the real and imaginary components of the impedance are plotted in the complex plane as parametric functions of the frequency (commonly referred to as Nyquist plot). The resulting spectra in reducing atmosphere for temperatures ranging from 700 to 200 °C are shown in Fig. 4.7.

At high temperatures (700 to 500 °C) the AC measurements show a high frequency x-axis intercept, one depressed arc at intermediate frequencies and a much smaller one at low frequencies (see Fig. 4.7a to Fig. 4.7c). At high frequencies also an inductive feature was observed, caused by the inductance of the cables. For the high temperature cases this high frequency axis-intercept corresponds to the resistance of charge transport in the electrolyte. Barium zirconates are also known to have large grain boundary contributions, especially at smaller grain sizes. Thus, at these high temperatures no clear assignment of the grain or the grain boundary is possible. In this first assumption, both, the medium and low impedance arcs were attributed to processes at the electrode.

At temperatures of 300 °C and lower first indications of a high frequency arc are noticeable (see Fig. 4.7e and Fig. 4.7f). At the lowest temperature of 200 °C enough capacitive information can be obtained to calculate an important material constant: the dielectric constant ϵ_r. In Eq. (4.1) C is the capacitance (around 7.5×10^{-11} F), ϵ_0 the vacuum permittivity (8.854×10^{-12} F m^{-1}), d the thickness and A the area of the sample.

$$\epsilon_r = \frac{C}{\epsilon_0}\frac{d}{A} \tag{4.1}$$

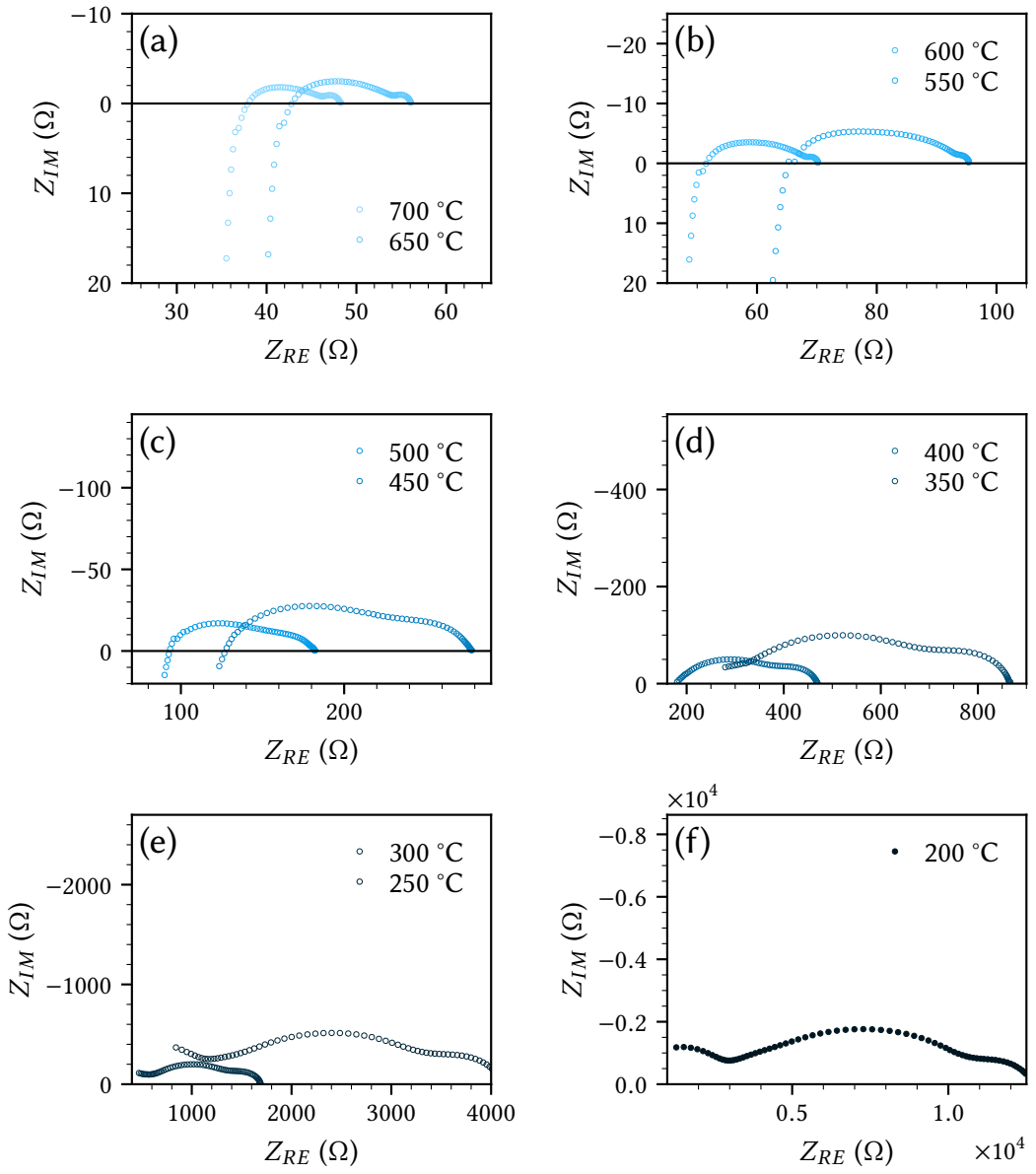

Figure 4.7.: Nyquist plots of BZCY with porous platinum electrodes in reducing atmosphere (2.5 % H_2/2.5 % H_2O) in a temperature range of 700 to 200 °C

Using this equation, average ϵ_r values of around 37.63 ± 0.05 of all spectra recorded at 200 °C are obtained. In literature ϵ_r of around 40 to 46 are reported [48] for bulk values of similar electrolyte compositions. Thus, it appears to be the case that the real axis intercept at higher temperatures corresponds to the bulk resistance, while the grain boundary contribution may in fact be part of the middle arcs. The latter strongly overlaps with the electrode processes and cannot be resolved.

Fig. 4.8 show the obtained Nyquist plots for measurements in oxidising atmosphere with platinum electrodes. At temperatures above 600 °C no reliable data could be obtained due to noise. Just like before, at 400 °C and above the bulk resistance of the electrolyte is given by the intercept of the impedance plane plots with the real axis. In contrast to the spectra recorded at reducing conditions, only a strongly depressed electrode feature intermediate or low frequency can be noticed (see Fig. 4.8a to Fig. 4.8c). At temperatures below 300 °C a small part of an arc at high frequencies appears as well as the beginning of another arc at low frequencies (see Fig. 4.8d to Fig. 4.8f). The dielectric constant obtained via the high frequency arc at 200 °C amounts to 41.40 ± 0.04.

The spectra with Pt|YSZ cermet electrodes show similar features like their platinum counterparts. They can be found in App. A. Fig. A.1 shows the ones measured at low oxygen partial pressures. Like before, at high temperatures (Fig. A.1a to Fig. A.1c) the high frequency real axis intercept was assigned to the bulk resistance of the electrolyte. Compared to Fig. 4.7 features of the electrode are even more convoluted and indiscernible. Only at the lowest temperature (Fig. A.1f) the onset of the electrolyte can be identified.

Fig. A.2 shows the impedance spectra of the cermet measurements at high $p(O_2)$. Above 650 °C the noise prevented obtaining of reliable data. Similar to Fig. A.1 the onset of the electrolyte arc is exclusively shown at very low temperatures (see Fig. A.2e and Fig. A.2f).

Based on the obtained total resistances of the electrolyte R a bulk conductivity σ_{bulk} can be calculated by using the geometrical parameters thickness d and area A of the sample, as shown in Eq. (4.2).

$$\sigma_{bulk} = \frac{1}{R}\frac{d}{A} \tag{4.2}$$

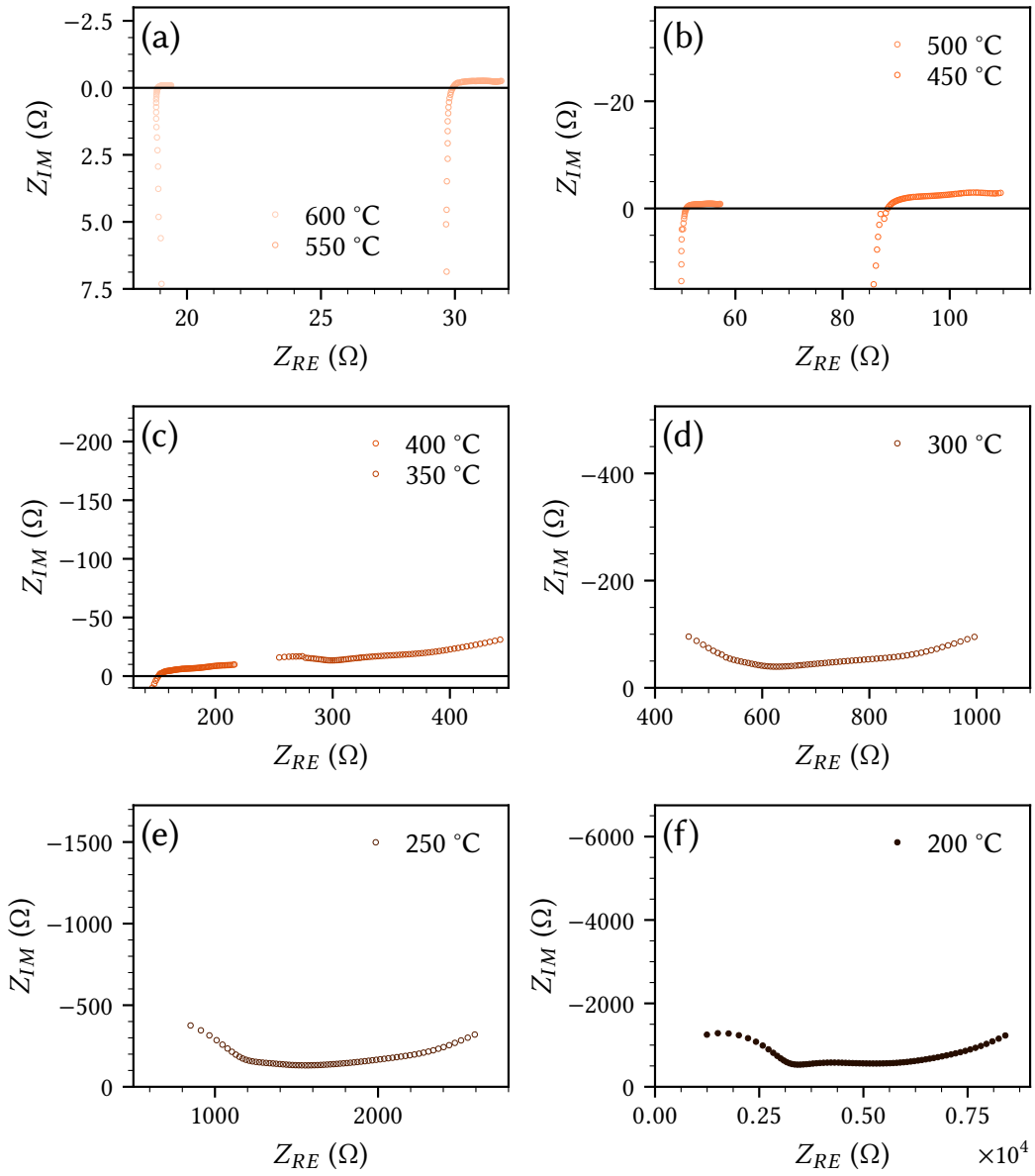

Figure 4.8.: Nyquist plots of BZCY with porous platinum electrodes in oxidising atmosphere (O_2/2.5 % H_2O) in a temperature range of 600 to 200 °C

As described in Subsec. 2.1.2 the temperature dependence of the conductivity is given by Eq. (2.10). Plotting, the obtained conductivity values in an Arrhenius diagram (see Fig. 2.3) allows calculation of the activation energy E_a of the underlying elementary process.

Since multiple charge carriers (protons and holes) are expected in oxidising conditions a simple linear regression was not feasible. Thus, a non linear regression model was established, which incorporates both, electron holes $h^\bullet$ and protons H^+. In Eq. (4.3) $\sigma_{bulk,i}$ denotes the contribution to the bulk conductivity $\sigma bulk$ of either carrier i, $\sigma^0_{bulk,i}$ and E_a, i are the pre-exponential factor and the activation energy for the respective charge carrier.

$$\sigma_{bulk} = \underbrace{\sigma^0_{bulk,h} \exp\left(-\frac{E_{a,h}T}{k_b}\right)}_{\sigma_{bulk,h}} + \underbrace{\sigma^0_{bulk,H} \exp\left(-\frac{E_{a,H}T}{k_b}\right)}_{\sigma_{bulk,H}} \tag{4.3}$$

Fig. 4.9 shows the resulting Arrhenius plots of each measurements as well as literature data [37, 49]. The calculated activation energies are shown in the form of slope markers for each plot. Measurements in oxidising conditions have two slope markers, one for protons and one for electron holes.

While the absolute conductivity values between each measurement slightly varies the activation energy of proton transport remains in the range of 0.37 and 0.4 eV. These values are in excellent agreement with the literature data of 0.4 and 0.35 eV. Variances between literature and experimental data may be explained by different sample preparation routes and thus different contributions of grain boundaries or slightly different electrolyte compositions or, in the case of *Kreuer*, the use of total instead of bulk conductivity. Grain boundary properties in particular are very sensitive to even minor changes.

As alluded before, at high oxygen partial pressures $p(O_2)$ electron holes play an important role according to Eq. (2.17) [50]. Oxygen from the gas atmosphere is incorporated into the lattice by taking up two electrons, thus leaving two electron holes behind. At low $p(O_2)$, in contrast, the hole concentration is sufficiently low to not play an important role. Due to the humid environment proton conduction (see Eq. (2.16)) is thus the predominant charge transport mechanism.

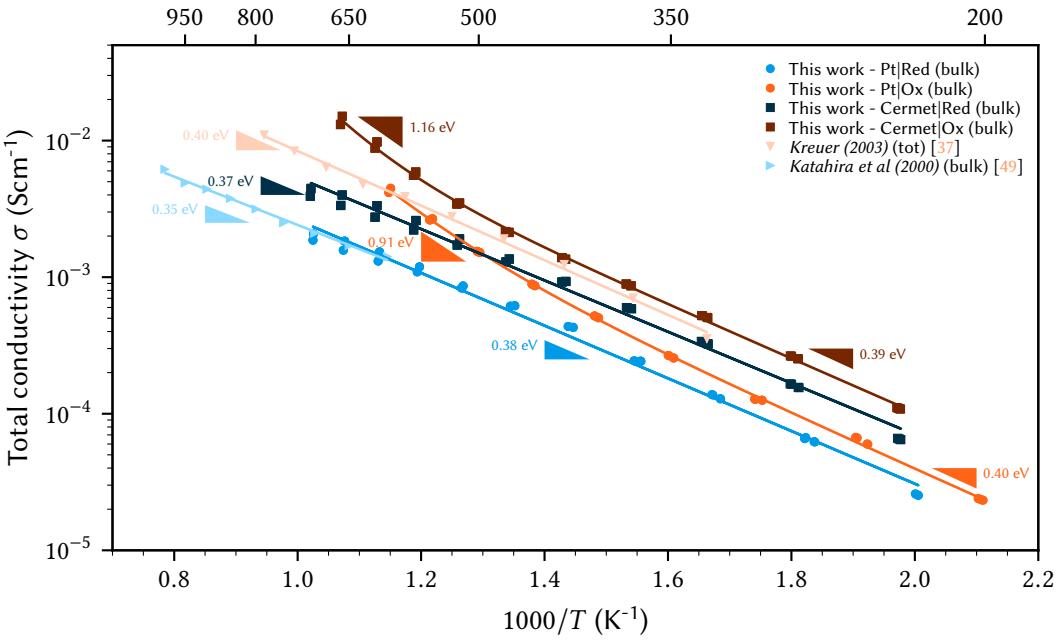

Figure 4.9.: Arrhenius plot of the ionic conductivity of BZCY in humid reducing (2.5 % H_2) and oxidising atmosphere as well as comparison with *Kreuer* ($Ba(Zr_{0.765}Ce_{0.085}Y_{0.15})O_{3-\delta}$, unknown atmosphere) [37] and *Katahira et al* ($Ba(Zr_{0.8}Ce_{0.1}Y_{0.1})O_{3-\delta}$, humid H_2) [49]

The reason for variances in total conductivity of measurements with different electrodes on the same substrate may be associated with poor adhesion of the porous electrodes. In fact, problems at the platinum interface with barium zirconate electrolytes have already been reported in the literature due to weak attachment of the Pt layer to the electrolyte and thermal expansion mismatch [51]. YSZ is proven to work as an adhesion promoter as can bee seen in Subsec. 3.2.4.

Tab. 4.1 gives a summary of all obtained activation energies as well as standard deviations. High values for the latter are due to few data points in electron hole dominant regions (e.g. above 600 °C).

In summary it was shown that the BZCY electrolyte used in this work shows the expected behaviour in comparison to the literature. Activation energies, regarding the proton conduction in particular, are in very good agreement with reported values [37, 49].

Table 4.1.: Comparison of obtained E_a values for all measurements as well as literature data provided by *Kreuer* [37] and *Katahira et al* [49]

Sample	Activation energy E_a (eV)	
	Protons	**Electron Holes**
This work - Pt|Red	0.38 ± 0.02	
This work - Pt|Ox	0.4 ± 0.16	0.91 ± 1.32
This work - Cermet|Red	0.37 ± 0.02	
This work - Cermet|Ox	0.39 ± 0.1	1.16 ± 1.6
Kreuer (2003)	0.4 ± 0.04	
Katahira et al (2000)	0.35 ± 0.05	

4.3. Electrochemical Characterisation of Proton Conducting MIEC Electrodes

In the case of symmetrical cells on BZCY the active electrode area was about 2.5 cm^2. This results in an electrode volume of 5×10^{-5} cm^3 after inclusion of the film thickness. In comparison, the cells constructed on YSZ had 1 cm^2 and 2×10^{-5} cm^3, respectively. As described before, all impedance measurements were conducted in the temperature range of 700 to 300 °C in humidified reducing conditions.

Fig. 4.10 shows the resulting Nyquist plots for LSF electrodes on BZCY. In addition, CNLS fits modelled after a specific equivalent circuit (see Fig. 4.14), are displayed, which will be explained in detail later on. At higher temperatures (Fig. 4.10a) the signal consists of an x-axis offset, a shoulder at middle frequencies (MF) and a larger, depressed semicircle at low frequencies (LF). By lowering the temperature the offset transforms into the ending of a depressed semicircle (see Fig. 4.10d).

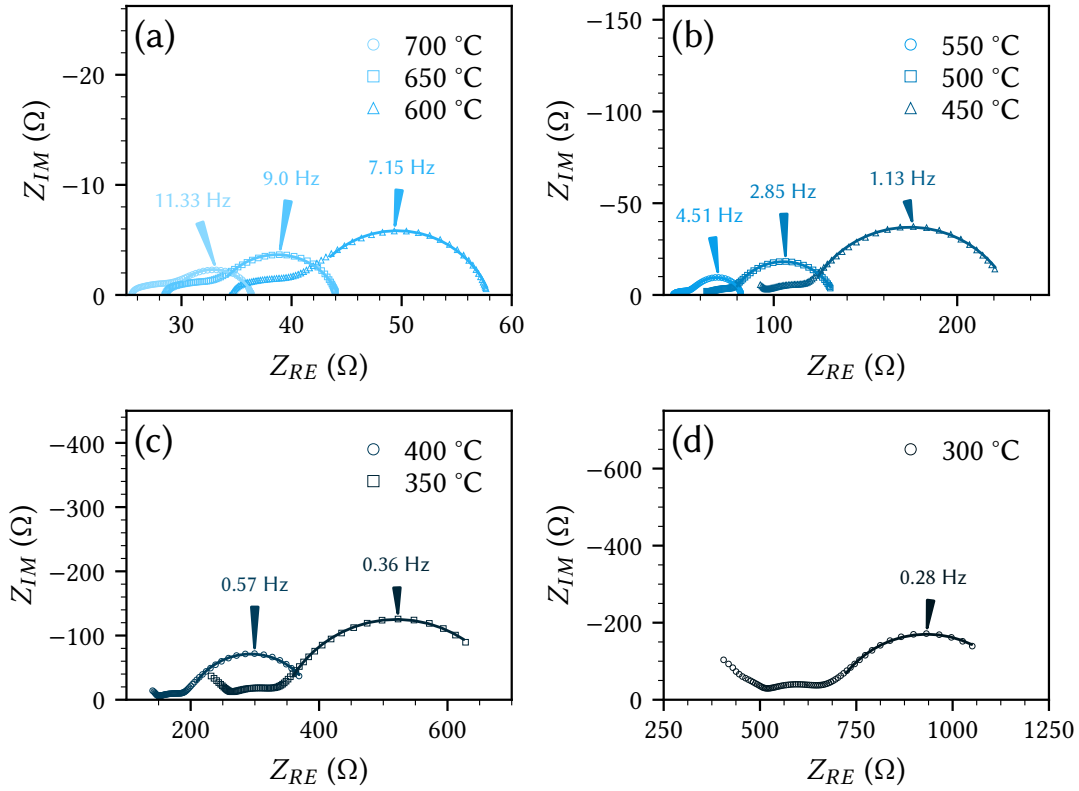

Figure 4.10.: Nyquist plots of a symmetric cell of LSF electrodes on a BZCY electrolyte at 700 to 350 °C as well as fit results using the EC shown in Fig. 4.14

The higher frequency features (axis intercept or semicircle fragment) is again assigned to the bulk resistance of ionic charge transport in the BZCY electrolyte (see also Sec. 4.2). The medium frequency arc then includes the grain boundaries and possibly also contribution from the interface to the electrode, whereas the low frequency arc is attributed to and electrode process, which can not be related to and individual elementary process yet.

Similar results are obtained for LSBF electrodes, as depicted in Fig. 4.11, showing also the dominant electrode semicircle and the electrolyte-related intercept (high T) or the fragment of an electrolyte-semicircle at HF (low T). In contrast to the previous spectra, the small arc at MF seemingly decreases with lower temperatures. Apart from that, there is still the dominant semicircle at LF and the ending of a semicircle at HF (at lower temperatures).

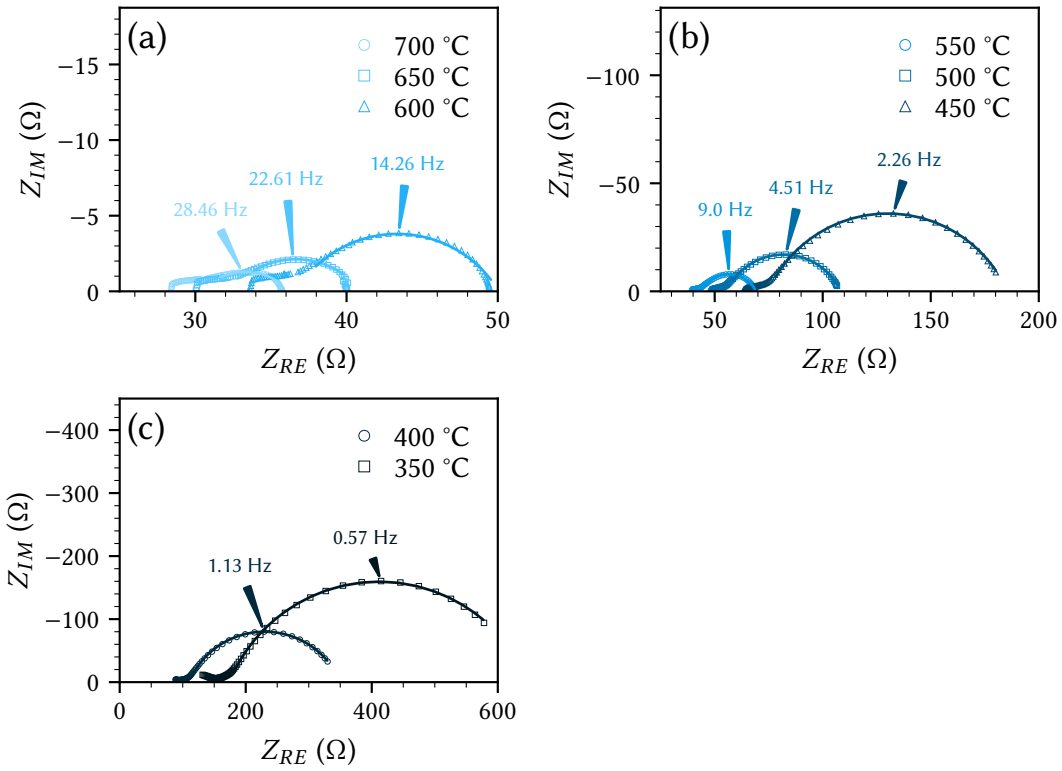

Figure 4.11.: Nyquist plots of a symmetric cell of LSBF electrodes on a BZCY electrolyte at 700 to 350 °C

Nyquist plots of the LSF and LSBF cells on the oxide ion conducting electrolyte YSZ show similar results (Fig. 4.12). The small arc at MF is now hardly visible indicating absence of a grain boundary contribution (only an interfacial resistance between the electrode and the electrolyte remains). By lowering the temperature the HF semicircle becomes the by far most dominant feature. (Fig. 4.12d). This can be explained by relating the arc to the transport resistance of oxide ions in the electrolyte. As explained before, the oxide ion conduction in these ceramics is thermally activated and therefore strongly dependent on temperature.

Using LSBF instead of LSF on YSZ results in almost identical spectra, see Fig. 4.13. The shoulder at MF is slightly more pronounced than before and the semicircle at LF appears more depressed. The angle of around 45° could indicate the contribution of a transmission line type electrode impedance.

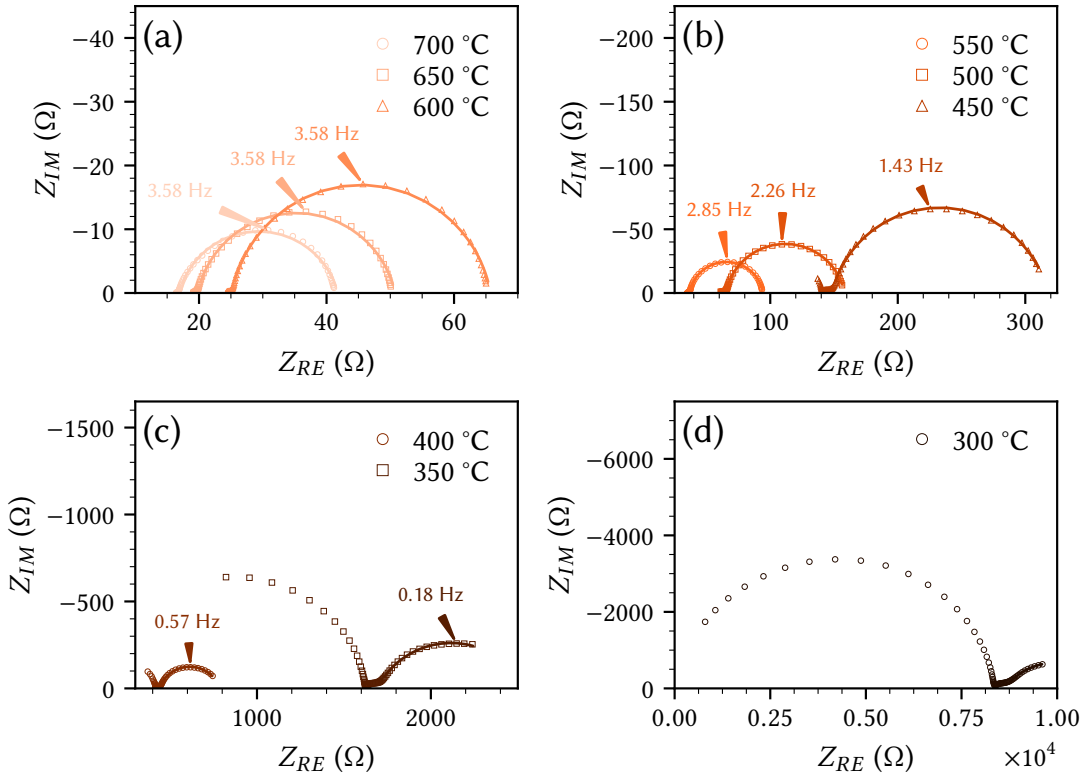

Figure 4.12.: Nyquist plots of a symmetric cell of LSF electrodes on a YSZ electrolyte at 700 to 350 °C

In order to deduce the resistance of the main electrode contribution, the spectra had to be parametrised. This is done by an equivalent circuit. In order to use the same circuit for all measurements a rather simple system of a resistor in series with a R||CPE element was chosen (see Fig. 4.14). To account for inhomogeneity a constant phase element was used instead of an ideal capacitor. Only the low frequency data points are used for the fitting procedure, see fit lines in the figures, e.g. in Fig. 4.10a.

In this model circuit the first resistor R_{offset} includes the resistance to charge transport in the respective electrolyte as well as resistances at the electrolyte-electrode interface or the ion and electron transport in the electrode. The resistor of the R||C element represents the polarisation resistance of the electrode R_{surf}, which - in this case - is most likely surface related. This is concluded from the size of the capacitance (see below), in accordance with *Baumann et al* [52]. The capacitance of this R||C element is then attributed to the so called chemical capacitance

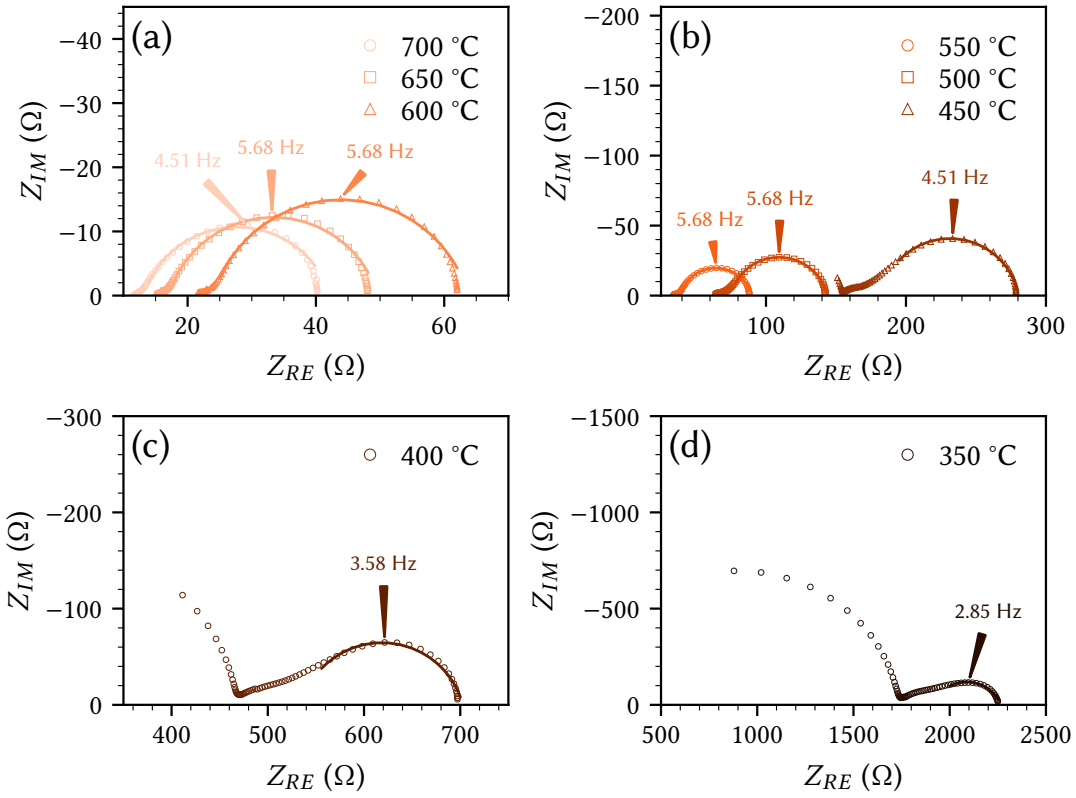

Figure 4.13.: Nyquist plots of a symmetric cell of LSBF electrodes on a YSZ electrolyte at 700 to 350 °C

C_{chem}. It describes the capability of a sample to store chemical energy, i.e., the changes of the component chemical potential μ_i, due to stoichiometry changes [53]. CNLS-fits using this EC are shown in all previously discussed figures.

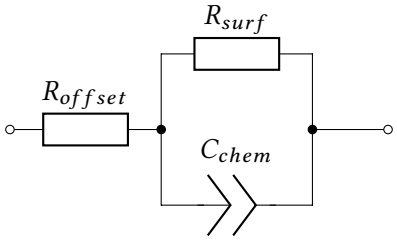

Figure 4.14.: Equivalent circuit used for macro samples in temperature dependent measurements

Chemical capacitance values for electrodes on BZCY can only be estimated using the CPE-element. The area related capacitance is calculated using Eq. (2.25), which results in values of around $10^{-3}\,\mathrm{F\,cm^{-2}}$ for LSF and $10^{-2}\,\mathrm{F\,cm^{-2}}$ for LSBF (see Tab. 4.2). Capacitances in this range are usually chemical capacitances and depend on the specific defect concentrations. Those seem to be affected by Ba replacing some Sr. Owing to this interpretation as a chemical capacitor it is reasonable to assume that the resistance of this semicircle is related to the electrochemical oxidation of hydrogen at the electrode surface. In general, this is a complex, multi-step process, which will be explained in detail later on.

Table 4.2.: Area related chemical capacitances of all combinations at 600 °C

Sample	$C_{chem}A^{-1}$ **(F cm^{-2}) at** 600 °C
LSF|BZCY	2.30E-03
LSBF|BZCY	2.14E-02
LSF|YSZ	1.05E-03
LSBF|YSZ	3.20E-02

The EIS measurements were then used to evaluate the area specific resistance (*ASR*) of the surface resistance of the thin film electrodes. Its definition is shown in Eq. (4.4), where A is the geometrical electrode area. The factor of $\frac{1}{2}$ results from the fact that in the symmetric samples two identical electrodes are connected in series. The latter, in this case, only contains the low frequency semicircle. The small shoulder at intermediate frequencies is, as explained above, attributed to the electrode electrolyte interface and or grain boundaries and thus not included. At 600 °C the *ASR* of all samples was around $15\,\Omega\,\mathrm{cm^2}$.

$$ASR = \left(\frac{R_{pol}A}{2}\right) \tag{4.4}$$

Its temperature dependency was further investigated by plotting the logarithmic *ASR* in an Arrhenius diagram (Fig. 4.15). The total *ASR*-values of all electrode-electrolyte combinations are in the same order magnitude. The resulting activation energies E_a are in the range of 0.4 to 0.7 eV. However, neither electrode nor electrolyte variation resulted in a specific trend. This can be seen as an indicator that the rate determining step (*rds*) causing the surface resistance may be independent from the ionic charge carrier in the cell and thus from the reaction mechanism of H_2 oxidation.

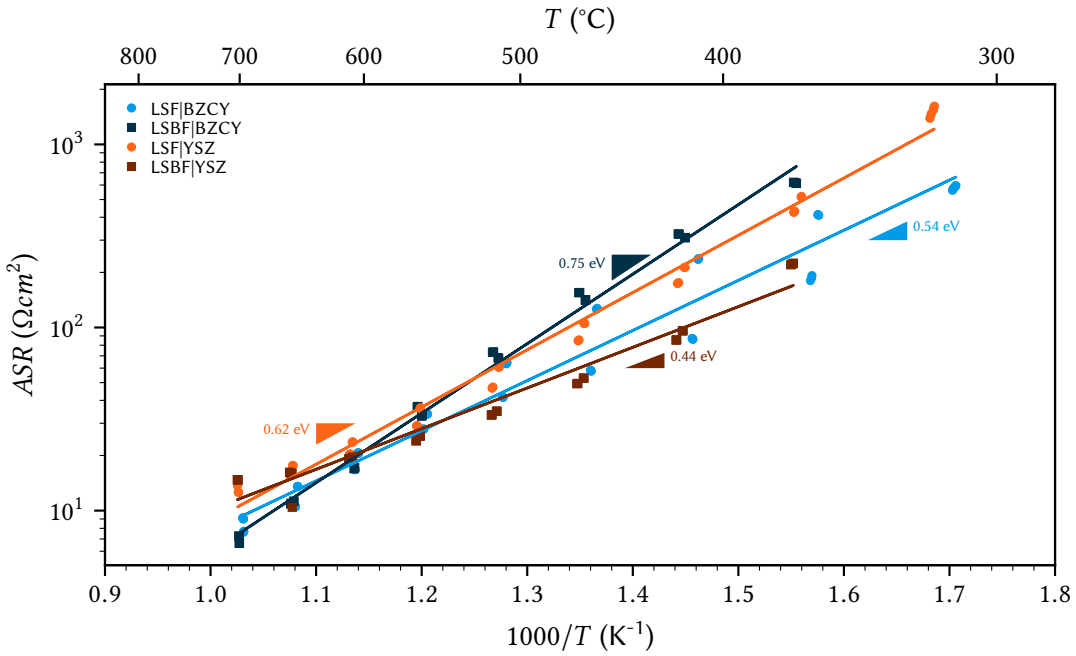

Figure 4.15.: Arrhenius plot showing the temperature dependence of the area related polarisation resistance *ASR* in (2.5 % H_2/2.5 % H_2O) of all previously shown macro samples

4.4. I-V Curves

One of the possible rate limiting steps in the H_2 oxidation process is diffusion of protons through the electrode bulk to the electrode surface. In general, a transport limitation can be tested by applying DC bias to the electrode - a limiting current in the resulting I-V curve would be a strong indicator for this behaviour. So far all measurements were conducted by using alternating voltage only. In this case, the selected reaction is driven back and forth around its equilibrium. Upon DC bias application an additional net reaction rate and therefore a net DC current can be observed. The reaction is no longer probed around the equilibrium, but at certain point on the current-voltage (I-V) curve. To avoid contributions from the counter electrode, the current-voltage curves were recorded on LSF and LSBF microelectrodes versus a macroscopic counterelectrode (preparation, see Subsec. 3.2.3).

The resulting overpotential η at a microelectrode can be obtained from the applied bias U_{DC} between working- and counter electrode by correcting for ohmic losses in the electrolyte ($I_{DC}R_{yte}$), as shown in Eq. (4.5).

$$\eta = U_{DC} - \underbrace{I_{DC} R_{yte}}_{\eta_\Omega} \tag{4.5}$$

In order to obtain the correct electrolyte resistance R_{yte}, EIS spectra were recorded at 600 °C after applying either cathodic or anodic bias in 0.025 V intervals up to 0.5 V. The obtained Nyquist plots are shown in Fig. 4.16. In the case of LSBF a very depressed semicircle at MF to LF can be seen. At HF there is a small shoulder indicating the electrode-electrolyte interface. No real axis intercept is visible.

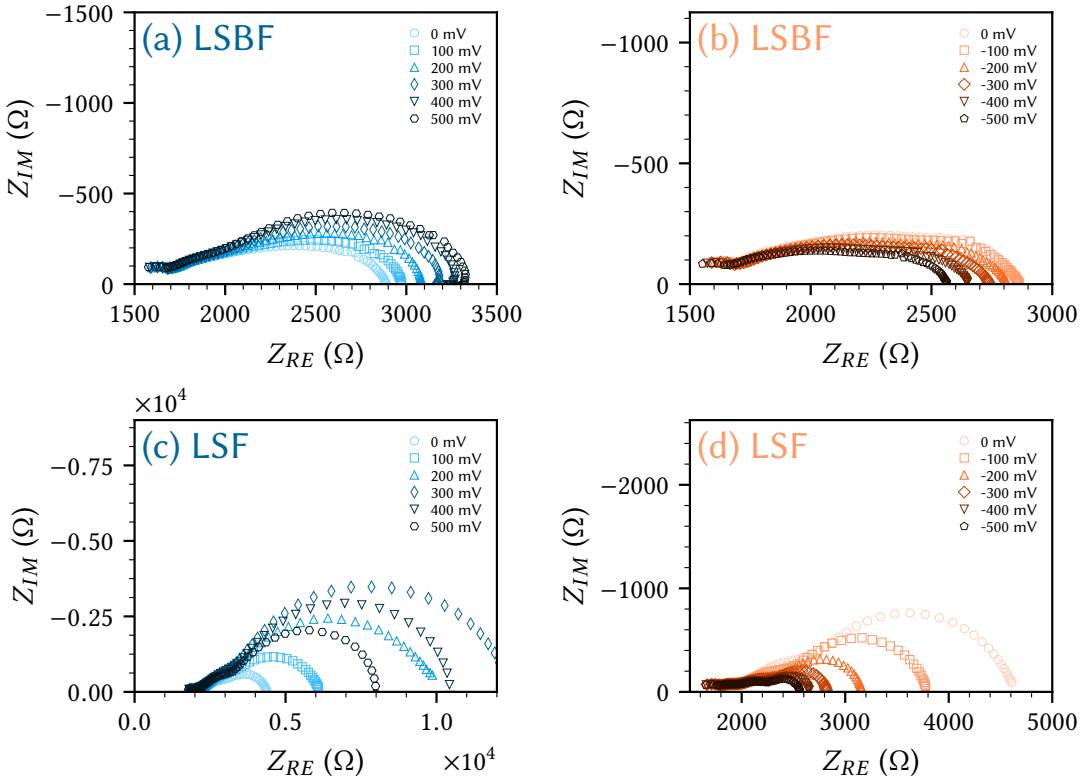

Figure 4.16.: Nyquist plots of LSBF (top) and LSF (bottom) microelectrodes on BZCY electrolytes at 600 °C and applied anodic (left) or cathodic (right) bias ranging from −500 to 500 mV in humid reducing atmosphere (2.5 % H_2)

To obtain R_{yte} all spectra were fitted using the EC shown in Fig. 4.17. This equivalent circuit by *Baumann et al* is derived from the drift-diffusion model and contains various simplifications [52]. In the end this procedure yields an electrolyte resistance R_{yte}, an interface capacitance as well as resistance (C_{int}, R_{int}), the chemical capacitance C_{chem} and the electrode surface resistance R_{surf}. In our specific case C_{int} and R_{int} may also include grain boundary contribution.

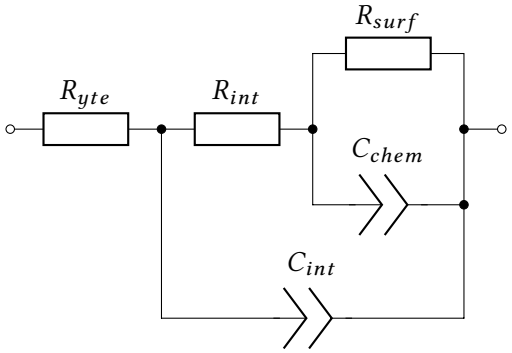

Figure 4.17.: Equivalent circuit used for micro/macro samples in I-V characteristics

For LSBF the real axis intercept is attributed to the ionic transport resistance through the electrolyte, which decreases with anodic bias from 800 down to 500 Ω while obtaining slightly larger values with cathodic bias of around 900 Ω. This behaviour indicates that separation of resistances was not completely successful and other processes such as a contact resistance may also contribute to the HF axis intercept. Also, the simplified circuit model may play a role.

The 'interfacial resistance' R_{int} is 700 Ω at equilibrium and 550 Ω at 500 mV and 1000 Ω at −500 mV, respectively. Anodic bias increases the area specific surface resistance (appearing at LF) from 1 Ω cm^2 at equilibrium to 3 Ω cm^2 at 500 mV. In contrast, cathodic bias has the opposite effect by showing a decrease down to 0.5 Ω cm^2. Reasons for the much lower polarisation resistance compared to Fig. 4.15 are not known.

LSF microelectrodes on the other hand show a semicircle at LF and a more pronounced shoulder at MF. The offset attributed to the electrolyte is mostly constant at around 1900 Ω over the course of the measurement. Only at strong cathodic bias a slight decrease down to 1750 Ω can be observed. The R_{int} increases with anodic bias from 700 up to 2000 Ω and while it remains mostly constant with cathodic bias. In contrast, the surface resistance shows a large decrease for increasing bias voltages. The area specific surface resistance changes from 4 to 0.4 Ω cm^2 at maximum bias. Anodic bias, on the contrary, shows a raise in resistance up to

300 mV followed by decreases at the highest voltages. In this case the area specific surface resistance reached values up to 25 Ω cm^2. Similarly, the interface region at MF becomes more pronounced as more anodic bias is applied.

Due to the large variances in R_{yte}, comparisons with a circular microelectrode of 600 µm were drawn, which has roughly the same amount of active area as the interdigitating finger geometry used in this experiment. The resistance due to ion transport is then given by Eq. (4.6), where d_{ME} is the diameter of the microelectrode and σ_{ion} the conductivity of the ion. The latter was obtained via the results in Sec. 4.2. The resulting 6000 Ω is around three (LSF) to six (LSBF) times larger than in this experiment.

$$R_{yte} = \frac{1}{2d_{ME}\sigma_{ion}} \tag{4.6}$$

After accounting for ohmic losses, as described above, I-V curves are obtained, which are shown in Fig. 4.18 for two microelectrodes each.

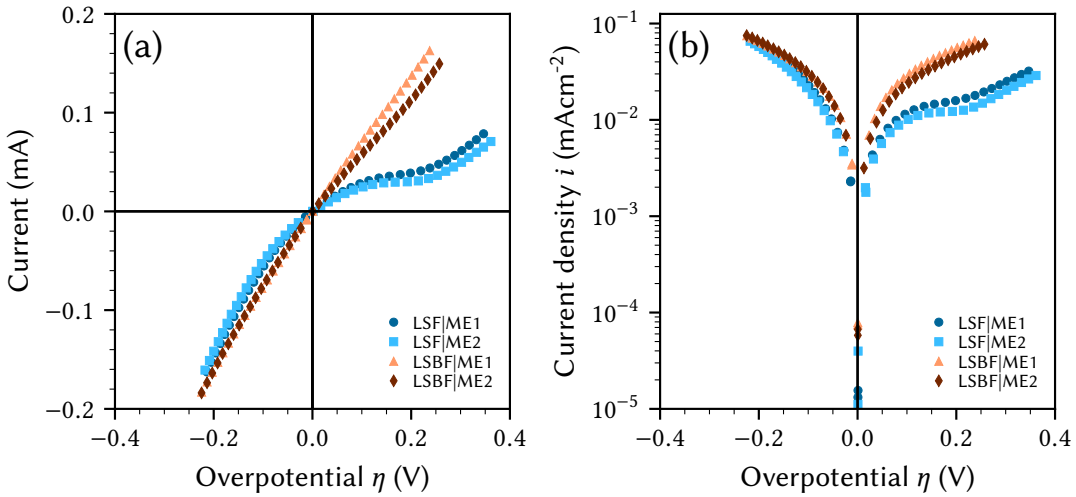

Figure 4.18.: (a) I-V curves and (b) Tafel plots of LSBF and LSF microelectrodes on BZCY electrolytes at 600 °C in (2.5 % H_2 / 2.5 % H_2O)

In the vicinity of the equilbrium (±50 mV) the slopes of both electrode materials are comparable. Moreover, at least for LSBF, no limiting current is present. Thus, it is concluded that close to equilibrium any kind of diffusion limitation, such as gas diffusion or transport of H^+

through the electrode, is not the *rds* of the hydrogen oxidation reaction, especially on LSBF. On LSF, the situation is much more complex - maybe with a change of the mechanism at higher anodic overpotentials - and a straightforward interpretation of the I-V curves for this material is not possible from the available data so far. In conjunction with the previous impedance experiments these results mainly suggest surface processes like the adsorption and dissociation of H_2 or dissociative adsorption of H_2 as possible *rds*.

4.5. Electrochemical Pumping Experiments

4.5.1. Expected Reactions

Since one major goal of this thesis is to relate the reaction mechanism of H_2 oxidation on pervoskite-type MIEC electrodes to the involved ionic charge carrier, measurements of the transference numbers of protons and oxide ions in the BZCY electrolyte were conducted. These measurements were realised by electrochemical pumping experiments and detection of the amounts of H^+ and O^{2-} that can be released as H_2, O_2 or H_2O at the electrodes of a cell with two separate compartments. For comparison, the same experiments were also conducted on cells with YSZ electrolytes. The overview of all expected reactions is shown in Fig. 4.19.

Fig. 4.19 shows an idealisation assuming either a pure proton conducting (yellow) or an oxide ion conducting (green) electrolyte. Furthermore, the cells can operate in two different modes: SOFC and SOEC (indicated by blue and orange arrows, respectively). The former describes an electrochemical cell, where O_2 and H_2 react to H_2O. Thus, a current can be drawn from the cell. By applying a voltage larger than the open-circuit voltage (U_{OCV}) the reverse occurs: water is split into H_2 and O_2.

In terms of half-cell reactions, a pure proton conductor would form H_2O only at the air electrode during SOFC mode and split it again in SOEC mode. On the fuel electrode H_2 is either oxidised (SOFC) and forming protons, which move through the lattice or H_2 is formed via the reverse reaction (SOEC). The corresponding reactions are shown in Eq. (4.7) and Eq. (4.8)

$$2\,H_2 \underset{\text{SOEC}}{\overset{\text{SOFC}}{\rightleftharpoons}} 4\,H^+ + {}_4e^- \tag{4.7}$$

$$4\,H^+ + O_2 + 4\,e^- \underset{\text{SOEC}}{\overset{\text{SOFC}}{\rightleftharpoons}} 2\,H_2O \tag{4.8}$$

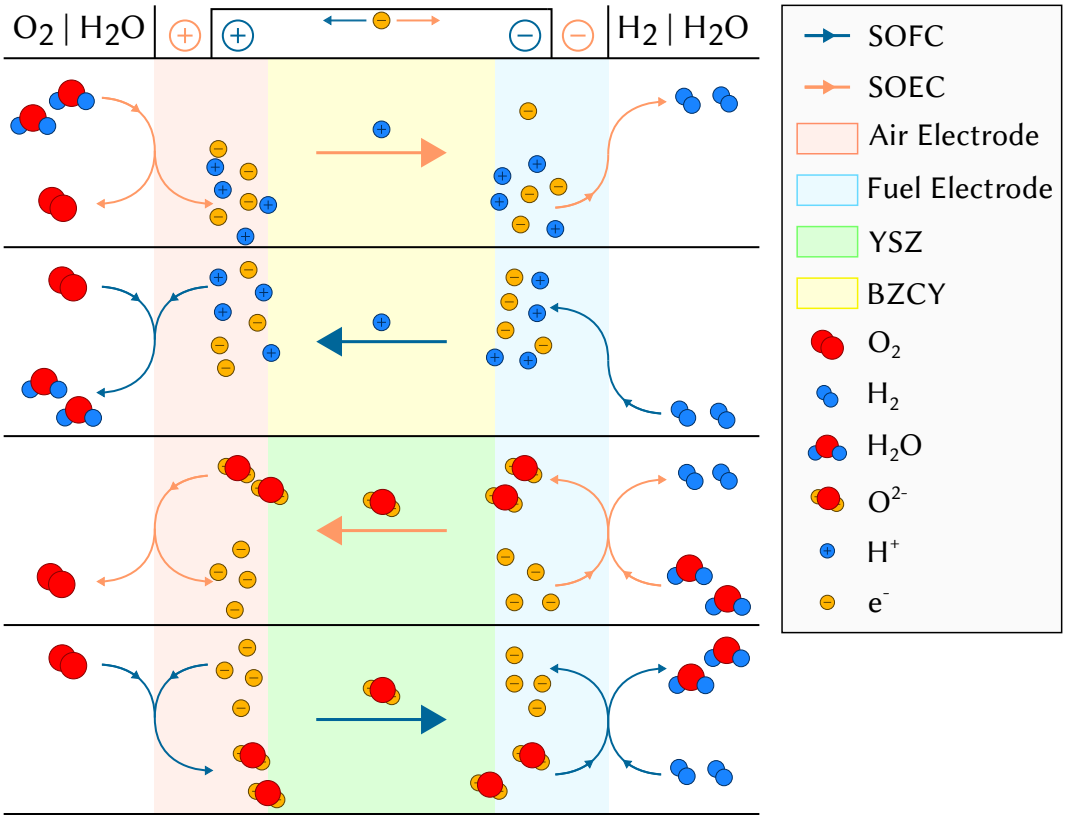

Figure 4.19.: Overview over all expected reactions, where blue arrows indicate SOFC and orange arrows SOEC mode.

For an oxide ion conductor, on the other hand, water is exclusively formed (SOFC) or consumed (SOEC) at the hydrogen electrode (see Eq. (4.9)). During SOFC mode at the air electrode oxygen molecules are reduced to oxide ions, which then move through the electrolyte. In the reverse reaction, O_2 is formed consuming 4 electrons (see Eq. (4.10)).

$$2\,H_2 + 2\,O^{2-} \underset{\text{SOEC}}{\overset{\text{SOFC}}{\rightleftharpoons}} 2\,H_2O + 4\,e^- \tag{4.9}$$

$$O_2 + 4\,e^- \underset{\text{SOEC}}{\overset{\text{SOFC}}{\rightleftharpoons}} 2\,O^{2-} \tag{4.10}$$

In addition to the expected reactions in Fig. 4.19, Fig. 4.20 shows sketched reaction rates of all involved species in their respective compartments on either a pure proton or a pure oxide ion conductor. For the sake of simplicity, exponential reaction rates are assumed.

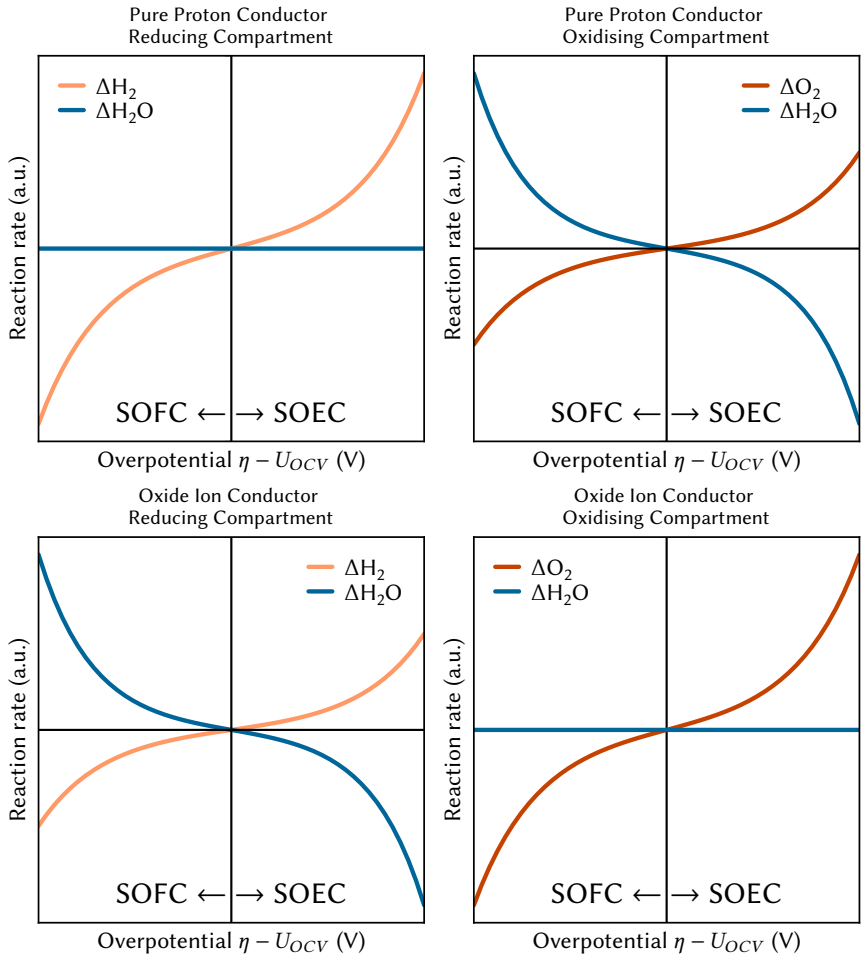

Figure 4.20.: Schematic conversion rates for species of interest for samples with a proton or oxide ion conducting electrolyte in either compartment.

On a pure proton conductor, one notices that H_2O is expected to not be converted in the reducing compartment. H_2 however, is either oxidised and the resulting protons incorporated into the lattice (SOFC) or it is the product of water splitting (SOEC). In the oxidising compartment both, O_2 and H_2O are converted. On an oxide ion conducting electrolyte a change in H_2O content is only observed in the reducing compartment. Therefore, under the assumption of a proton and oxide ion conducting electrolyte, the conversion of H_2O in a specific compartment is unambiguously linked to a specific ionic charge carrier.

The U_{OCV} was only determined experimentally. In order to gauge the expected value using theoretical data, U_{OCV}^{theo} was calculated via the Nernst equation, as shown in Eq. (4.11). There, R is the ideal gas constant ($8.314\,\mathrm{J\,mol^{-1}\,K^{-1}}$), T the temperature, z the amount of electrons exchanged, F Faraday's constant ($96\,485\,\mathrm{C\,mol^{-1}}$) and p_i the partial pressure of the involved species i.

$$U_{OCV}^{theo} = U_{OCV}^{theo,0} + \frac{RT}{zF} \ln\left(\frac{p_{\mathrm{H_2O}}^2}{p_{\mathrm{H_2}}^2 p_{\mathrm{O_2}}}\right) \tag{4.11}$$

The standard potential $U_{OCV}^{theo,0}$ is temperature dependent and can be calculated using Eq. (4.12), where the Gibb's free reaction enthalpy $\Delta_R G^0$ is given by the enthalpy $\Delta_R H^0$ and the reaction entropy $\Delta_R S^0$.

$$U_{OCV}^{theo,0} = -\frac{\Delta_R G^0}{zF} \quad \text{where} \quad \Delta_R G^0 = \Delta_R H^0 - T\Delta_R S^0 \tag{4.12}$$

Using these relations U_{OCV}^{theo} values of 792 mV, 839 mV and 885 mV are obtained for temperatures of 800 °C, 700 °C and 600 °C, respectively. This results in deviations of around 100 (at 800 °C) to 15 mV (at 600 °C) compared to the actual values used in the experiment (refer to Subsec. 3.3.4 for details). A reason for this may be the rising importance of hole conduction at higher temperatures.

In the following, the transference numbers t of each ionic charge carrier were calculated via the molar flows of the involved gaseous species s in their specific compartment l. The different molar flows can then be put in relation according to their half-cell reactions (see Eq. (4.7) to Eq. (4.10)). This yields, for example, Eq. (4.13), where the desired internal molar flow of H^+, $\dot{n}_{\mathrm{H^+}}^{int}$, is unambiguously given via the reaction rate of H_2O in the oxidising compartment ($\Delta\dot{n}_{\mathrm{H_2O}}^{ox}$). The latter is defined by the difference between the incoming and outgoing molar flow (see Subsec. 4.5.4 for details). Also, its relation to the reaction rate of H_2 ($\Delta\dot{n}_{\mathrm{H_2}}$) and O_2 ($\Delta\dot{n}_{\mathrm{O_2}}$) in the reducing and oxidising compartment, respectively, is shown.

$$\Delta\dot{n}_{\mathrm{H_2O}}^{ox} = \frac{1}{2}\dot{n}_{\mathrm{H^+}}^{int} = 2\Delta\dot{n}_{\mathrm{O_2}} = \Delta\dot{n}_{\mathrm{H_2}} \tag{4.13}$$

Similarly, the internal molar flow of O^{2-} is explicitly given by the reaction rate of H_2O in the reducing compartment, as shown in Eq. (4.14).

$$\Delta\dot{n}_{H_2O}^{red} = \dot{n}_{O^{2-}}^{int} = 2\Delta\dot{n}_{O_2} = \Delta\dot{n}_{H_2} \tag{4.14}$$

Furthermore, the ratio of H_2 to O_2 is set to 1:2 by the stoichiometry of the total reaction (Eq. (4.7) to Eq. (4.10)). All explanations above describe cells with either an exclusively proton or oxide ion conducting electrolyte. However, it is possible that proton conducting electrolytes like barium zirconates also exhibit a small amount of oxide ion conductivity. Thus, transference numbers of each charge carrier are of interest.

4.5.2. Proton Conductor

In order to obtain the reaction rates mentioned before, measurements were carried out using symmetric cells LSF, LSBF and BLF electrodes on BZCY electrolytes. Please note that the symmetric cell was exposed to an asymmetric gas environment, one reducing the other oxidising. Due to the separate compartments of the measuring apparatus the evolution of a specific species over time was possible using mass spectrometry. To account for drifts in the signal, open-circuit voltages were recorded at each respective temperature and then used as a reference point.

Fig. 4.21 shows the conversion of H_2 and H_2O via their m/z-ratios in the reducing compartment of a symmetric cell using LSF electrodes and a BZCY electrolyte for voltages from 0 to 1400 mV at temperatures ranging from 800 to 600 °C. 0 V corresponds to a short circuited cell, $U < U_{OCV}$ indicates operation in fuel cell mode and $U > U_{OCV}$ corresponds to electrolysis. In the following figures the difference $U - U_{OCV}$ is used and negative values thus indicate fuel cell mode while positive voltages represent water splitting. The areas of different temperatures are coloured accordingly.

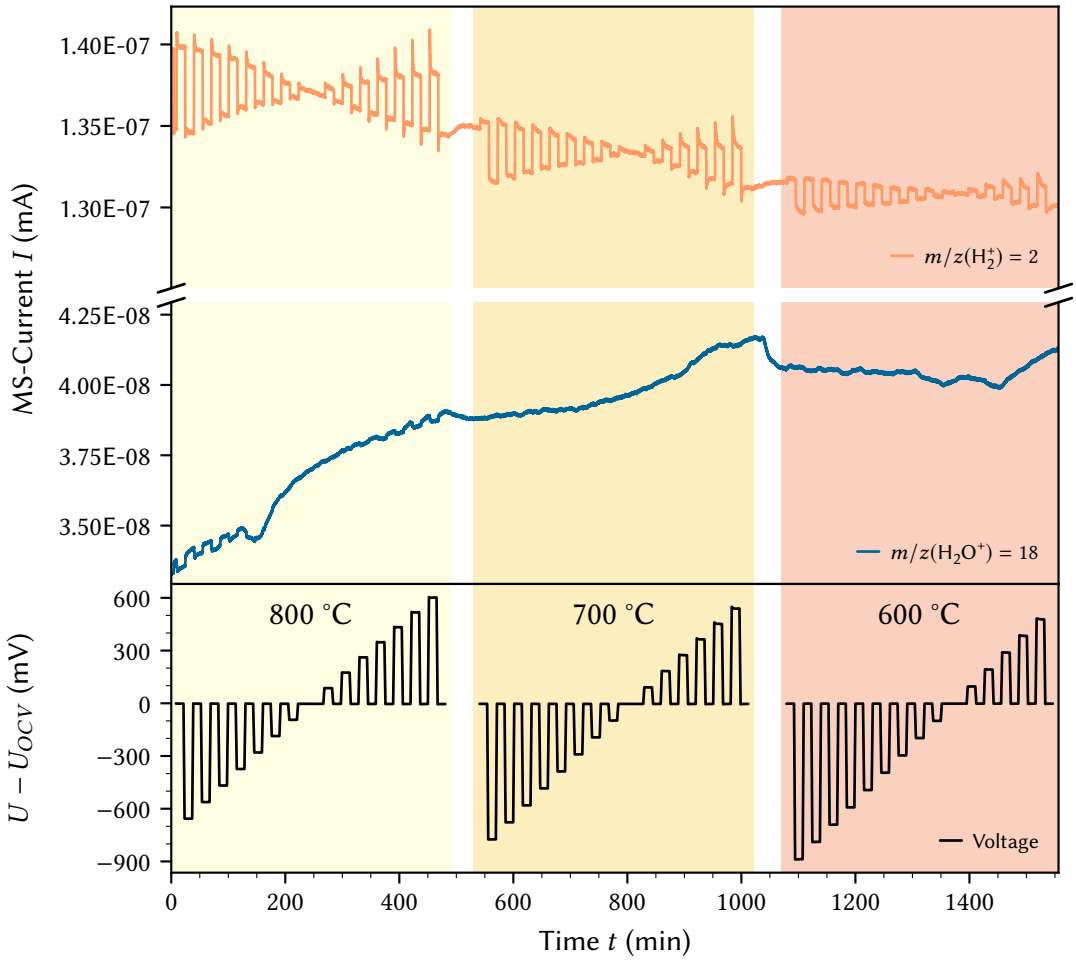

Figure 4.21.: Conversion of H_2 and H_2O over time in the reducing compartment of a cell using LSF electrodes and a BZCY electrolyte for voltages from 0 to 1400 mV at temperatures ranging from 800 to 600 °C.

For easier interpretation the evolution of H_2 at 800 °C is again separately depicted in Fig. 4.22. In the bottom part the applied cell voltage U is shown relative to the measured U_{OCV}. Dashed lines show the change in signal at certain voltages. The large spikes at the beginning and end of each step may be the result of charging and discharging a (chemical) capacitance. U smaller than U_{OCV} results in H_2 consumption (SOFC), while H_2 is produced if U_{Bias} is larger than U_{OCV}. For H_2 the bias steps are visible at all temperatures, while for H_2O a noticeable formation or consumption was only observed at the highest temperatures.

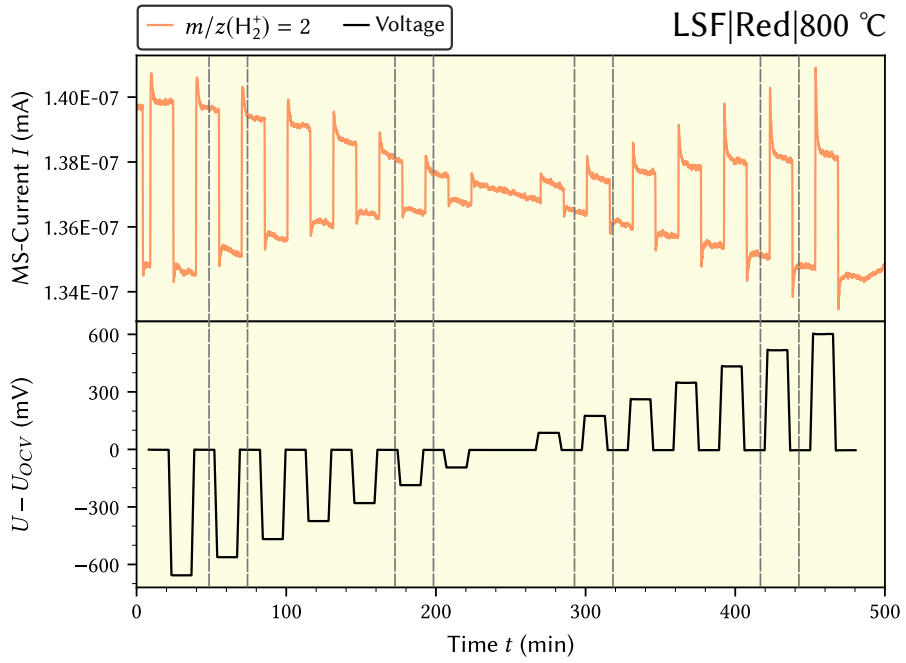

Figure 4.22.: Example of H_2-evolution and -consumption over time in the reducing compartment of a cell using LSF electrodes and a BZCY electrolyte during for voltages from 0 to 1400 mV at a temperature of 800 °C.

In the next step, the evolution of O_2 and H_2O in the oxidising compartment was followed by repeating the same procedure as before (Fig. 4.23). This time, a stable signal for both species can be observed at all temperatures during SOFC mode. However, at 600 °C no conversion at voltages higher than U_{OCV} can be identified. This may be the result of cell degradation since the ratio of H_2 and O_2 reaction rate has to be 1:2 and according to Fig. 4.21 a change in H_2-signal exists. Please remember that reducing and oxidising compartment were measured consecutively since only one mass spectrometer was available. The pre-history of both measurements is thus different with the measurement in Fig. 4.23 being performed after the cell has been exposed to high temperatures for a significantly longer time.

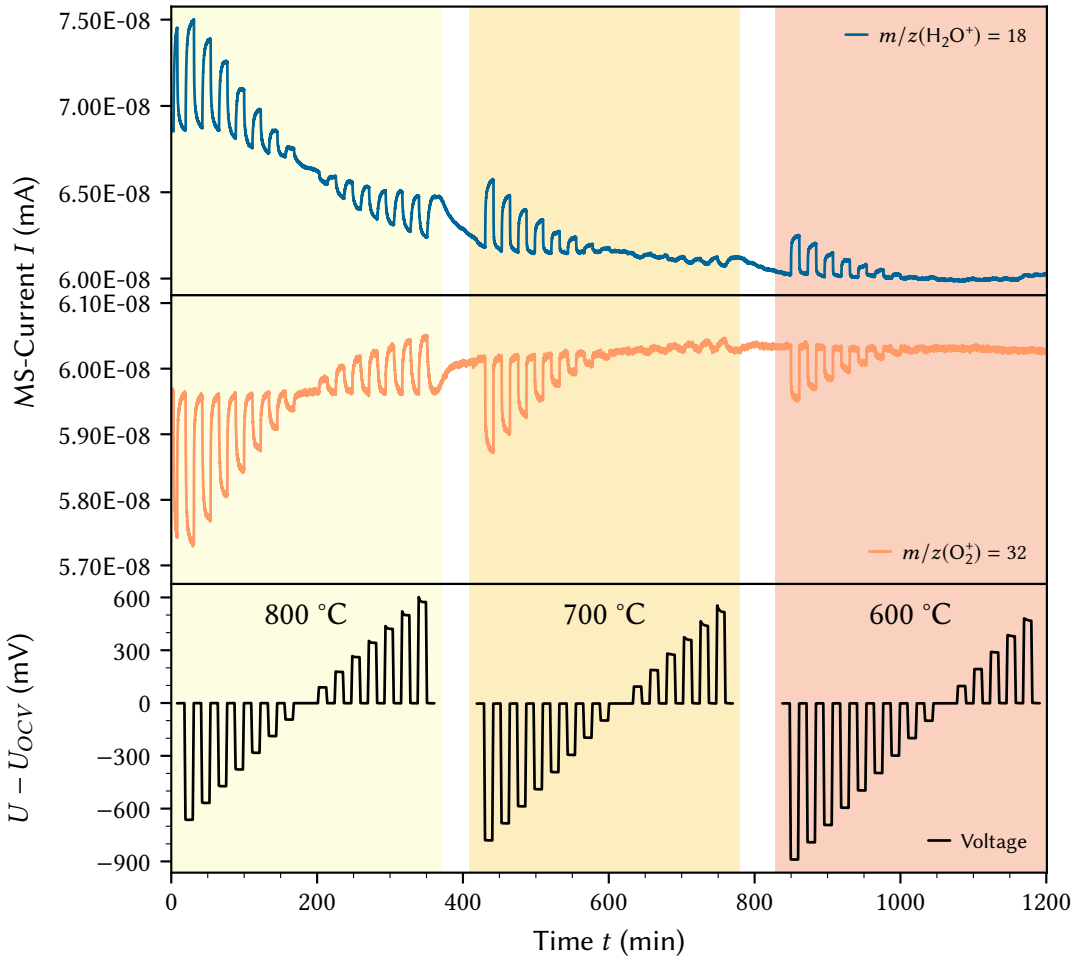

Figure 4.23.: Conversion of O_2 and H_2O over time in the oxidising compartment of a cell using LSF electrodes and a BZCY electrolyte for voltages from 0 to 1400 mV at temperatures ranging from 800 to 600 °C.

Another indicator for this assumption can be found in the I-V curves recorded for each compartment at all respective temperatures (see Fig. 4.24). The current of measurements in the oxidising compartment is mostly lower than its reducing counterpart, which was recorded around 15 h later.

The same trend can be seen for the other electrode materials LSBF and BLF. Their H_2O, H_2 and O_2 conversion plots as well as their I-V curves can be found in App. B.

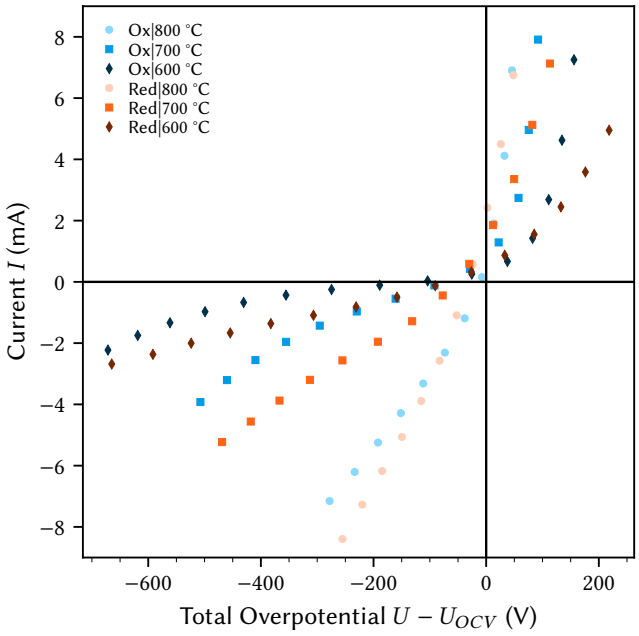

Figure 4.24.: I-V curves of LSF on BZCY electrolyte in oxidising and reducing atmospheres at temperatures ranging from 800 to 600 °C.

4.5.3. Oxygen Ion Conductor

Similar to the other experiments, the whole procedure was also conducted using symmetric cells of LSF and BLF electrodes on polycrystalline yttria-stabilised zirconia (pYSZ) electrolytes. YSZ is known to exclusively transport oxide ions. Therefore, no proton transport is expected. Fig. 4.25 shows the conversion of H_2 and H_2O over time in the reducing compartment of a cell using LSF electrodes and pYSZ electrolyte for voltages from 0 to 1400 mV at temperatures ranging from 800 to 600 °C.

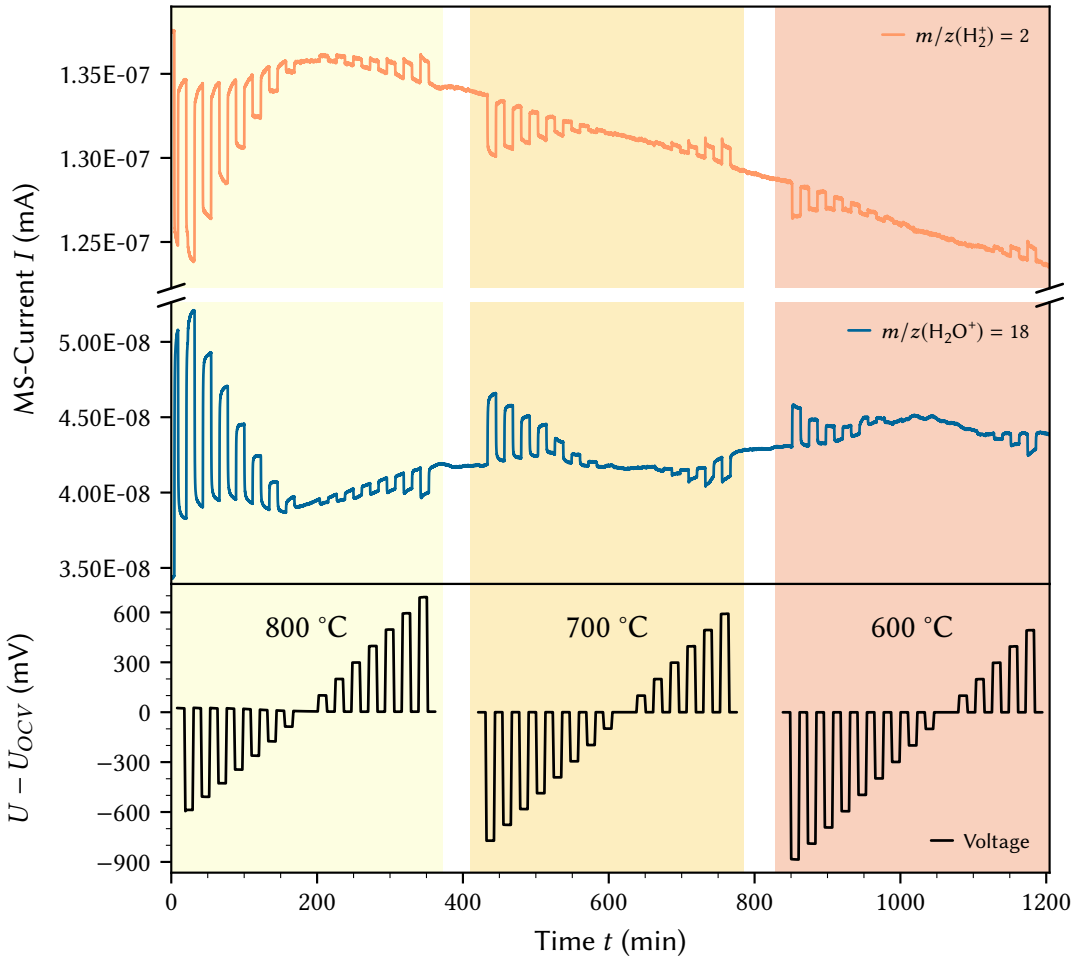

Figure 4.25.: Conversion of H_2 and H_2O over time in the reducing compartment of a cell using LSF electrodes and a pYSZ electrolyte for voltages from 0 to 1400 mV at temperatures ranging from 800 to 600 °C.

Compared to Fig. 4.21 a clear change of the H_2O-signal can be observed, even at low temperatures. Fig. 4.26 shows the following measurement of the oxidising compartment.

There, the H_2O signal shows only a slightly drifting background indicating no noticeable reaction. For O_2 however, the same trend as before (see Subsec. 4.5.2) can be observed. The evolution of O_2 under SOEC mode especially at low temperatures is weaker than the H_2 evolution (compare Fig. 4.25 and Fig. 4.26), which again indicates degradation of the cell.

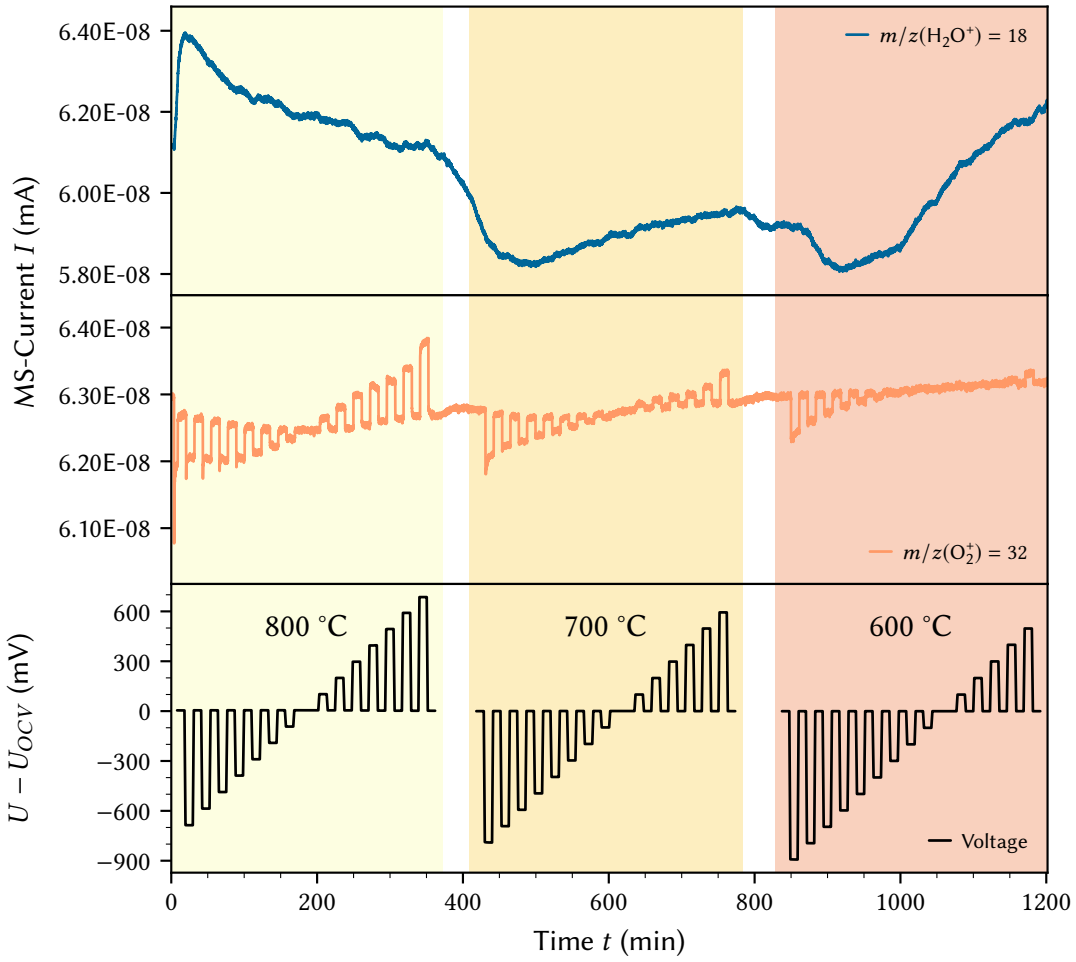

Figure 4.26.: Conversion of O_2 and H_2O over time in the oxidising compartment of a cell using LSF electrodes and a pYSZ electrolyte for voltages from 0 to 1400 V at temperatures ranging from 800 to 600 °C.

Similarly the I-V curves also show a lower current for the later measurements (see Fig. 4.27). All these trends are reproducible on BLF electrode materials, as can bee seen in App. B.

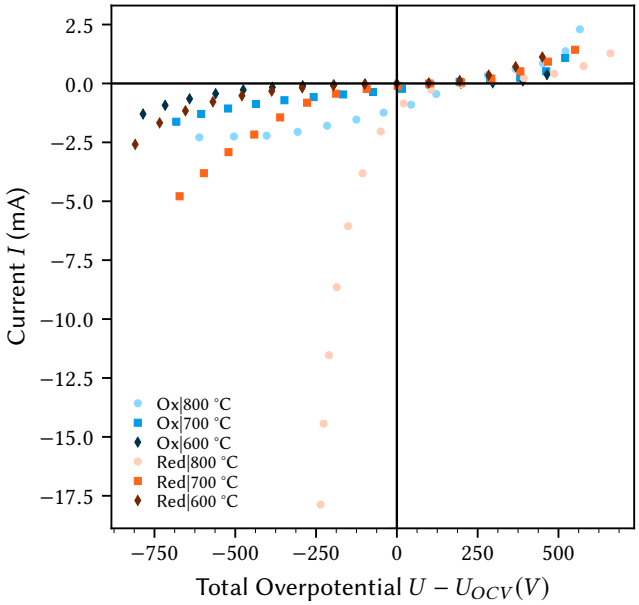

Figure 4.27.: I-V curves of LSF on pYSZ electrolyte in oxidising and reducing atmospheres at temperatures ranging from 800 to 600 °C.

4.5.4. Transference Numbers

In order to obtain the transference numbers of each charge carrier, the actual molar flows of each species of interest had to be calculated. In general, the actual reaction rate $\Delta\dot{n}_s$ of species s is given as the difference between the incoming (i) molar flow $\dot{n}_s^i$ and the outgoing (o) molar flow $\dot{n}_s^o$, as shown in Eq. (4.15)

$$\Delta\dot{n}_s = \dot{n}_s^i - \dot{n}_s^o \tag{4.15}$$

The former can be calculated using Eq. (4.16), where $\dot{V}_s$ is the partial volume flow of species s (see Subsec. 3.3.4), P the total pressure (101 325 Pa), R the ideal gas constant (8.314 J K^{-1} mol^{-1}), T the temperature and χ_{MS} a proportionality factor, which is used to calculate the outgoing flow. For the incoming flow it has the value of 1.

$$\dot{n}_s^l = \frac{\dot{V}_s P}{RT} \chi_{MS} \tag{4.16}$$

In order to obtain the outgoing flow the evolution of the m/z-ratios of each species had to be evaluated. This was done by calculating the ratio between the measured ion current I_{MS} at each voltage step and its U_{OCV} counterpart I_{MS}^{OCV} (see Eq. (4.17)).

$$\chi_{MS} = \frac{I_{MS}}{I_{MS}^{OCV}} \tag{4.17}$$

In Fig. 4.28 an example of H_2O-evolution over time is shown. Multiple data points were taken at each plateau as well as before and after to account for signal drift and peak form. Related data points were given the same colour.

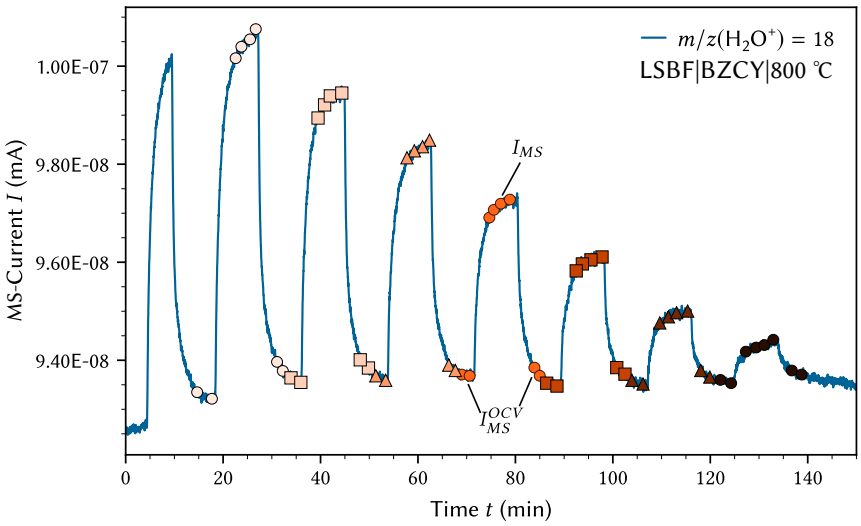

Figure 4.28.: Example H_2O-evolution over time on LSBF|BZCY|LSBF-cells at 800 °C in the oxidising compartment and the calculation of the proportional via the faradaic current.

The factor χ_{MS} can be smaller or lager than 1, depending on whether s is consumed ($\chi_{MS} < 1$) or produced ($\chi_{MS} > 1$). At equilibrium, no reactants are converted and χ_{MS} is exactly 1.

Using this starting point, transference numbers can be obtained. As described in Subsec. 4.5.2 and Subsec. 4.5.3 the cells likely suffered from significant degradation, which is especially noticeable in the SOEC mode. Therefore, only the SOFC mode is considered. Fig. 4.29 gives an overview over all reaction pathways including the different molar flows and their following nomenclature.

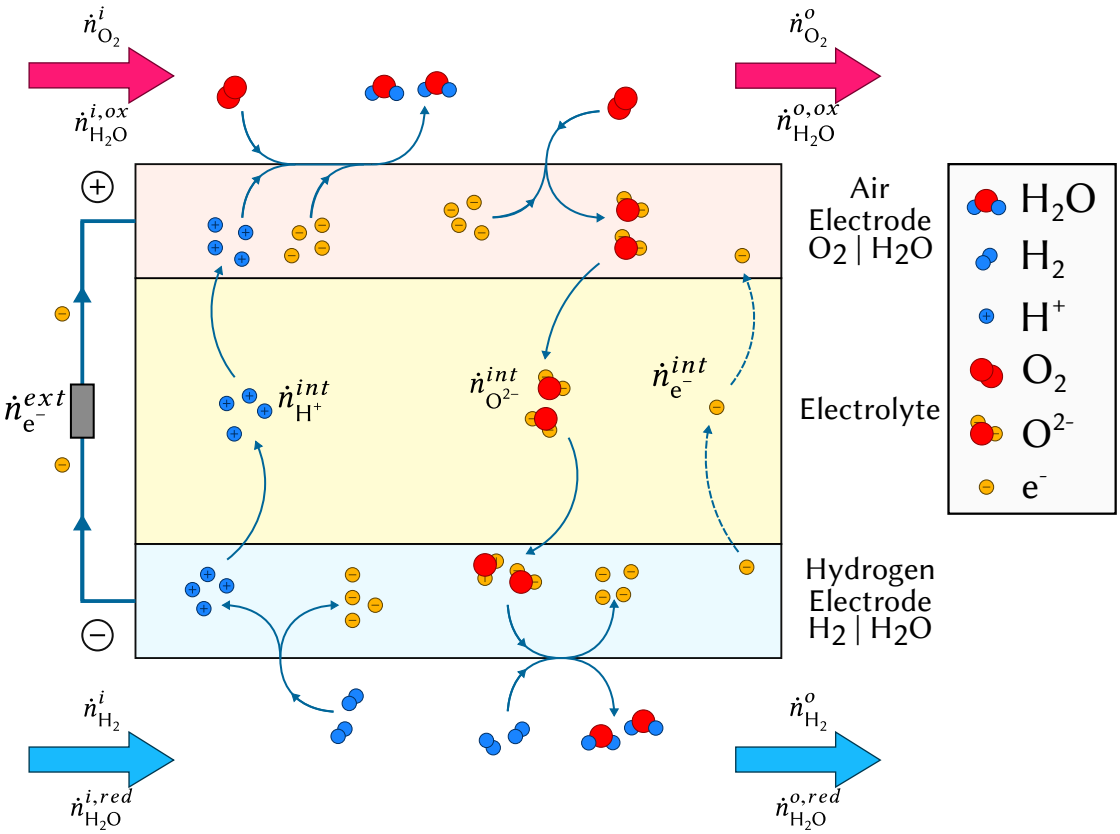

Figure 4.29.: Stoichiometric schematic of all reactions pathways during SOFC mode including molar flows $\dot{n}^{l}_{s}$ of species s in location l

All occurring reactions were already discussed in Subsec. 4.5.1. In addition to them, a possible internal electron molar flow $\dot{n}^{int}_{e^-}$ is shown, which will be neglected for the sake of simplicity in the transference number calculation. The important relations between measured gas species and ionic currents are as follows:

- $\dot{n}^{int}_{H^+}$ is exclusively responsible for $\Delta\dot{n}^{ox}_{H_2O}$
- $\dot{n}^{int}_{O^{2-}}$ is exclusively responsible for $\Delta\dot{n}^{ox}_{H_2O}$

This has already been described by Eq. (4.13) and Eq. (4.14). However, due to the potential degradation a direct evaluation would lead to inaccurate results. To compensate for this an adjustment factor ν was calculated taking advantage of the fixed 1:2 ratio of $\Delta\dot{n}_{H_2}$ and $\Delta\dot{n}_{O_2}$ (see Eq. (4.18)). This factor is between 1.8 and 4.

$$\nu = \frac{\Delta\dot{n}_{H_2}}{2\Delta\dot{n}_{O_2}} \tag{4.18}$$

Thus, the internal proton and oxide ion flow can be calculated according to Eq. (4.19) and Eq. (4.20).

$$\dot{n}^{int}_{H^+} = 2\Delta\dot{n}^{ox}_{H_2O}\nu \tag{4.19}$$

$$\dot{n}^{int}_{O^{2-}} = \Delta\dot{n}^{ox}_{H_2O}\nu \tag{4.20}$$

The total ion current I_{ion} is then given by Eq. (4.21), where z_s is the number of electrons of species s and F is Faraday's constant (96 485 C mol^{-1}).

$$I_{ion} = |z_{H^+}|F\dot{n}^{int}_{H^+} + |z_{O^{2-}}|F\dot{n}^{int}_{O^{2-}} \tag{4.21}$$

Transference numbers t_s of species s is given as the fractional contribution of each charge carrier to the total current, which results in Eq. (4.22).

$$1 = \frac{I^{int}_{H^+}}{I_{ion}} + \frac{I^{int}_{O^{2-}}}{I_{ion}} = t_{H^+} + t_{O^{2-}} \tag{4.22}$$

The obtained transference numbers and their error bars for LSF electrodes on a BZCY electrolyte at all measured temperatures are shown in Fig. 4.30. In this case the oxide ion conductivity amounts to 0.1 of the total ion current. The missing bars at higher bias steps (700 to 800 mV) result from either approaching U_{OCV} (for 800 °C) or no discernable signal (for 700 to 600 °C).

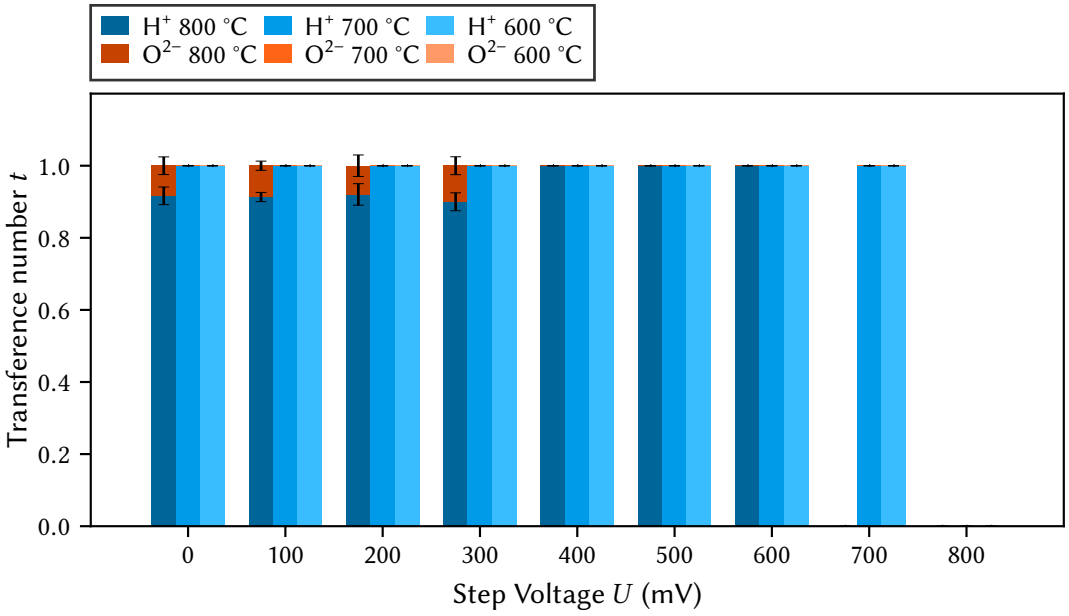

Figure 4.30.: Transference numbers t of protons (H^+) and oxide ions (O^{2-}) in SOFC mode at temperatures from 800 to 600 °C and various (0 to 800 mV) voltages for LSF on BZCY.

To confirm this method, Fig. 4.31 shows the transference numbers obtained with LSF electrodes on a pYSZ electrolyte at all measured temperatures. As expected, no proton conductivity can be observed. The same reasons for the missing bars at higher bias steps apply like explained above.

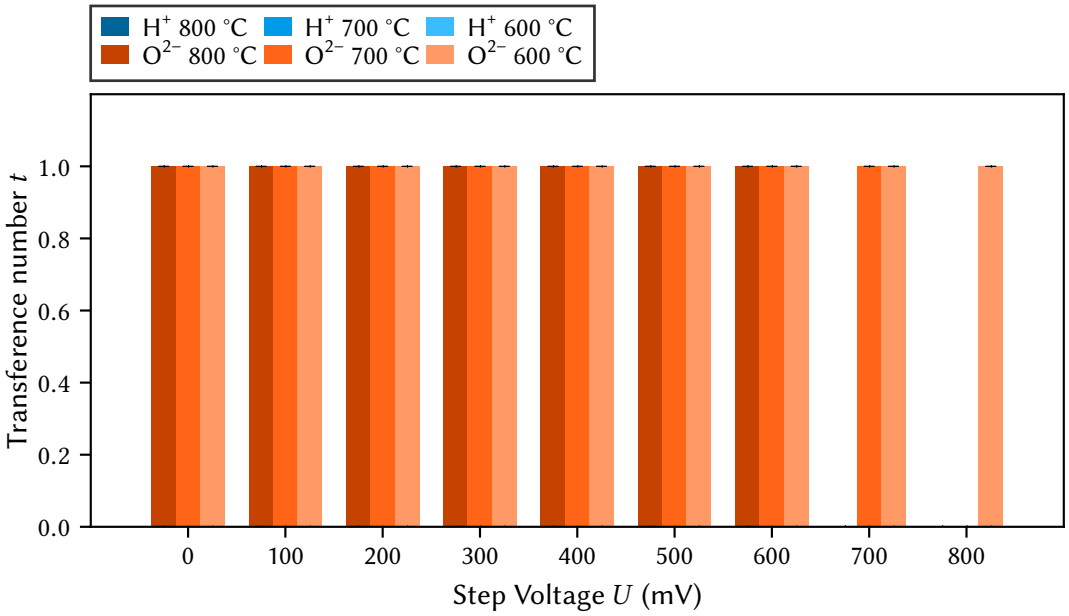

Figure 4.31.: Transference numbers t of protons (H^+) and oxide ions (O^{2-}) in SOFC mode at temperatures from 800 to 600 °C and various (0 to 800 mV) voltages for LSF on pYSZ.

The remaining transference number plots for all bias steps can be found in App. B. In the case of BLF|BZCY|BLF cells $t_{O^{2-}}$ of around 0.15 are obtained at the highest temperature. This is also the case for LSBF. In addition, LSBF cells also exhibit small oxide ion conductivity at 700 °C ($t_{O^{2-}} \approx 0.05$). BLF cells with pYSZ electrolyte show the same behaviour as their LSF counterparts before. To summarise these results Fig. 4.32 gives an overview over the transference numbers of all samples at all temperatures and $U = 0$ mV (i.e. short circuited cell in SOFC mode).

In conclusion, it was found that a proton conducting electrolyte may show slight oxide ion conductivity ($t_{O^{2-}} \leq 0.15$) at 800 °C. By lowering the temperature this decreases drastically with virtually no oxide ion conductivity at 700 or 600 °C.

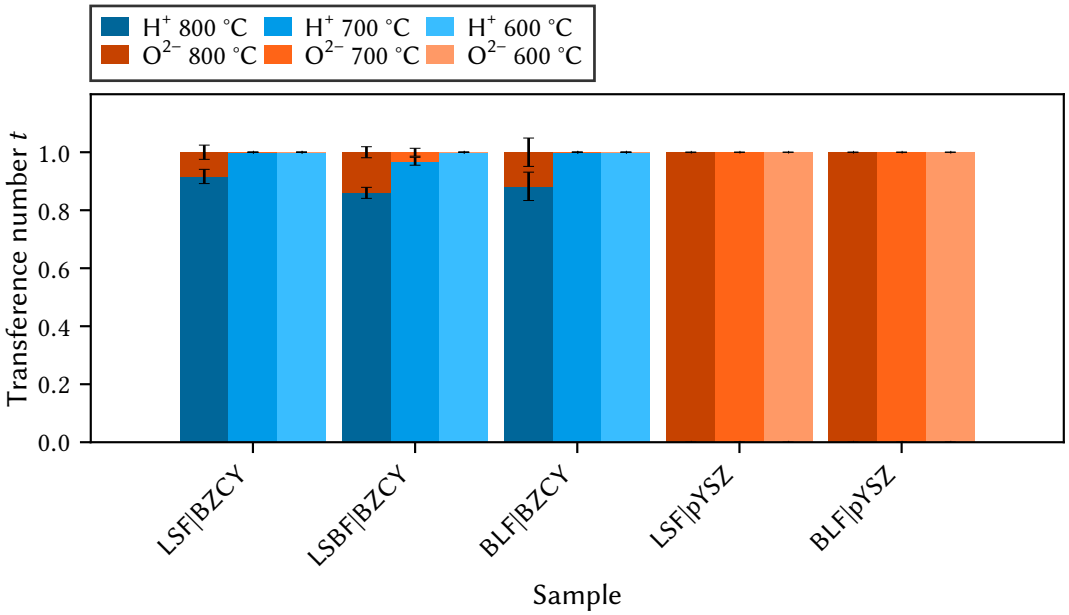

Figure 4.32.: Transference numbers t of protons (H^+) and oxide ions (O^{2-}) in SOFC mode at temperatures from 800 to 600 °C for all samples at $U = 0\,\mathrm{mV}$ (short circuit of cell).

5. Mechanistic Conclusion

Based on the results in the previous chapter first mechanistic conclusions can be drawn. To facilitate this, possible reaction pathways for the H_2 oxidation process on a pervoskite MIEC electrode with both, proton and oxide ion conducting capabilities, had to be considered. The result is shown in Fig. 5.1.

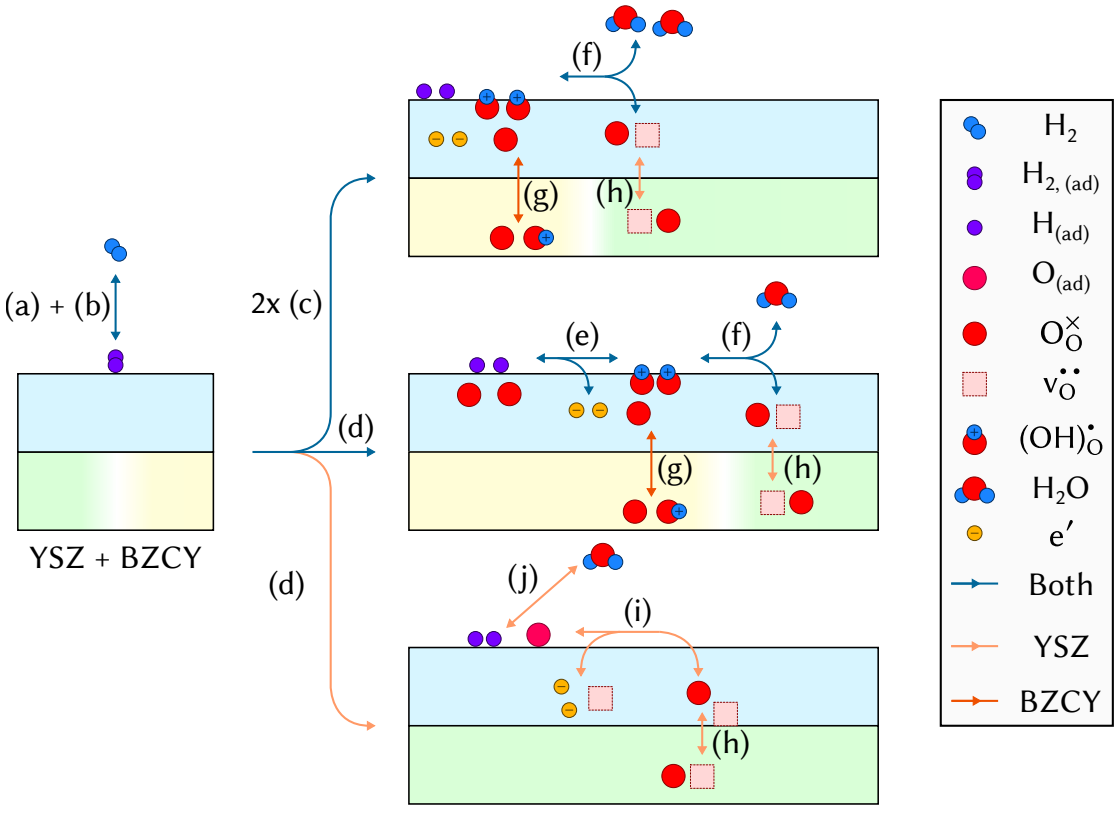

Figure 5.1.: Mechanistic Considerations of possible reaction pathways on both proton and oxide ion conductor (see text for more details).

To retain the overview, each typ of electrolyte, BZCY and YSZ, was given a specific colour (yellow and green, respectively). Due to the multitude of pathways, the possible reactions are sketched in three different images. Based on current knowledge there is no clear ranking, which pathway may be favoured.

In the first steps the hydrogen molecule diffuse to the surface of the electrode (a). Afterwards, it adsorbs on the electrode surface (Eq. (5.1)). The exact elementary steps in the formation of a surface $(OH)^{\bullet}_{O\,(surf)}$ are not known. Multiple options are possible. The $H_{2\,(ad)}$ either dissociates by forming one hydroxyl defect, while one hydrogen remains adsorbed at the surface (Eq. (5.2)) or it splits into two single hydrogen atoms $H_{(ad)}$ at the surface (Eq. (5.3)). The former may be energetically favourable [54–56]. Instead of adsorbing as a molecule, H_2 may also adsorb by dissociative adsorption.

$$(b)\quad H_{2\,(gas)} \rightleftharpoons H_{2\,(ad)} \tag{5.1}$$

$$(c)\quad H_{2\,(ad)} + O^{\times}_{o} \rightleftharpoons (OH)^{\bullet}_{O\,(surf)} + e' + H_{(ad)} \tag{5.2}$$

$$(d)\quad H_{2\,(ad)} \rightleftharpoons 2\,H_{(ad)} \tag{5.3}$$

The next steps partly depend on the ionic charge carrier in the used electrolyte. The adsorbed hydrogen atoms are incorporated into the oxide after donating their electron to the electrode (Eq. (5.4)) and following the blue path in Fig. 5.1. Afterwards, the hydroxyl groups can either form water (Eq. (5.5)), leaving a surface vacancy and an oxide ion behind, or hand the hydrogen over to another oxide ion in the crystal bulk, thus leading to an ionic current via the electrolyte towards the counter electrode. The former would be coupled to an oxide ion current, while the latter is only possible on a proton conductor (Eq. (5.6)).

$$(e)\quad 2\,H_{(ad)} + 2\,O^{\times}_{O\,(surf)} \rightleftharpoons 2\,(OH)^{\bullet}_{O\,(surf)} + 2\,e' \tag{5.4}$$

$$(f)\quad 2\,(OH)^{\bullet}_{O\,(surf)} \rightleftharpoons H_2O + v^{\bullet\bullet}_{O\,(surf)} + O^{\times}_{O\,(surf)} \tag{5.5}$$

$$(g)\quad (OH)^{\bullet}_{O\,(surf)} + O^{\times}_{O\,(bulk)} \rightleftharpoons O^{\times}_{O\,(surf)} + (OH)^{\bullet}_{O\,(b)} \tag{5.6}$$

On the other hand, by following the orange path in Fig. 5.1, oxide ions move to the electrode surface via vacancies (Eq. (5.7)). There, they can leave the crystal, leaving two electrons behind while forming oxygen surface adsorbates and creating a vacancy in the electrode (Eq. (5.8)). The adsorbed $O_{(ad)}$ can form water with two adsorbed hydrogen atoms, which then desorbs from the crystal (Eq. (5.9)).

$$(h) \quad O^{\times}_{O\,(bulk)} + v^{\bullet\bullet}_{O\,(surf)} \rightleftharpoons v^{\bullet\bullet}_{O\,(bulk)} + O^{\times}_{O\,(surf)} \tag{5.7}$$

$$(i) \quad O^{\times}_{O\,(surf)} \rightleftharpoons O_{(ad)} + v^{\bullet\bullet}_{O\,(surf)} + 2\,e' \tag{5.8}$$

$$(j) \quad 2\,H_{(ad)} + O_{ad} \rightleftharpoons H_2O_{(ad)} \rightleftharpoons H_2O_{(gas)} \tag{5.9}$$

Based on the results known from literature and the present study a decent amount of the mentioned steps can already be excluded as being the *rds*. Both, oxide ion and proton conduction in the bulk (Eq. (5.6) and Eq. (5.7)) are only rate limiting at low temperatures, as shown in Sec. 4.3. The formation of water at the cost of two hydroxyl groups via an acid-base reaction (Eq. (5.5)) is a fast process, as already proven in literature [57]. The formation of water via an adsorbed oxygen and two hydrogen atoms can also be ruled out due to the fact that this formation only happens on electrolytes with oxide ion conducting capabilities. Since the transference number results in Sec. 4.5 confirm that O^{2-} ions to only play a minor (if any) role on proton conducting electrolytes this possibility can be excluded especially for temperatures of 600 °C and below. The *rds* is, on the contrary, most likely the same for both electrolyte types. Thus, it has to be either the adsorption and subsequent dissociation of the hydrogen molecule (Eq. (5.1) and Eq. (5.3)) or the incorporation of hydrogen into the crystal together with an electron transfer (Eq. (5.2) and Eq. (5.4)).

6. Summary and Outlook

Various perovskite type anode materials for proton conducting fuel cells (PCFC) are applied as thin film electrodes on proton and oxide ion conducting electrolytes. In particular, pellets of polycrystalline BZCY and YSZ single crystals were used as electrolytes, respectively. Ti/Pt current collector grids were deposited using lift-off photolithography and sputter deposition in order to ensure homogeneous polarisation of the subsequently PLD-grown thin film electrodes. These were produced via pulsed laser deposition. Impedance spectroscopy and DC characterisation techniques (I-V curves) were used for electrochemical characterisation of these thin films. Specific parameters like temperature, bias, composition of gas atmosphere or active electrode area were varied.

First, the conductivity of the purchased proton conducting BZCY pellets was characterised. Symmetrical cells with brush deposited porous Pt electrodes were prepared and EIS experiments in temperatures ranges of 700 to 200 °C and both oxidising as well as reducing atmosphere were conducted. The resistance of charge transport through the material was extracted from the impedance spectra by CNLS-fitting. Arrhenius plots of the conductivities derived from these resistances revealed activation energies of 0.4 eV for proton conduction, which is in excellent agreement with literature data of similar compounds. Additionally, in oxidising conditions the impact of electron hole conduction was shown to increase strongly with temperature.

The temperature dependence of the area related surface resistance of symmetrical cells using LSF and LSBF electrodes on BZCY and YSZ in reducing conditions was then investigated by EIS. Fitting the resulting Nyquist plots revealed that the used electrolyte had only small impact on the obtained *ASR* values (average: 15 Ω cm^2 at 600 °C) and activation energies (between 0.4 and 0.75 eV). This results can be regarded as an indication that the rate determining step of H_2 oxidation is independent of the involved ionic charge carrier.

I-V curves measured on LSF and LSBF electrodes on BZCY electrolytes at 600 °C further support this interpretation. Especially close to equilibrium conditions (± 50 mV) no indication of transport limitation of protons in the electrode was found. This supports the interpretation that the dominant electrode polarisation resistance indeed originates from a surface process. At stronger polarisation, however, the electrode material with expectedly lower proton concentration (LSF) showed kind of a limiting current and a significantly lower performance.

Electrochemical and MS experiments were coupled by a novel measuring apparatus with two separate gas compartments to obtain the transference number of each charge carrier in both electrolytes. The current through the cell at voltages ranging from 0 to 1.4 V at three different temperatures (800 °C, 700 °C and 600 °C) was measured. Simultaneously, the composition of the atmosphere in each gas compartment was analysed with the mass spectrometer. The step heights between signals obtained at a voltage step and open circuit could then be used to calculate the molar flow of each component in the system. Thus, transference numbers of each charge carrier could be obtained.

Depending on the applied voltage, the cell was operated in either SOFC (water evolution, $U_{Bias} < U_{OCV}$) or SOEC (water splitting, $U_{Bias} > U_{OCV}$) mode. Multiple signs like loss of current and a shift of the fixed $H_2|O_2$-ratio point towards cell degradation. Thus, the transference number evaluation was conducted exclusively for the SOFC mode. Irregardless of the electrode material in question the transference number for oxide ions on BZCY never exceeded 0.15 at 800 °C and tends towards zero at lower temperatures. On the contrary, an oxide ion conducting electrolyte like YSZ showed no proton conductivity at all. In conclusion, a proton conduction on the investigated MIEC electrodes could be proven. The current pathway via oxide ions is shown to be negligible on these MIEC materials with a proton conducting electrolyte.

Combining the impedance, I-V curve, and electrochemical pumping results it can be concluded that the H_2 oxidation reaction on mixed conducting PCFC anodes indeed proceeds via a pathway involving protons in the electrode reactions. Moreover, the rate determining elementary step of this proton-related pathway appears to be identical to the *rds* of an oxide-ion-related H_2 oxidation pathway on MIEC anodes in conventional SOFCs. As the most likely candidates, H_2 dissociation, or an oxidative dissociation of H_2, or the oxidation of adsorbed hydrogen can be identified.

A. Electrolyte Characterisation

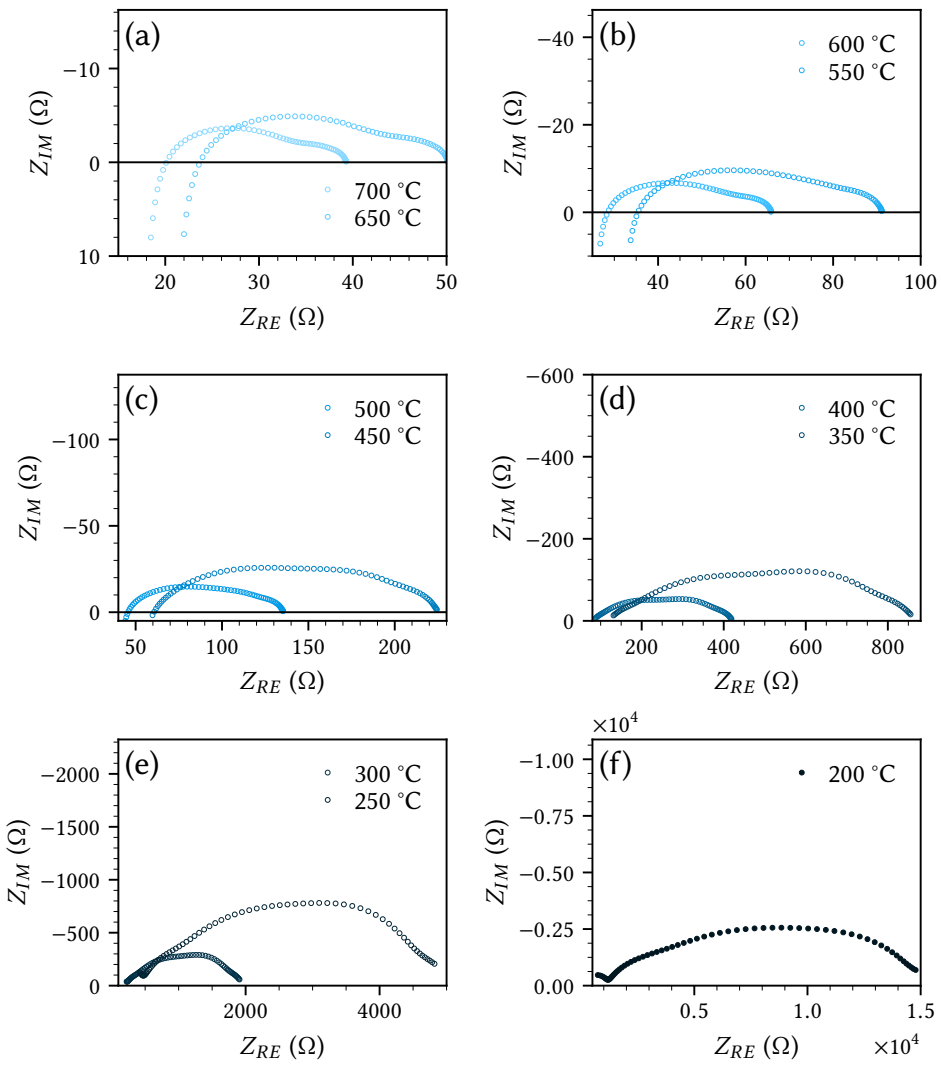

Figure A.1.: Nyquist plots of BZCY with porous YSZ|Pt cermet electrodes in reducing atmosphere (2.5 % H_2/2.5 % H_2O) in a temperature range of 700 to 200 °C

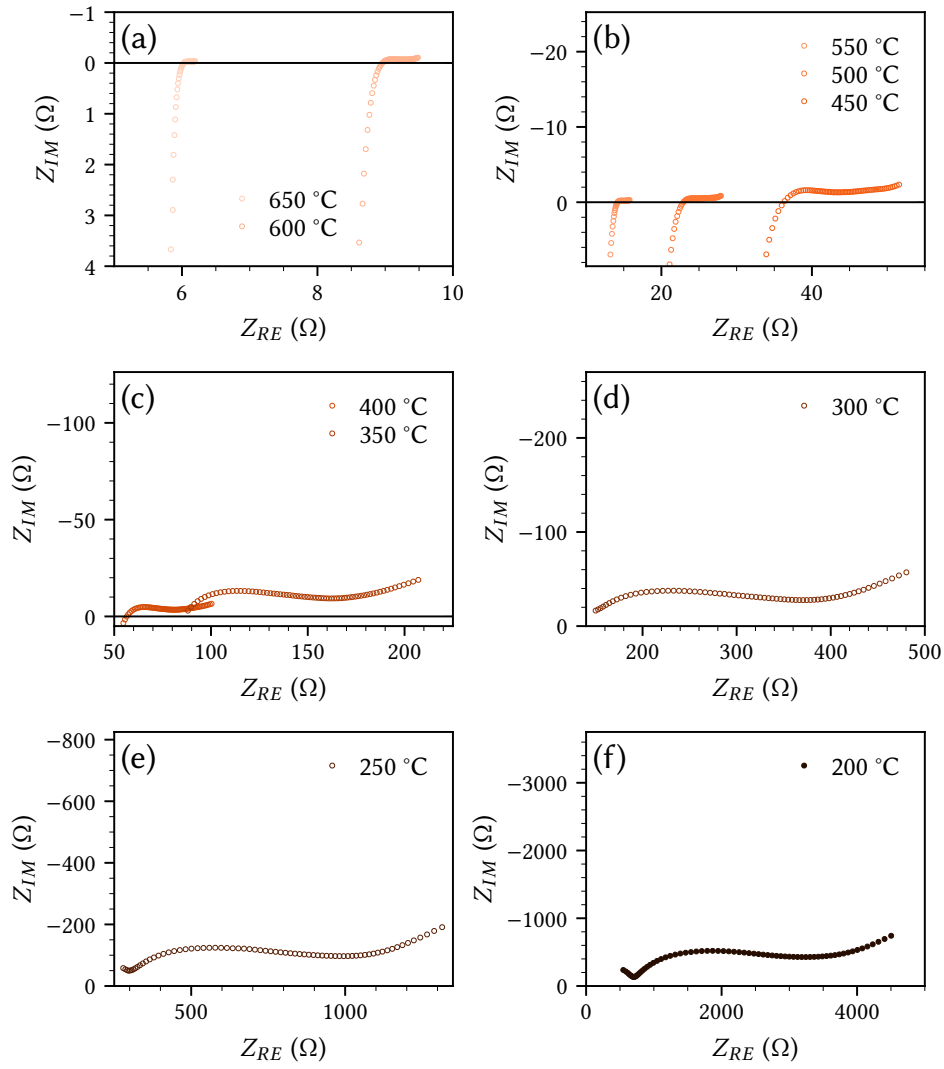

Figure A.2.: Nyquist plots of BZCY with porous cermet Pt|YSZ cermet electrodes in oxidising atmosphere (O_2/2.5 % H_2O) in a temperature range of 650 to 200 °C

B. 2-Gas Measurements

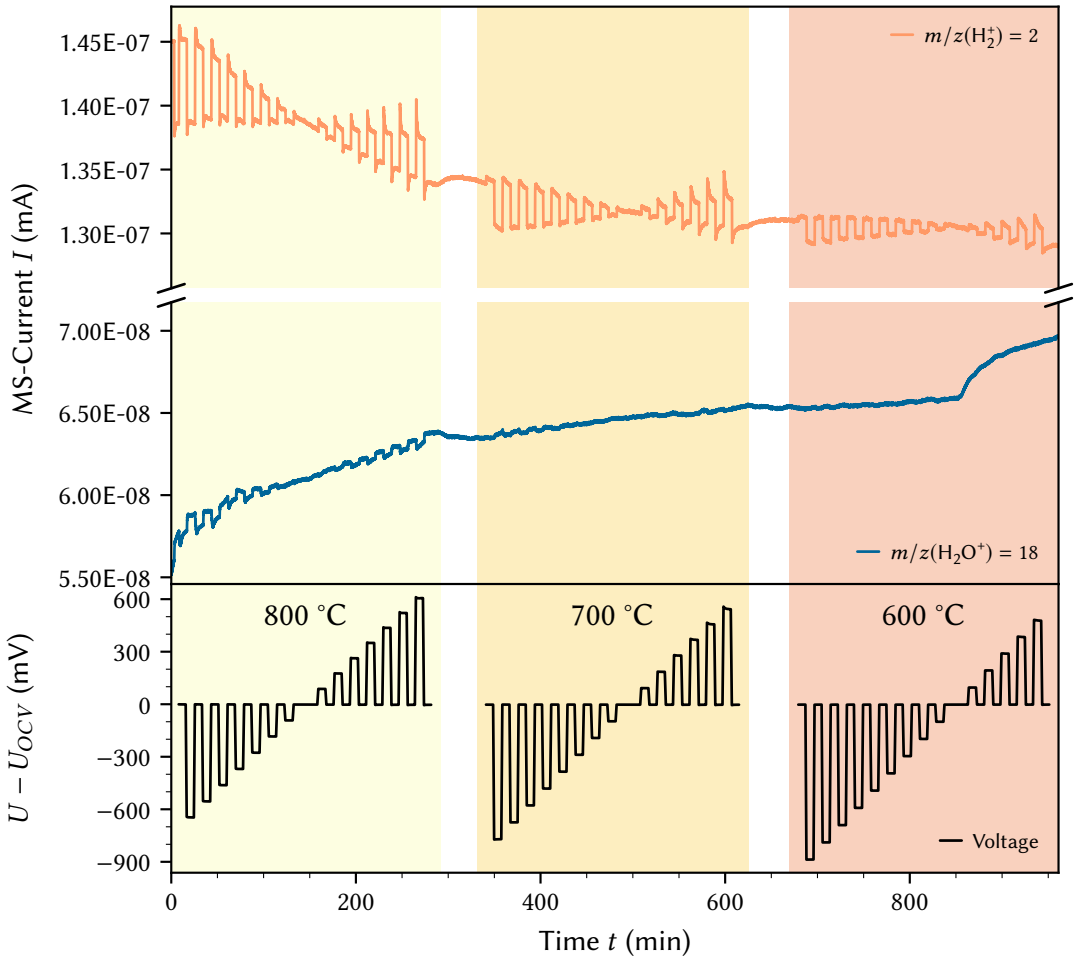

Figure B.1.: Conversion of H_2 and H_2O over time in the reducing compartment of a cell using LSBF electrodes and a BZCY electrolyte for voltages from 0 to 1400 mV at temperatures ranging from 800 to 600 °C.

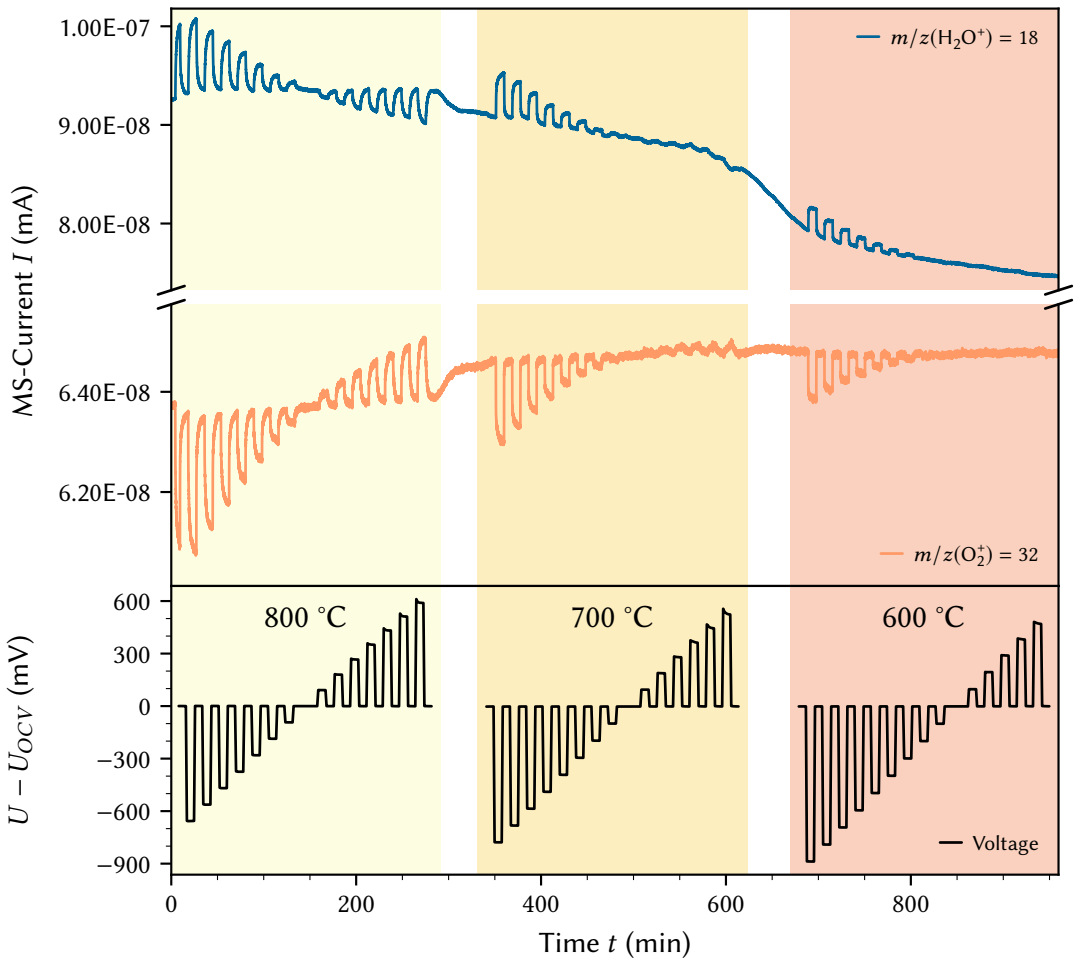

Figure B.2.: Conversion of O_2 and H_2O over time in the oxidising compartment of a cell using LSBF electrodes and a BZCY electrolyte for voltages from 0 to 1400 mV at temperatures ranging from 800 to 600 °C.

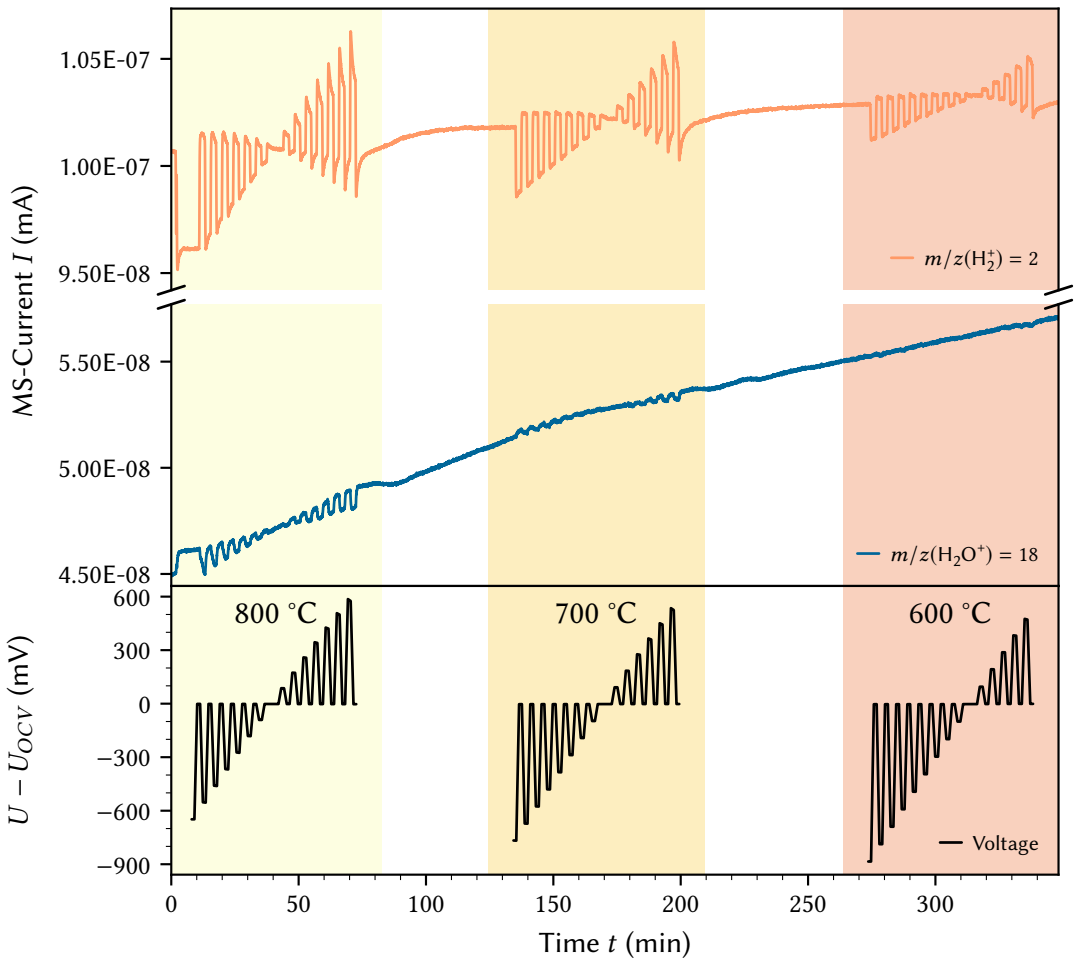

Figure B.3.: Conversion of H_2 and H_2O over time in the reducing compartment of a cell using BLF electrodes and a BZCY electrolyte for voltages from 0 to 1400 mV at temperatures ranging from 800 to 600 °C..

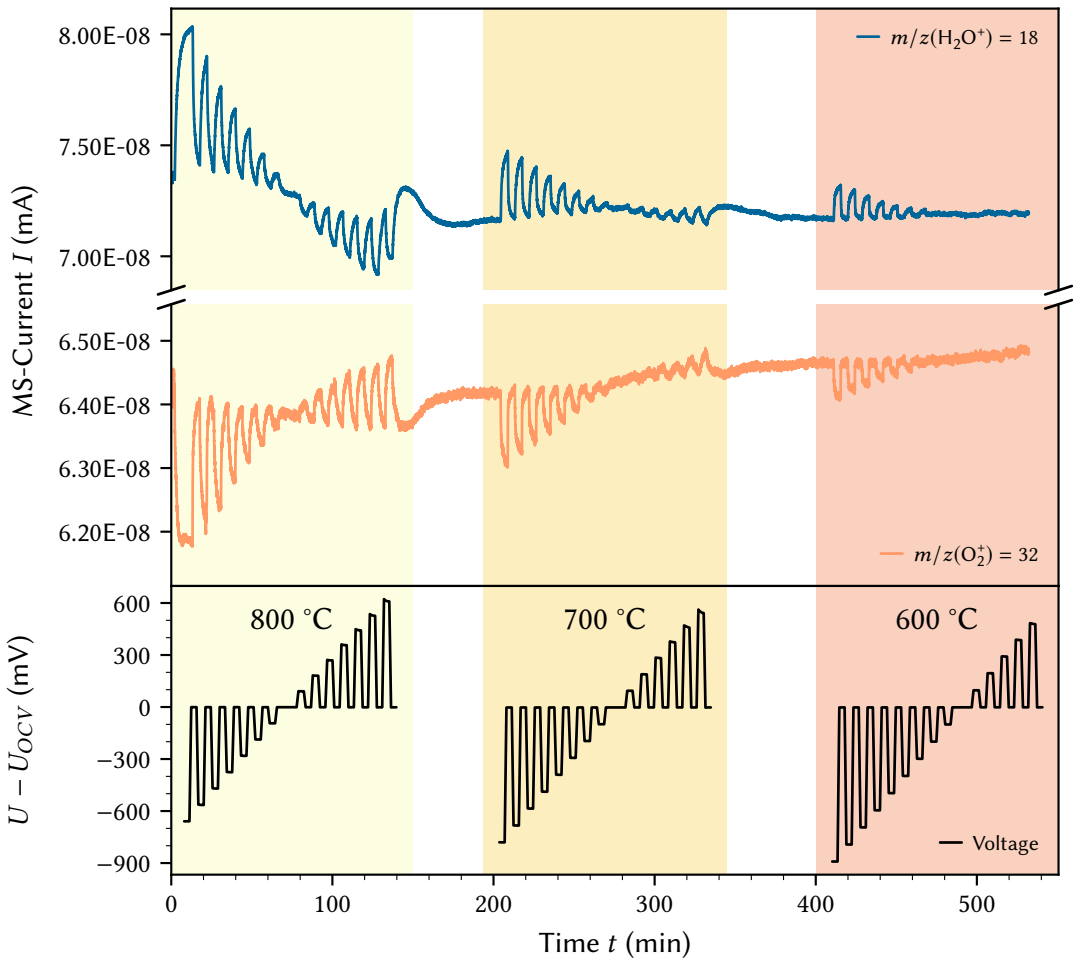

Figure B.4.: Conversion of O_2 and H_2O over time in the oxidising compartment of a cell using BLF electrodes and a BZCY electrolyte for voltages from 0 to 1400 mV at temperatures ranging from 800 to 600 °C.

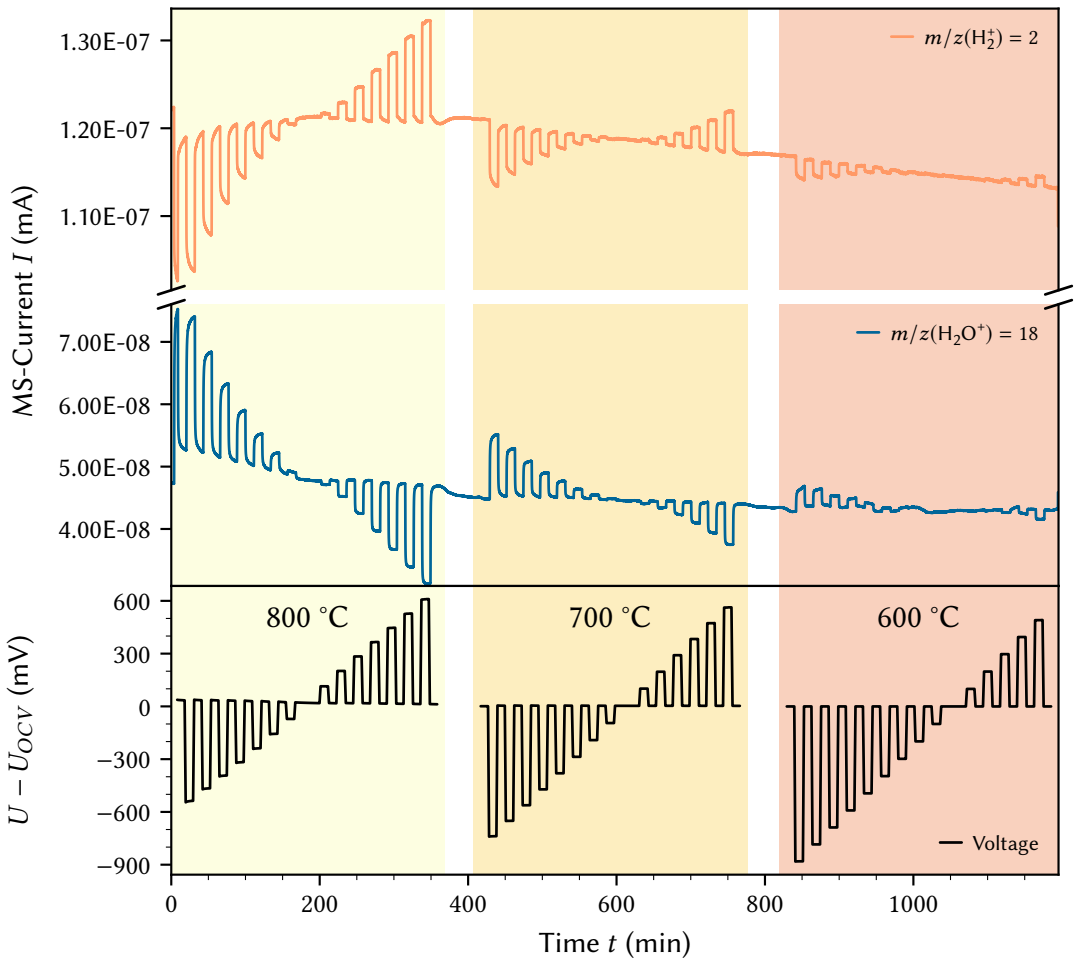

Figure B.5.: Conversion of H_2 and H_2O over time in the reducing compartment of a cell using BLF electrodes and a pYSZ electrolyte for voltages from 0 to 1400 mV at temperatures ranging from 800 to 600 °C.

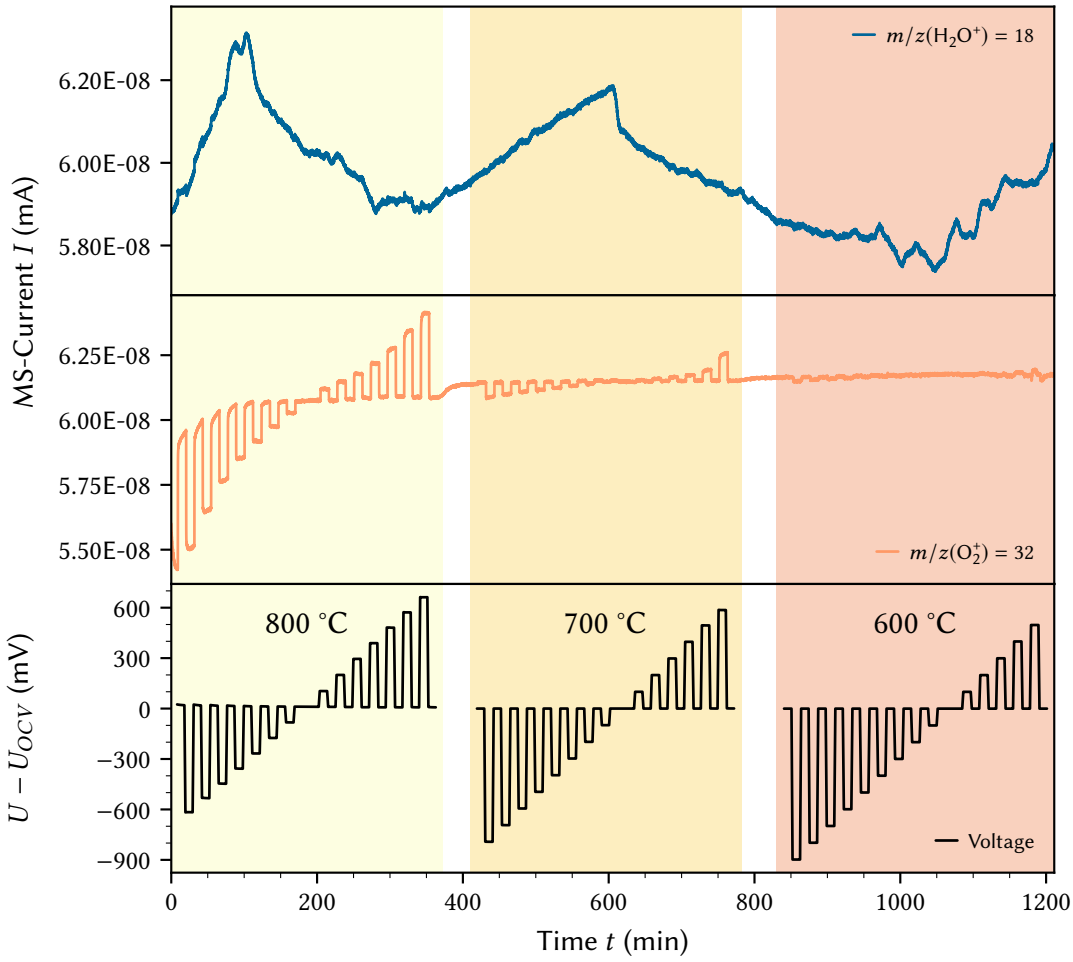

Figure B.6.: Conversion of O_2 and H_2O over time in the oxidising compartment of a cell using BLF electrodes and a pYSZ electrolyte for voltages from 0 to 1400 mV at temperatures ranging from 800 to 600 °C.

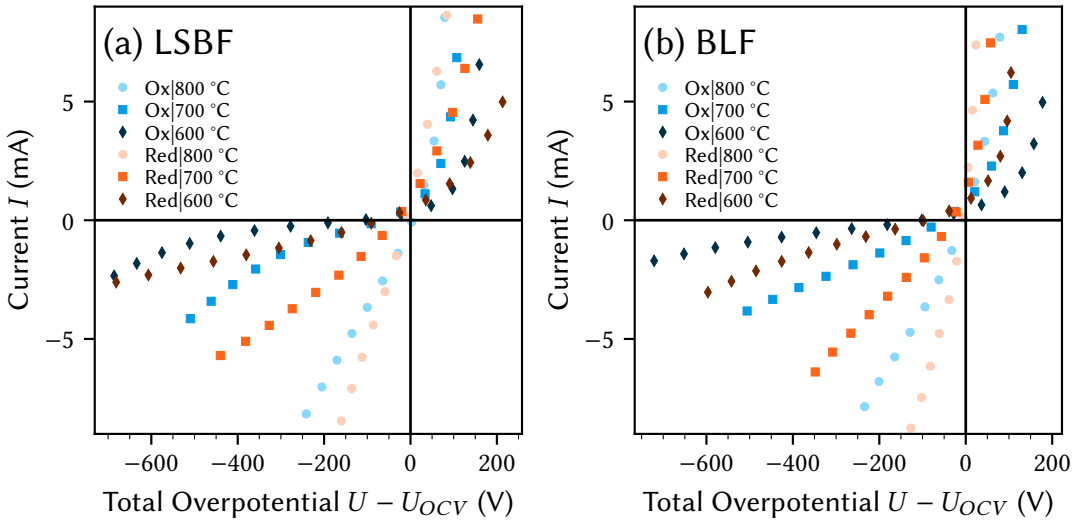

Figure B.7.: I-V curves of (a) LSBF and (b) BLF on BZCY electrolytes in oxidising and reducing atmospheres at temperatures ranging from 800 to 600 °C.

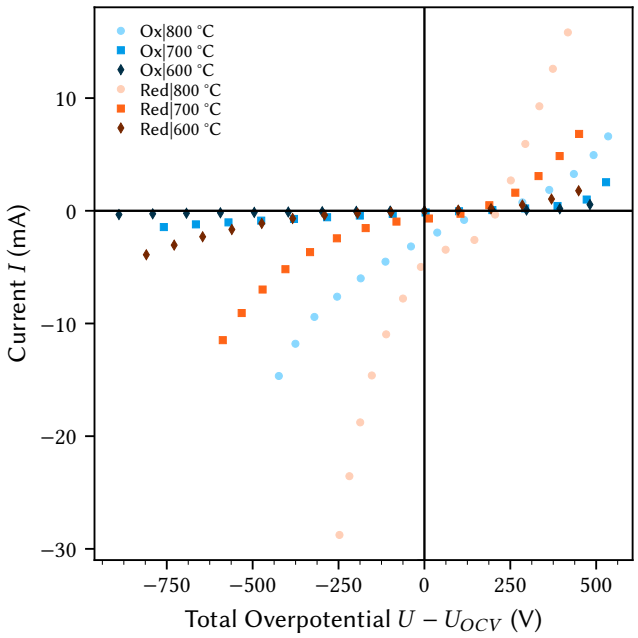

Figure B.8.: I-V curves of BLF on pYSZ electrolyte in oxidising and reducing atmospheres at temperatures ranging from 800 to 600 °C.

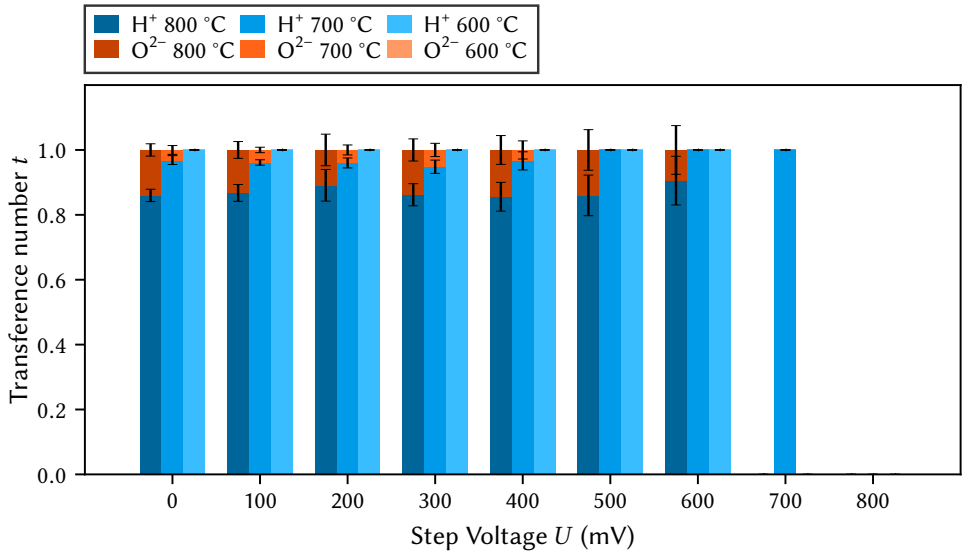

Figure B.9.: Transference numbers t of protons (H^+) and oxide ions (O^{2-}) in SOFC mode at temperatures from 800 to 600 °C and various (0 to 800 mV) voltages for LSBF on BZCY.

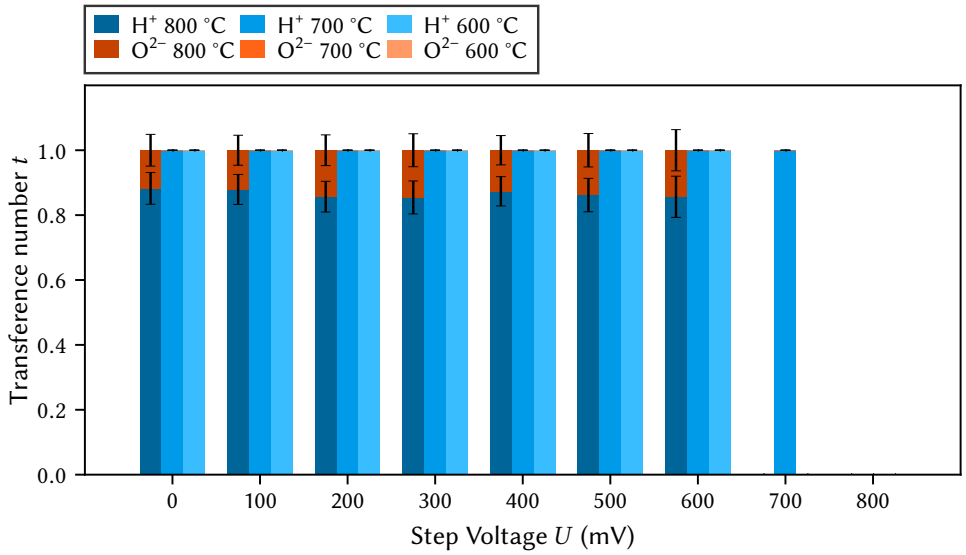

Figure B.10.: Transference numbers t of protons (H^+) and oxide ions (O^{2-}) in SOFC mode at temperatures from 800 to 600 °C and various (0 to 800 mV) voltages for BLF on BZCY.

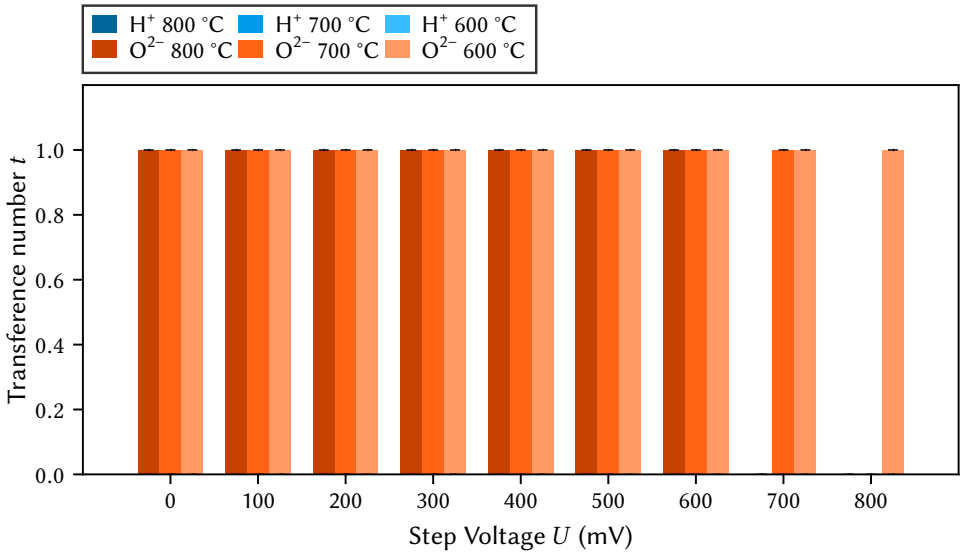

Figure B.11.: Transference numbers t of protons (H^+) and oxide ions (O^{2-}) in SOFC mode at temperatures from 800 to 600 °C and various (0 to 800 mV) voltages for BLF on BZCY.

Bibliography

[1] International Energy Agency. *Renewables 2017*. 2017.

[2] A. B. Stambouli and E. Traversa. "Fuel cells, an alternative to standard sources of energy". In: *Renewable and Sustainable Energy Reviews* 6 (2002), pp. 295–304. ISSN: 1364-0321. DOI: 10.1016/s1364-0321(01)00015-6.

[3] A. B. Stambouli and E. Traversa. "Solid oxide fuel cells (SOFCs): a review of an environmentally clean and efficient source of energy". In: *Renewable and Sustainable Energy Reviews* 6.5 (2002), pp. 433–455. ISSN: 1364-0321. DOI: 10.1016/S1364-0321(02)00014-X.

[4] Renewable Energy Policy Network for the 21st Century. *Renewables 2018*. 2018.

[5] E. Fabbri, L. Bi, D. Pergolesi, and E. Traversa. "Towards the Next Generation of Solid Oxide Fuel Cells Operating Below 600 °C with Chemically Stable Proton-Conducting Electrolytes". In: *Advanced Materials* 24.2 (Sept. 2011), pp. 195–208. DOI: 10.1002/adma.201103102.

[6] J. Larminie and A. Dicks. *Fuel Cell Systems Explained*. John Wiley & Sons, Ltd,., Feb. 2003. DOI: 10.1002/9781118878330.

[7] N. Sammes, ed. *Fuel Cell Technology*. Springer London, 2006. DOI: 10.1007/1-84628-207-1.

[8] M. Ziomek-Moroz, G. R. Holcomb, B. S. Covino, S. J. Bullard, P. D. Jablonski, and D. E. Alman. "Corrosion Performance of Ferritic Steel for SOFC Interconnect Applications". In: *Advances in Solid Oxide Fuel Cells II: Ceramic Engineering and Science Proceedings*. Wiley-Blackwell, 2008. Chap. 20, pp. 200–209. ISBN: 9780470291337. DOI: 10.1002/9780470291337.ch20.

[9] N. Bonanos, K. Knight, and B. Ellis. "Perovskite solid electrolytes: Structure, transport properties and fuel cell applications". In: *Solid State Ionics* 79 (1995), pp. 161–170. ISSN: 0167-2738. DOI: 10.1016/0167-2738(95)00056-c.

[10] T. Yajima, H. Iwahara, and H. Uchida. "Protonic and oxide ionic conduction in BaCeO3-based ceramics - effect of partial substitution for Ba in BaCe0.9O3 with Ca". In: *Solid State Ionics* 47.1-2 (Aug. 1991), pp. 117–124. DOI: 10.1016/0167-2738(91)90189-i.

[11] R. Hui, R. Maric, C. Decès-Petit, E. Styles, W. Qu, X. Zhang, J. Roller, S. Yick, D. Ghosh, K. Sakata, and M. Kenji. "Proton conduction in ceria-doped Ba2In2O5 nanocrystalline ceramic at low temperature". In: *Journal of Power Sources* 161.1 (Oct. 2006), pp. 40–46. DOI: 10.1016/j.jpowsour.2006.03.070.

[12] J. Niwa, T. Suehiro, K. Kishi, S. Ikeda, and M. Maeda. "Structure and electrical characteristics of Ce4+-doped Ba2In2O5". In: *Journal of Materials Science* 38.18 (2003), pp. 3791–3795. DOI: 10.1023/a:1025940418380.

[13] G. Zhang. "Protonic conduction in Ba2In2O5". In: *Solid State Ionics* 82.3-4 (Dec. 1995), pp. 153–160. DOI: 10.1016/0167-2738(95)00199-8.

[14] H. Iwahara, T. Esaka, H. Uchida, and N. Maeda. "Proton conduction in sintered oxides and its application to steam electrolysis for hydrogen production". In: *Solid State Ionics* 3-4 (1981), pp. 359–363. ISSN: 0167-2738. DOI: 10.1016/0167-2738(81)90113-2.

[15] H. Iwahara, H. Uchida, and N. Maeda. "Studies on solid electrolyte gas cells with high-temperature-type proton conductor and oxide ion conductor". In: *Solid State Ionics* 32 (1983), pp. 395–402. ISSN: 0010-9355. DOI: 10.3323/jcorr1974.32.7_395.

[16] L. Chevallier, M. Zunic, V. Esposito, E. D. Bartolomeo, and E. Traversa. "A wet-chemical route for the preparation of Ni-BaCe0.9Y0.1O3 cermet anodes for IT-SOFCs". In: *Solid State Ionics* 180.9-10 (May 2009), pp. 715–720. DOI: 10.1016/j.ssi.2009.03.005.

[17] A. Essoumhi, G. Taillades, M. Tailladesjacquin, D. Jones, and J. Roziere. "Synthesis and characterization of Ni-cermet/proton conducting thin film electrolyte symmetrical assemblies". In: *Solid State Ionics* 179.38 (Nov. 2008), pp. 2155–2159. DOI: 10.1016/j.ssi.2008.07.025.

[18] L. Bi, E. Fabbri, Z. Sun, and E. Traversa. "BaZr0.8Y0.2O3-NiO Composite Anodic Powders for Proton-Conducting SOFCs Prepared by a Combustion Method". In: *Journal of The Electrochemical Society* 158.7 (2011), B797. DOI: 10.1149/1.3591040.

[19] G. Mather. "Synthesis and characterisation of Ni–SrCe0.9Yb0.1O3 cermet anodes for protonic ceramic fuel cells". In: *Solid State Ionics* 158.3-4 (Mar. 2003), pp. 333–342. DOI: 10.1016/s0167-2738(02)00904-9.

[20] S. Kogler, A. Nenning, G. M. Rupp, A. K. Opitz, and J. Fleig. "Comparison of Electrochemical Properties of La0.6Sr0.4FeO3 Thin Film Electrodes: Oxidizing vs. Reducing Conditions". In: *Journal of The Electrochemical Society* 162.3 (2015), F317–F326. DOI: 10.1149/2.0731503jes.

[21] D. Poetzsch, R. Merkle, and J. Maier. "Investigation of oxygen exchange kinetics in proton-conducting ceramic fuel cells: Effect of electronic leakage current using symmetric cells". In: *Journal of Power Sources* 242 (Nov. 2013), pp. 784–789. DOI: 10.1016/j.jpowsour.2013.05.108.

[22] C. Hammond. *The Basics of Crystallography and Diffraction*. 3Ed. International Lunion of Crystallography Texts on Crystallography. OUP, 2009. ISBN: 978-0199546459. DOI: 10.1007/s11224-009-9480-6.

[23] F. Kröger and H. Vink. "Relations between the Concentrations of Imperfections in Crystalline Solids". In: *Solid State Physics*. Elsevier, 1956, pp. 307–435. DOI: 10.1016/s0081-1947(08)60135-6.

[24] M. Kuhn, S. Hashimoto, K. Sato, K. Yashiro, and J. Mizusaki. "Oxygen nonstoichiometry, thermo-chemical stability and lattice expansion of La0.6Sr0.4FeO3". In: *Solid State Ionics* 195.1 (July 2011), pp. 7–15. DOI: 10.1016/j.ssi.2011.05.013.

[25] J. Maier. *Physical Chemistry of Ionic Materials*. John Wiley & Sons, Ltd, Apr. 2004. DOI: 10.1002/0470020229.

[26] J. Fleig. "Microelectrodes in Solid State Ionics". In: *Advances in Electrochemical Science and Engineering, Volume 8*. Wiley-VCH Verlag GmbH & Co. KGaA, 2003, pp. 1–87. DOI: 10.1002/3527600787.ch1.

[27] A. J. Moulson and J. M. Herbert. *Electroceramics: Materials, Properties, Applications*. Wiley, 2003. ISBN: 978-0-471-49748-6. DOI: 10.1002/0470867965.

[28] R. J. D. Tilley. *Defects in Solids*. John Wiley & Sons, Inc., Sept. 2008. DOI: 10.1002/9780470380758.

[29] H.-H. Möbius. "On the history of solid electrolyte fuel cells". English. In: *Journal of Solid State Electrochemistry* 1.1 (July 1997). Cited By :76, pp. 2–16. DOI: 10.1007/s100080050018.

[30] A. J. McEvoy. "Materials for high-temperature oxygen reduction in solid oxide fuel cells". In: *Journal of Materials Science* 36.5 (2001), pp. 1087–1091. DOI: 10.1023/a:1004861221167.

[31] J. M. Ralph, C. Rossignol, and R. Kumar. "Cathode Materials for Reduced-Temperature SOFCs". English. In: *Journal of The Electrochemical Society* 150.11 (2003), A1518–A1522. DOI: 10.1149/1.1617300.

[32] C. Sun, R. Hui, and J. Roller. "Cathode materials for solid oxide fuel cells: a review". In: *Journal of Solid State Electrochemistry* 14.7 (Oct. 2009), pp. 1125–1144. DOI: 10.1007/s10008-009-0932-0.

[33] N. Minh. "Ceramic Fuel Cells". In: *Journal of the American Ceramic Society* 76.3 (1993), pp. 563–588. DOI: 10.1111/j.1151-2916.1993.tb03645.x.

[34] W. Zhu and S. Deevi. "A review on the status of anode materials for solid oxide fuel cells". In: *Materials Science and Engineering: A* 362.1-2 (Dec. 2003), pp. 228–239. DOI: 10.1016/s0921-5093(03)00620-8.

[35] M. Gerstl, A. Nenning, R. Iskandar, V. Rojek-Wöckner, M. Bram, H. Hutter, and A. Opitz. "The Sulphur Poisoning Behaviour of Gadolinia Doped Ceria Model Systems in Reducing Atmospheres". In: *Materials* 9.8 (Aug. 2016), p. 649. DOI: 10.3390/ma9080649.

[36] A. Schmid, G. M. Rupp, and J. Fleig. "Voltage and partial pressure dependent defect chemistry in (La,Sr)FeO3 thin films investigated by chemical capacitance measurements". In: *Physical Chemistry Chemical Physics* 20.17 (2018), pp. 12016–12026. DOI: 10.1039/c7cp07845e.

[37] K. Kreuer. "Proton-Conducting Oxides". In: *Annual Review of Materials Research* 33.1 (Aug. 2003), pp. 333–359. DOI: 10.1146/annurev.matsci.33.022802.091825.

[38] E. Fabbri, D. Pergolesi, and E. Traversa. "Electrode materials: a challenge for the exploitation of protonic solid oxide fuel cells". In: *Science and Technology of Advanced Materials* 11.4 (Feb. 2010), p. 044301. DOI: 10.1088/1468-6996/11/4/044301.

[39] W. Münch, G. Seifert, K. Kreuer, and J. Maier. "A quantum molecular dynamics study of proton conduction phenomena in BaCeO3". In: *Solid State Ionics* 86-88 (July 1996), pp. 647–652. DOI: 10.1016/0167-2738(96)00229-9.

[40] A. Nowick and A. Vaysleyb. "Isotope effect and proton hopping in high-temperature protonic conductors". In: *Solid State Ionics* 97.1-4 (May 1997), pp. 17–26. DOI: 10.1016/s0167-2738(97)00081-7.

[41] R. Zohourian, R. Merkle, G. Raimondi, and J. Maier. "Mixed-Conducting Perovskites as Cathode Materials for Protonic Ceramic Fuel Cells: Understanding the Trends in Proton Uptake". In: *Advanced Functional Materials* 28.35 (July 2018), p. 1801241. DOI: 10.1002/adfm.201801241.

[42] E. Fabbri, D. Pergolesi, and E. Traversa. “Materials challenges toward proton-conducting oxide fuel cells: a critical review”. In: *Chemical Society Reviews* 39.11 (2010), p. 4355. DOI: 10.1039/b902343g.

[43] E. Fabbri, L. Bi, D. Pergolesi, and E. Traversa. “High-performance composite cathodes with tailored mixed conductivity for intermediate temperature solid oxide fuel cells using proton conducting electrolytes”. In: *Energy & Environmental Science* 4.12 (2011), p. 4984. DOI: 10.1039/c1ee02361f.

[44] D. Poetzsch, R. Merkle, and J. Maier. “Proton conductivity in mixed-conducting BSFZ perovskite from thermogravimetric relaxation”. In: *Physical Chemistry Chemical Physics* 16.31 (Aug. 2014), p. 16446. DOI: 10.1039/c4cp00459k.

[45] E. Barsoukov and J. Macdonald. *Impedance Spectroscopy: Theory, Experiment, and Applications*. Wiley, 2005. ISBN: 9780471716228. DOI: 10.1002/9781119381860.ch4.

[46] J. Fleig. “The grain boundary impedance of random microstructures: numerical simulations and implications for the analysis of experimental data”. In: *Solid State Ionics* 150.1-2 (Sept. 2002), pp. 181–193. DOI: 10.1016/s0167-2738(02)00274-6.

[47] M. P. Pechini. “Method of preparing lead and alkaline earth titantes and niobates and coating method using the same to form a capacitor”. In: (1967).

[48] P. Babilo, T. Uda, and S. M. Haile. “Processing of yttrium-doped barium zirconate for high proton conductivity”. In: *Journal of Materials Research* 22.05 (May 2007), pp. 1322–1330. DOI: 10.1557/jmr.2007.0163.

[49] K. Katahira, Y. Kohchi, T. Shimura, and H. Iwahara. “Protonic conduction in Zr-substituted BaCeO3”. In: *Solid State Ionics* 138.1-2 (Dec. 2000), pp. 91–98. DOI: 10.1016/s0167-2738(00)00777-3.

[50] K. Nomura and H. Kageyama. “Transport properties of Ba(Zr0.8Y0.2)O3 perovskite”. In: *Solid State Ionics* 178.7-10 (Apr. 2007), pp. 661–665. DOI: 10.1016/j.ssi.2007.02.010.

[51] J. M. Serra and W. A. Meulenberg. “Thin-Film Proton BaZr0.85Y0.15O3Conducting Electrolytes: Toward an Intermediate-Temperature Solid Oxide Fuel Cell Alternative”. In: *Journal of the American Ceramic Society* 90.7 (July 2007), pp. 2082–2089. DOI: 10.1111/j.1551-2916.2007.01677.x.

[52] F. Baumann, J. Fleig, H. Habermaier, and J. Maier. “Impedance spectroscopic study on well-defined (La,Sr)(Co,Fe)O3 model electrodes”. In: *Solid State Ionics* 177.11-12 (Apr. 2006), pp. 1071–1081. DOI: 10.1016/j.ssi.2006.02.045.

[53] J. Jamnik. “Treatment of the Impedance of Mixed Conductors Equivalent Circuit Model and Explicit Approximate Solutions”. In: *Journal of The Electrochemical Society* 146.11 (1999), p. 4183. DOI: 10.1149/1.1392611.

[54] T. Li, M. Kim, Z. Liang, A. Asthagiri, and J. F. Weaver. “Dissociative Chemisorption and Oxidation of H2 on the Stoichiometric IrO2(110) Surface”. In: *Topics in Catalysis* 61.5-6 (Dec. 2017), pp. 397–411. DOI: 10.1007/s11244-017-0877-y.

[55] G. Vicario, G. Balducci, S. Fabris, S. de Gironcoli, and S. Baroni. “Interaction of Hydrogen with Cerium Oxide Surfaces: a Quantum Mechanical Computational Study”. In: *The Journal of Physical Chemistry B* 110.39 (Oct. 2006), pp. 19380–19385. DOI: 10.1021/jp061375v.

[56] X. Yu, X. Zhang, and S. Wang. “High coverage hydrogen adsorption on the Fe3O4(110) surface”. In: *Applied Surface Science* 353 (Oct. 2015), pp. 973–978. DOI: 10.1016/j.apsusc.2015.07.039.

[57] A. Nenning, E. Navickas, H. Hutter, and J. Fleig. “Water-Induced Decoupling of Tracer and Electrochemical Oxygen Exchange Kinetics on Mixed Conducting Electrodes”. In: *The Journal of Physical Chemistry Letters* 7.14 (July 2016), pp. 2826–2831. DOI: 10.1021/acs.jpclett.6b00778.